DESIGN AND FABRICATION OF GUIDED-MODE RESONANT TUNABLE OPTICAL FILTERS

by

MOHAMMAD JALAL UDDIN

Presented to the Faculty of the Graduate School of

The University of Texas at Arlington in Partial Fulfillment

of the Requirements

for the Degree of

DOCTOR OF PHILOSOPHY

THE UNIVERSITY OF TEXAS AT ARLINGTON

December 2013

Acknowledgements

It is my immense pleasure to acknowledge my supervising professor Dr. Robert Magnusson for giving me the opportunity to work in “Nanophotonics Device Group” that has opened the door to the exciting research area of guided-mode resonance devices. I thank you very much for your professional guidance, motivation and encouragement, advice and support, without which this work would never be possible.

I would like to thank Dr. Kambiz Alavi, Dr. Weidong Zhou, Dr. Michael Vasilyev and Dr. Samir Iqbal for their kind consent to be in my supervising committee. Thank you very much for your valuable suggestions and comments regarding this work.

I would like to thank my co-workers Dr. Jae W. Yoon, Dr. Kyu J. Lee, Tanzina Khaleque, Mohammad Shyiq Amin for their advice, suggestion through valuable discussions. I also thank Kristin P. Bergfield for her continuous help and support.

I would like to thank Dr. Jonathan Bredow, Dr. W. Alan Davis, Dr. William E. Dillon, Gail Paniuski, Ann Lewiston, Janic Moore, and Pauline Mason for different administrative help in the department.

I thank Dr. Nader Hozhabri, Thanh Bui, Dennis Bueno, and Richard K. Chambers for the training, help and support during my work in nanofab.

I would like to acknowledge the financial support by my supervisor’s funding agencies and department of electrical engineering.

Finally, I would like to thank my parents, parents-in-law, my wife Tanzina and my daughter Jinan for their support and understanding during the pursuit of this degree.

November 11, 2013

Abstract

DESIGN AND FABRICATION OF GUIDED-MODE RESONANT TUNABLE OPTICAL FILTERS

Mohammad Jalal Uddin, PhD

The University of Texas at Arlington, 2013

Supervising Professor: Robert Magnusson

Tunable optical filters have many applications in optical communication, multispectral and hyper-spectral imaging, bio-sensing, and display application. In optical communication, tunable optical filters (TOF) are used extensively in different wavelength division multiplexed (WDM) related applications. In display applications TOFs have been being used as color filters (CF) to separate primary colors from incident white light. In this study, two types of TOFs have been designed and fabricated: 1) thermo-optic tunable optical filters (TOTOF) working in optical communication bands and 2) tunable color filters (TCF) working in visible wavelength range.

TOTOFs with deep (120 nm grating depth) and shallow (20 nm grating depth) grating structures are designed and fabricated in this study. A deep TOTOF using strongly modulated gratings has been designed, which exhibits 0.07 nm bandwidth with less than 1% sideband in C band optical communication window. The existence and parametric dependence of such narrow band filter are investigated. Designed filter can be tuned 13 nm with 100℃ change in temperature.

Deep and shallow grating TOTOFs with reasonably narrow bandwidth are fabricated. Fabricated deep grating TOTOF exhibits 12 nm FWHM (theoretical FWHM = 7

nm) and a tuning range of 15 nm with tuning efficiency of 0.15 nm per degree Celsius in C communication band. Fabricated shallow grating TOTOF has a 7 nm FWHM (theoretical FWHM = 3.1 nm) and a tuning range of 12 nm with tuning efficiency of 0.12 nm per degree Celsius in L communication band.

Design and fabrication of tunable color filters (TCF) is done in the second part of this dissertation. Three types of tunable color filters: angle-tuned color filters, polarization controlled TCFs, and color filter arrays (CFA) have been investigated. The filters consist of a silicon nitride (Si_3N_4) grating along with a homogeneous Si_3N_4 layer on glass substrate.

Two types of angle-tuned filters: red and blue-shift color filters are designed and fabricated in this study. In red-shift filter, the pixel response moves from blue to red color with increasing incident angle; the pixel response moves other way in blue-shift filters. An experimental maximum efficiency of 95% is observed in the red-shift color filter whereas an experimental efficiency of 75% is reported in blue-shift color filter.

Polarization controlled tunable color filter tunes displayed color by the change of input light polarization. Red-yellow and green-blue tunable color filters have been designed and fabricated. The fabricated red-yellow filter shows red color with 99% efficiency for transverse electric (TE) polarized light and yellow color with 80% efficiency for transverse magnetic (TM) polarized light; fabricated green-blue filter exhibits green color with 90% efficiency for TE polarized light and blue color with 80 % efficiency for TM polarized light.

A color filter array (CFA) is designed and fabricated with three physical pixels spaced side by side to exhibit three primary colors. More than 90% experimental efficiency with reasonable bandwidth is achieved for three primary colors.

Table of Contents

List of Illustrations

List of Tables

Chapter 1

Introduction

1.1 Background and Progress of Guided-Mode Resonance Devices

Electromagnetic wave propagation in periodic media yields numerous effects that are both interesting and useful. Even though theoretical and experimental research into properties of periodic structures dates back more than 100 years, there is still strong interest in the subject. In particular, if the periodicity is impressed upon thin dielectric or metallic films, pronounced resonance effects are observable. These resonances are manifested as rapid variations of external electromagnetic fields outside these devices. As an early example, resonance phenomena associated with metallic diffraction gratings were observed by Wood in 1902 [1-3]; this observation is widely known as Wood's anomaly. The Wood's anomaly was theoretically analyzed by Rayleigh [4], Fano [5], and Hessel and Oliner [6]. Rayleigh suggested that the field could be expressed as a series expansion both inside the grating grooves and outside the modulated region. Fano emphasized the existence of quasi-stationary waves, which can be strongly excited on the surface of a metallic grating under critical condition depending on the profile of the grooves. Hessel and Oliner reported two types of grating anomalies: the Wood, or Rayleigh anomaly, which is due to the sharp energy exchange among the propagating orders; and a resonance type anomaly, which is due to the guided mode in the grating or at its interface. Researchers in the following years showed that such surface waves could lead to the excitation of plasmon waves [7], whose excitation is known as a surface plasmon resonance.

Much research has been done to explain the theory of dielectric diffraction gratings [8-19]. Guided-mode or leaky-mode resonances are the terms used to describe

the resonances arising on waveguide gratings as a quasi-guided waveguide mode is excited by incident light. Wang and Magnusson in [20, 21] presented an approximate theoretical analysis to locate the resonance wavelength using standard waveguide equations for weakly modulated diffraction gratings, and they demonstrated the principle of optical filtering using guided-mode resonance (GMR) devices. In the years around 1995-2001, Magnusson's group demonstrated different applications of GMR devices such as reflection and transmission filters [21-30]; laser mirrors [31], and biosensors [32]. Rosenblatt et al. in 1997 provided a simplified ray model that uses a multi-path-interference approach to derive a formula for diffraction efficiency [33]. In the past decade, different new aspects and applications of GMR devices have been demonstrated. It has been shown that a single periodic resonance layer with one-dimensional (1D) periodicity enables narrow-line bandpass and bandstop filters, polarizers, reflectors, nanoelectromechanical display pixels and polarization-independent elements [34-43]. Recently, numerous applications including Rayleigh reflector, ultrasensitive complete biosensors, absorption enhancement in solar cells have been demonstrated [44-47]. In this study, we cover the GMR tunable filters that have potential application in optical communication and display devices [48- 50].

1.2 Theory of Operation of GMR Devices

GMR structure in its elementary form has a single layer diffraction grating on a substrate. The grating structure works as a waveguide when its average refractive index is greater than that of the cover and substrate. At resonance, the diffracted waves couple in the waveguide-grating by the phase-matching condition; an efficient energy exchange between the transmitted and reflected wave takes place in a small parametric range.

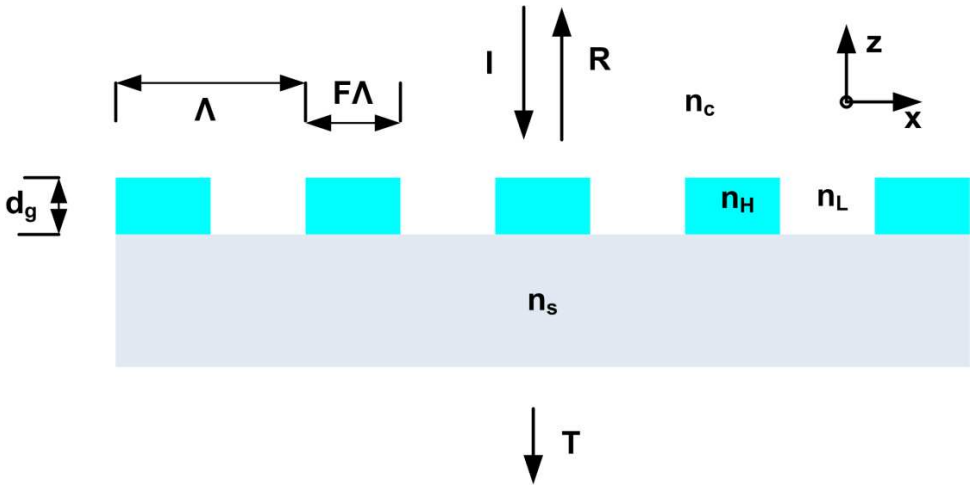

Figure 1-1 Basic structure of a single layer GMR device. d_g = grating depth, F = fill factor, Λ = period, I = incident light wave, T = transmittance, R = reflectance.

The device layers and parameters are shown in Figure 1-1, where d_g denotes grating depth, F fill factor, Λ period, I incident light wave, T transmittance, and R reflectance. The grating layer consists of a high-index material n_H and a low-index material n_L; n_s and n_c are the refractive index of substrate and cover respectively. Considering the GMR structure in Figure 1-1, when a plane wave is incident on the grating layer, it is diffracted into multiple orders. The diffracted waves couple to the waveguide-grating layer satisfying a phase-matching condition. The electric field distribution inside the grating region can be expressed as [20, 21]

$$\frac{dE_i^2(z)}{dz^2} + \left[k_0^2 n_{eff}^2 - k_0^2\left(n_c \sin\theta - i\,{}^{\lambda}/_{\Lambda}\right)^2\right] E_i(z) + k_0^2 \Delta\varepsilon \sum_{h=1}^{\infty} \frac{\sin(h\pi f)}{h\pi}\left[E_{i-h}(z) + E_{i+h}(z)\right] = 0 \quad (1.1)$$

where $E_i(z)$ is the y-component of the electric field amplitude of the i-th order diffracted wave, λ is the wavelength, $k_0 = {}^{2\pi}/_{\lambda}$, θ is the incident angle, $k_0\left(n_c \sin\theta - i\,{}^{\lambda}/_{\Lambda}\right)$ is the x component of wave propagation constant in the grating region, $\Delta\varepsilon = n_H^2 - n_L^2$ is the index

modulation, h is the integer Fourier harmonic index, and n_{eff} is the effective refractive index of the grating layer using zero-order effective medium theory. For TE polarized light,

$$n_{eff} = [f n_H^2 + (1-f) n_L^2]^{1/2}. \tag{1.2}$$

For TM polarized light,

$$n_{eff} = \left[{f}/{n_H^2} + {(1-f)}/{n_L^2} \right]^{-1/2}. \tag{1.3}$$

To simplify the equation, the coupling term is ignored for weakly modulated grating, where $\Delta\varepsilon \approx 0$ and the coupled wave equation can be reduced to

$$\frac{dE_i^2(z)}{dz^2} + \left[k_0^2 n_{eff}^2 - k_0^2 \left(n_c \sin\theta - i\,{\lambda}/{\Lambda} \right)^2 \right] E_i(z) = 0. \tag{1.4}$$

Considering the waveguide-grating layer of the GMR structure, the electric field distribution of the wave propagating in the waveguide can be expressed [20, 21] as

$$\frac{dE^2(z)}{dz^2} + \left[k_0^2 n_{eff}^2 - \beta^2 \right] = 0. \tag{1.5}$$

where β is the propagation constant of the mode supported by the waveguide-grating structure. A GMR takes place only when a diffracted wave is phase matched to a wave mode which is supported by the waveguide layer. From equation (1.4) and (1.5) the condition for phase matching is

$$\beta = k_0 \left(n_c \sin\theta - i\,{\lambda}/{\Lambda} \right). \tag{1.6}$$

At phase matching condition, the ith wave diffracted by the grating evanescently propagates in the waveguide-grating. If $i = 1$ or $i = -1$, the evanescent wave strongly couples to the zero-order wave and a complete energy exchange takes place between the forward and backward waves. If there is a constructive interference at the input side

and consequent destructive interference at the output side, the device works as a reflection filter and 100% reflection occurs at the resonance wavelength.

1.3 Two Layer GMR Structure

GMR devices, in this study, consist of a diffractive element and a homogeneous waveguide layer as shown in Figure 1-2. The homogeneous layer and the gratings are the same material making the device a single-material structure [51].

The device layers and parameters are shown in Figure 1-2, where d_g denotes grating depth, d_h homogeneous waveguide thickness, F fill factor, Λ period, I incident light wave, T transmittance, R reflectance. The grating layer consists of a high index material n_H and a low index material n_L; n_s, n_c and n are refractive index of substrate, cover and homogeneous layer.

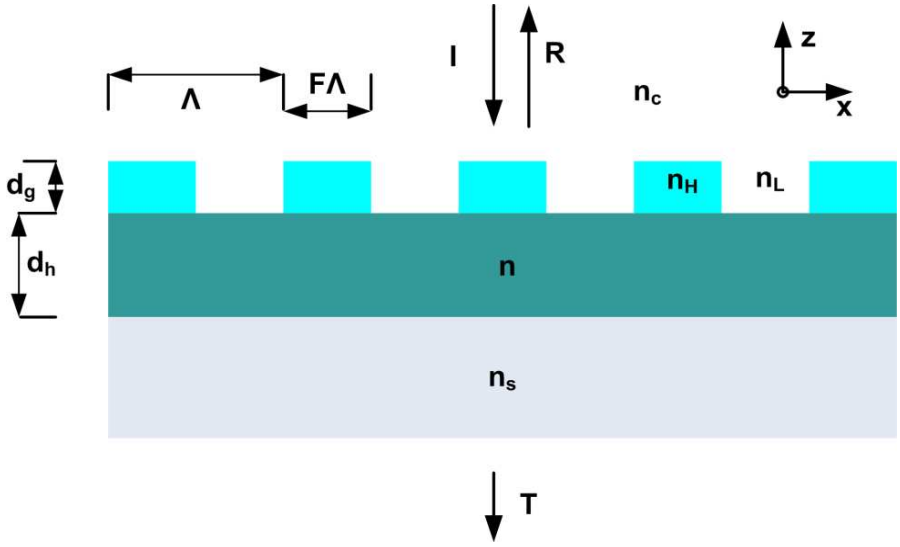

Figure 1-2 Basic structure of a two layer single-material GMR device having a diffraction grating and a homogeneous waveguide layer. d_g = grating depth, d_h = waveguide thickness, F = fill factor, Λ = period, I = incident light wave, T = transmittance, R = reflectance.

For the device in Figure 1-1, let us choose the material as Si_3N_4 with device parameters n = 2.02, F = 0.5, d_g = 55 nm, d_h = 110 nm and □ = 320 nm; and with the input being normally incident TE-polarized light. The calculated resonant spectral response of the device is shown in Figure 1-3. The calculation is performed based on a numerical method using rigorous coupled-wave analysis (RCWA) [13,15] of equation (1.1). If the diffraction grating is represented by an equivalent homogeneous layer with effective index calculated by the zero-order effective medium theory, no resonance occurs as shown in Figure 1-2. This explains the grating effect that creates sharp resonance phenomenon in GMR devices.

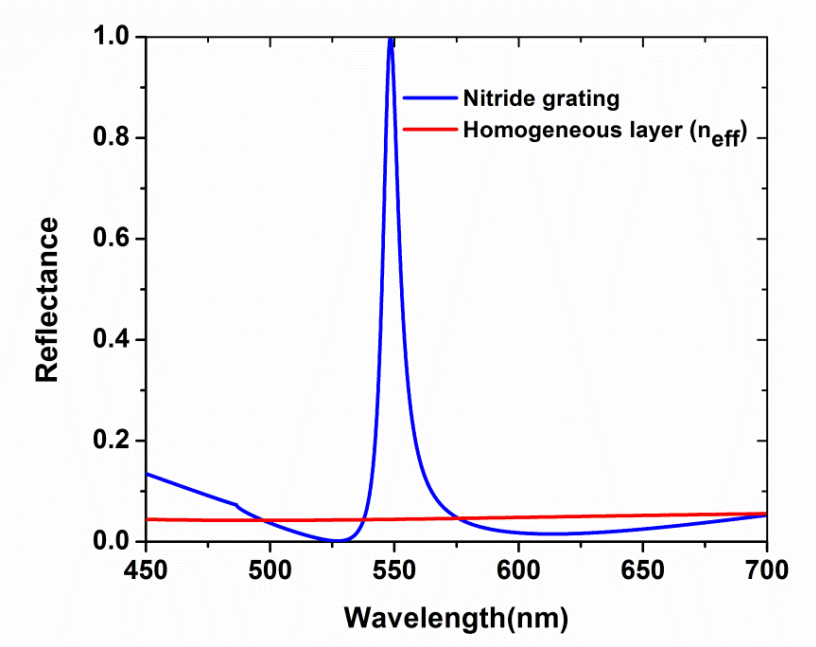

Figure 1-3 Guided-mode resonance behavior of the device shown in Figure 1.2 for normally incident TE polarized light. The device parameters are: n = 2.02, F = 0.5, d_g = 55 nm, d_h = 110 nm and □ = 320 nm. No resonance behavior is observed if the grating layer is replaced by a homogeneous layer with its effective refractive index. The effective refractive index n_{eff} = 1.594 for this structure.

1.4 Organization of the Dissertation

This study includes the design and fabrication of guided-mode resonant tunable optical filters. Two main types of tunable optical filters are investigated. One filter works in the optical communication wavelength range, and the other filter works in the visible wavelength range. This dissertation includes five chapters that detail different sub-projects of this work.

Chapter 2 investigates the design of an ultra-narrow-band GMR filter using a Si grating on a glass substrate with 0.07 nm bandwidth and less than 1% side-band in the C-band communication window. The origin and parametric dependence of the spectral position and bandwidth of the filter are investigated. The designed filter is thermo-optically tunable and can be tuned up to 12 nm with a temperature increase of 100℃.

Chapter 3 demonstrates the design and fabrication of thermo-optic tunable filters using Si gratings on glass substrates. Two types of filters are fabricated, including deep (grating depth 120 nm) and shallow (grating depth 20 nm) gratings. The filters operate in the C- and L-band optical communication bands. Approximately 15-nm wavelength shift is experimentally observed with 100℃ increase in t emperature.

Chapter 4 presents angle-tuned resonant color filters for projection display applications. Two types of tunable filters, red- and blue-shift color filters, are designed and fabricated. In this study, one physical pixel separates three primary colors from the incident white light.

Chapter 5 provides the design and fabrication of polarization-controlled tunable color filters. We observe color tuning by changing the polarization state of the input light. Two types of color filters, red-yellow and green-blue tunable color filters, are designed and fabricated. The red-yellow filter switches color from red to yellow, and the green-blue

filter switches color from green to blue when the input light polarization state changes from TE to TM.

Chapter 6 presents the design and fabrication of a tunable color filter array that has the potential for LCD display applications. Three physical pixels are fabricated using a single fabrication step, and they separate three primary colors upon incident white light. Very high experimental efficiency is observed with a reasonably narrow bandwidth for the GMR filters.

Chapter 7 discusses the future research directions based on the platform developed in this work.

Chapter 2

Design of Narrow-Band Thermo-Optic Tunable Resonant Filters

Narrowband guided-mode resonant devices can be realized with silicon gratings in spite of the strong index modulation between silicon and air. We investigate the origin of a silicon-based narrow-band filter and its parametric dependence on the device parameters. We design a thermo-optic tunable narrow-band filter using silicon gratings on glass substrates. We report as low as 0.07 nm bandwidth with less than 1% sidebands of the designed filter. The designed filter has a tuning range of 13 nm with a temperature change of 100℃.

2.1 Introduction

Wavelength division multiplexed (WDM) optical communication systems are in practical use to meet high data demands. Tunable optical filters (TOFs) have numerous applications in WDM communications. They have applications in add-drop multiplexing, channel performance monitoring, channel reconfiguration, noise suppression, and pulse shaping. In those applications, TOFs help to dynamically select a particular wavelength channel. In tunable lasers, TOFs are used to select a particular laser mode. They also find use in optical sensing, imaging spectroscopy etc.

There is increasing worldwide interest in GMR effects that originate in quasi-guided, or leaky, waveguide modes induced on patterned films with subwavelength periods. Whereas these effects have been known for a long time [9-21], new aspects and applications continue to appear.

In this study, we design a narrow-band thermo-optic TOF using a Si grating with bandwidth near 0.07 nm and sidebands less than 1% . We investigate the origin of this

narrow band resonance. We also investigate the dependence of the resonance wavelength and bandwidth on different structural parameters such as grating thickness, homogeneous layer thickness, and fill factor of the device. Designed narrowband filters can be tuned 13 nm with 100℃ change in temperature. With this tuning capability, the filter can cover more than 40 WDM channels with 0.2 nm (25 GHz) channel spacing.

2.2 Device Structure and Parameters

The designed narrow-band tunable optical filter consists of a subwavelength amorphous silicon (a-Si) grating along with an a-Si homogeneous layer on a glass substrate. The combined periodic and homogeneous layers constitute a waveguide grating. The device layers and parameters are shown in Figure 2-1, where d_g denotes grating depth, d_h homogeneous waveguide thickness, F fill factor, Λ period, I incident light wave, T_0 zero-order transmittance, and R_0 zero-order reflectance. The refractive index of Si_3N_4, substrate and cover are n, n_s and n_c respectively. As the period of the grating is chosen to be significantly smaller than the operating wavelengths, the device works in the zero-order diffraction regime. A GMR takes place when diffracted light from the grating structure is coupled with a leaky waveguide mode satisfying the phase-matching condition; as a result, a sharp resonance peak is observed at a particular wavelength. The details of GMR filter operation are explained in [20, 21]. The position of the resonance wavelength can be tuned by changing the refractive index, period, thickness, and incident angle as discussed in [21,37].

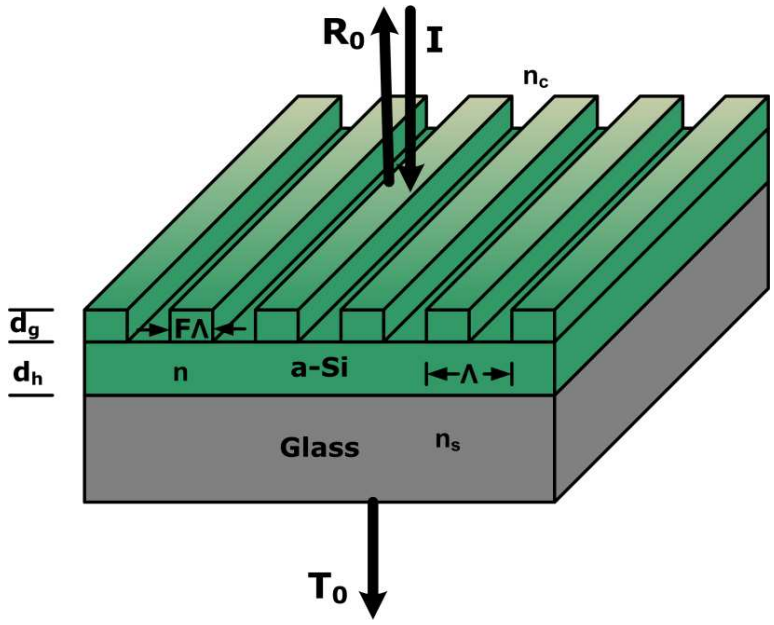

Figure 2-1 Basic GMR structure with Si/air diffraction grating. d_g = grating depth, d_h = waveguide thickness, Λ = period, F Λ = width of the high index region, F = fill factor, I = incident light wave, T_0 = zero-order transmittance, and R_0 = zero-order reflectance. n, n_s and n_c are the refractive index of the Si_3N_4, substrate and cover respectively.

2.3 Design and Analysis

We design the device using rigorous coupled-wave analysis (RCWA) based MATLAB codes and commercial RSoft software. We use the Rsoft software to do the forward calculations to get the best design regarding the resonance wavelength, FWHM, and side-band levels. The "most" option of Rsoft is able to run hundreds of forward simulations for different parametric variations. A GMR based narrowband filter with a bandwidth of 0.07 nm and less than 1% sidebands is designed and analyzed in this study. Figure 2-2 shows the static response of the designed filter. The parameters used for the design are given in figure caption. Normally incident TE polarized light is used for

the simulation. The spectral response of the same filter in logarithmic (dB) scale are shown in Figure 2-3 that shows an approximately -20 dB insertion loss at the sidebands.

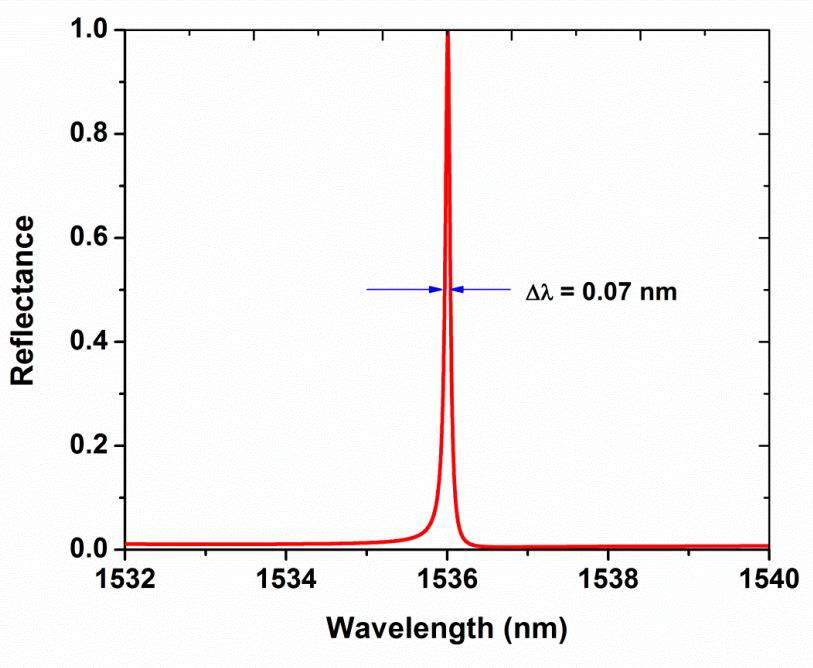

Figure 2-2 Ultra-narrow band guided-mode resonance filter using strongly modulated Si/Air grating structure. Resonance wavelength = 1536.01 nm, FWHM = 0.07nm. The device parameters are: Λ = 900 nm, d_h = 335 nm, d_g = 110 nm, n = 3.73, n_c =1.0,n_s = 1.5, polarization = TE and normally incident light.

Figure 2-4 shows different GMRs that takes place in the sub-wavelength region of this structure under study. GMR#1 arises in the deep subwavelength region; GMR 2, 3 and 4 exist in the near subwavelength region. From the one dimensional filed plot along the device dimension as shown in Figure 2-5, we can confirm different modes associated with the resonances. GMR #1 is a $TE_{1,0}$ mode, GMR #2 is a $TE_{1,1}$ mode, GMR #3 is $TE_{2,0}$ mode and GMR #4 is the mixture of modes $TE_{1,2}$,and $TE_{2,1}$. In the expression $TE_{m,n}$ m is the m^{th} diffracted order and n is n^{th} mode of the waveguide.

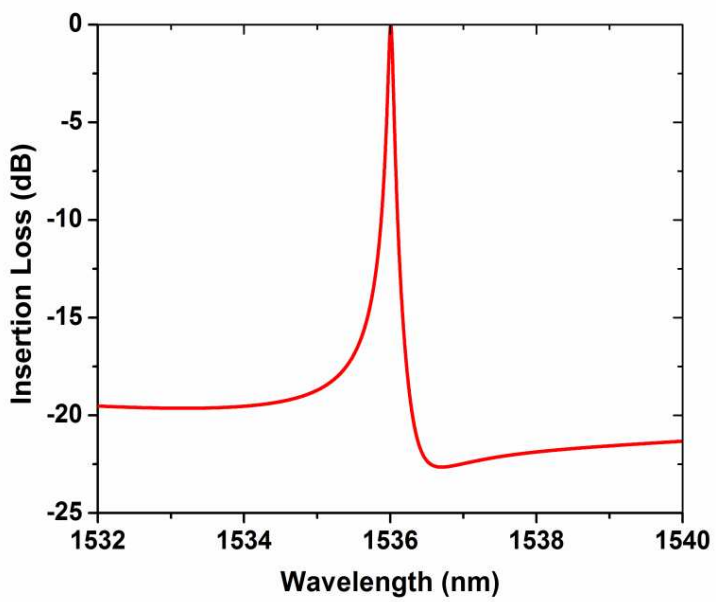

Figure 2-3 Static filter response in log-scale (dB). Device parameters are same as in the caption of Figure 2-2.

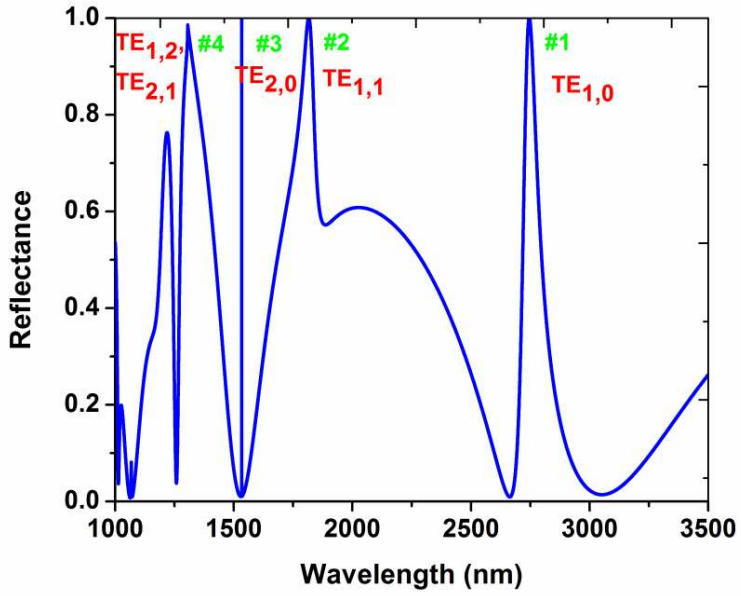

Figure 2-4 Zero order reflectance spectra of the designed filter. Device parameters for this plot are: Λ = 900 nm, d_h = 335 nm, d_g = 110 nm, n = 3.73, and F = 0.47.

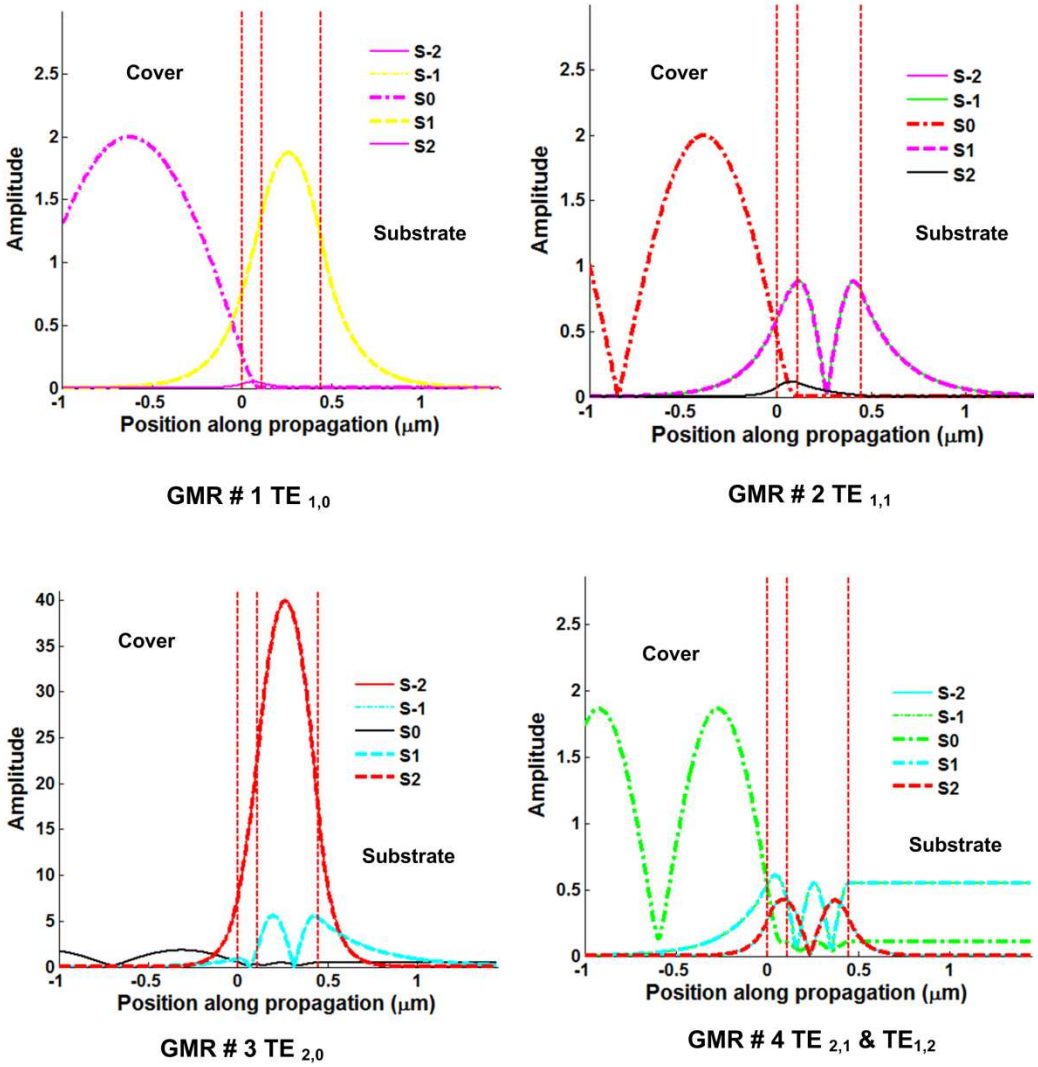

Figure 2-5 One dimensional field plot showing coupling of different diffraction orders into waveguide modes.

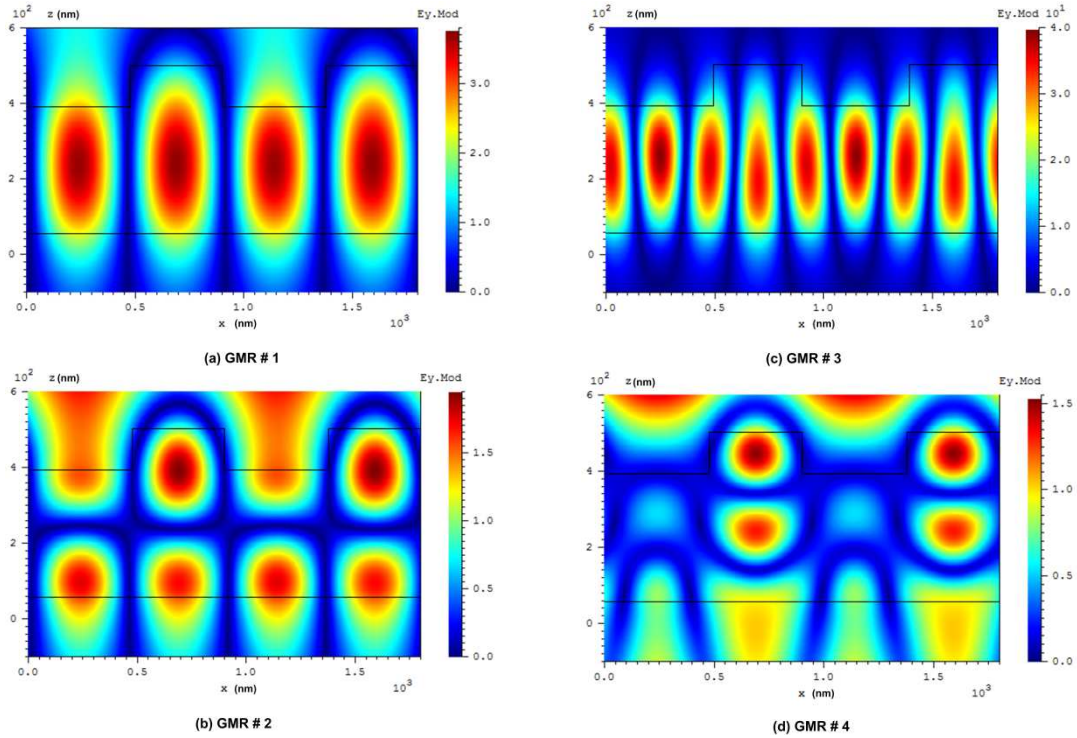

Figure 2-6 Field plot corresponding to different resonances shown in Figure 2-4. (a) GMR #1 is a $TE_{1,0}$ mode, (b) GMR#2 shows a $TE_{1,1}$ mode, (c) GMR #3 is a $TE_{2,0}$ mode, and (d) GMR #4 is a mixture of $TE_{2,1}$, and $TE_{1,2}$. The same device parameters from Figure 2-4 are used for this calculation.

Figure 2-6 provides the field plots associated with different resonances. The different modes associated with field plots are given in the Figure caption. We see that the field strength for the narrow-band GMR #3 is approximately 10 times higher than the others.

2.3.1 Variation of Grating Depth

In GMR device design, each parameter of the structure determines its spectral behavior. Figure 2-7 shows the effect of grating depth on FWHM using the reflectance contour map. We see that with the increase of grating depth beyond 100 nm, we get decrease of FWHM accompanied by increased sidebands. We need to select an optimum grating depth to get the minimum FWHM and acceptable sideband levels. For the current design we select grating depth of 110 nm, which gives 0.07 nm FWHM and less than 1% sideband levels. Figure 2-8 presents the spectral response of the filter associated with GMR #3 against grating depths. At higher grating depth, more radiated light couples back to the waveguide mode that increases the photon life time, increases the Q of the filter and reduces its bandwidth.

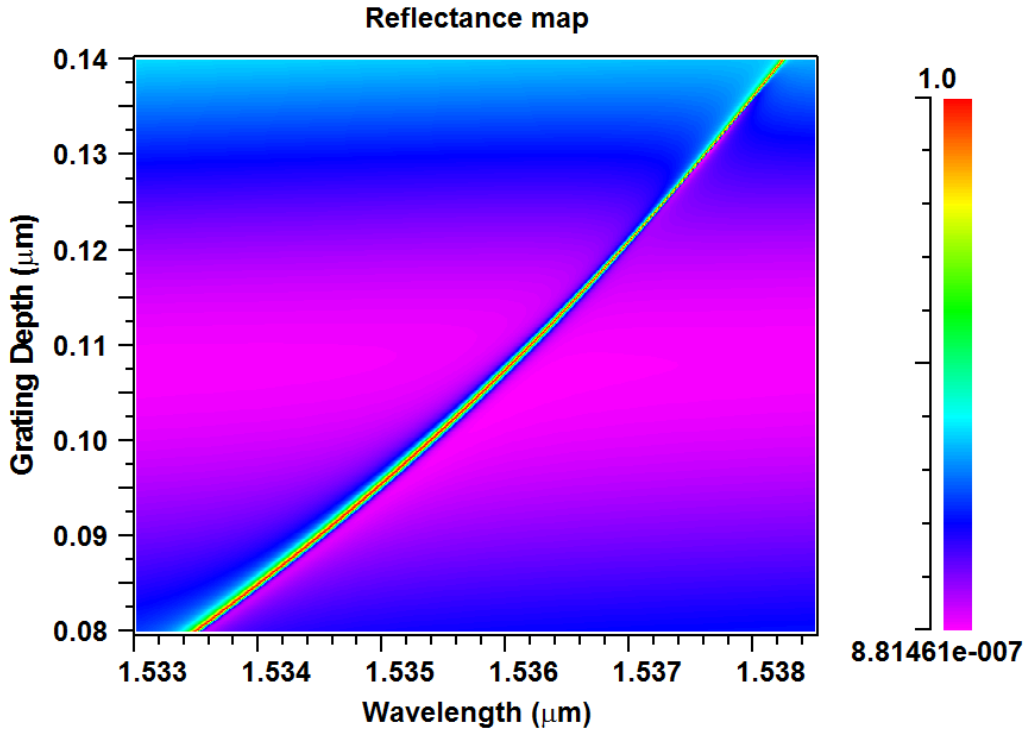

Figure 2-7 Reflectance contour map showing the effect of grating thickness in resonance spectra. Device parameters are: Λ = 900 nm, d_h = 335 nm, n = 3.73, F = 0.5.

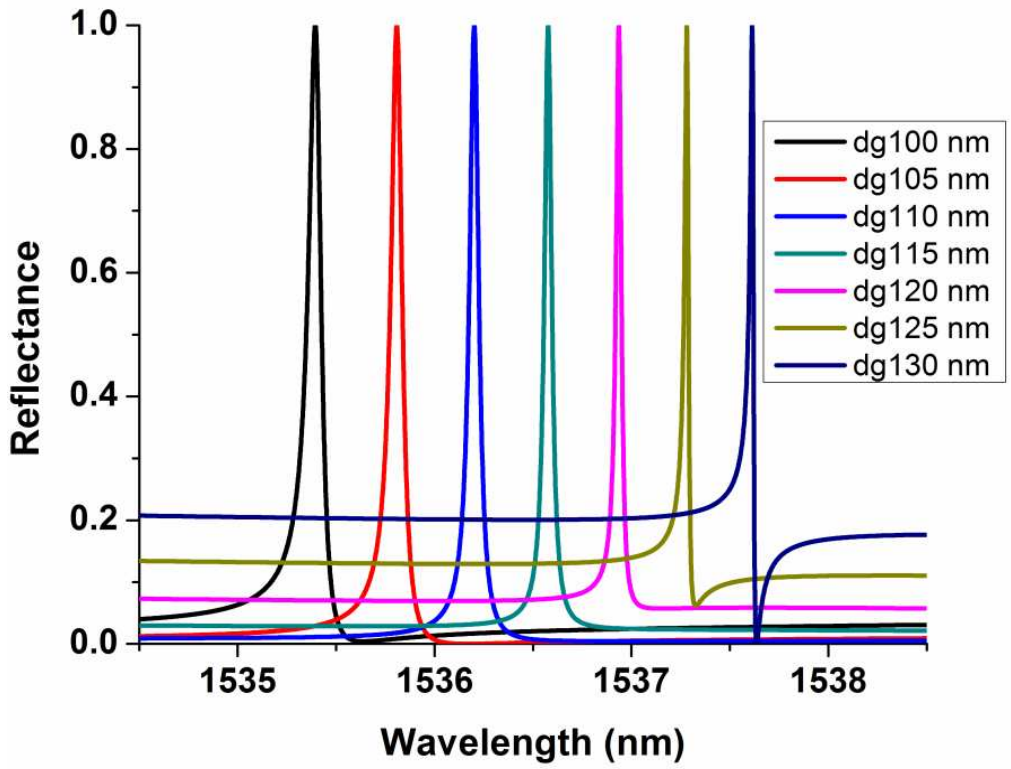

Figure 2-8 Effect of grating thickness in resonance spectra. Device parameters are: Λ = 900 nm, d_h = 335 nm, n = 3.73, and F = 0.5.

2.3.2 Variation of Fill Factor

The bandwidth of the filter can be controlled by changing the fill factor. Figure 2-9 depicts the reflectance map with fill factor and wavelength as varying parameters. We see that FWHM is minimum at F = 0.5; and a significant amount of tuning of the resonance wavelength takes place due to the variation of fill factor. Vanishing width at F = 0.5 means very narrow bandwidth of the filter that we cannot see without magnification.

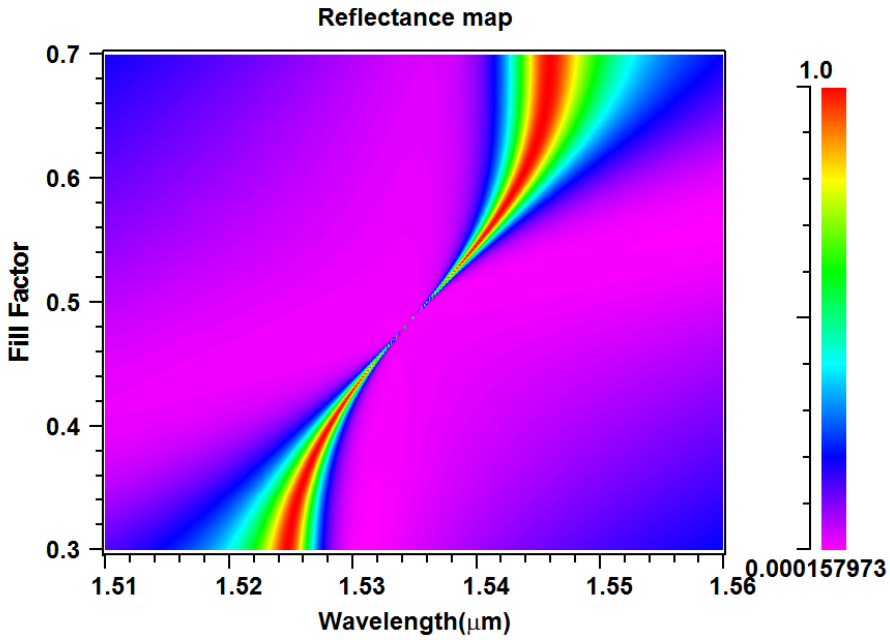

Figure 2-9 Reflectance map showing the effect of fill factor on resonance wavelength and FWHM. Device parameters are: Λ = 900 nm, d_g = 110 nm, d_h = 335 nm, and n = 3.73.

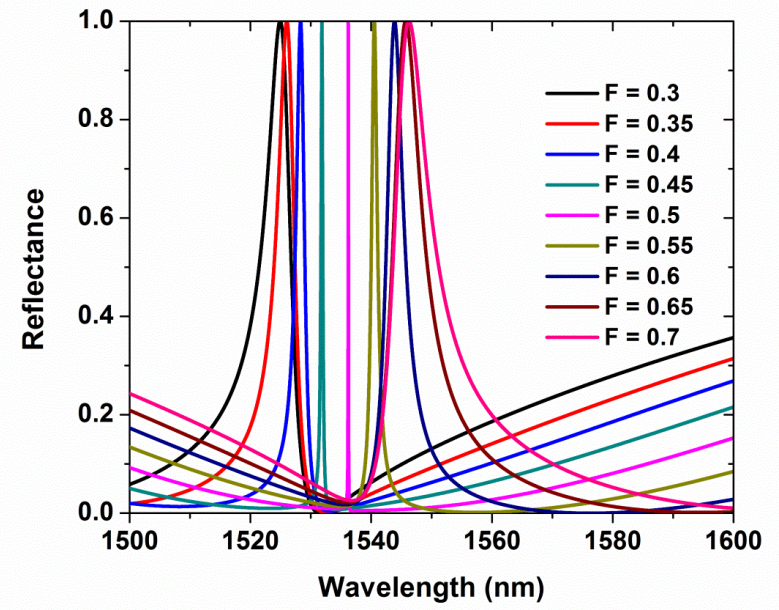

Figure 2-10 Effect of fill factor on resonance wavelength and FWHM. Device parameters are: Λ = 900 nm, d_g = 110 nm, d_h = 335 nm, and n = 3.73.

The spectral response in Figure 2-10 shows how the FWHM and the resonance wavelength of the filter depend on the fill factor. We see an increase in FWHM when the fill factor is away from the value of 0.5 and there is a 22 nm resonance shift due to the change of fill factor from 0.3 to 0.7. Figure 2-11 gives the quantitative computed value of FWHM against the fill factor. We get the minimum FWHM at F = 0.5, which is 0.07 nm for the current design.

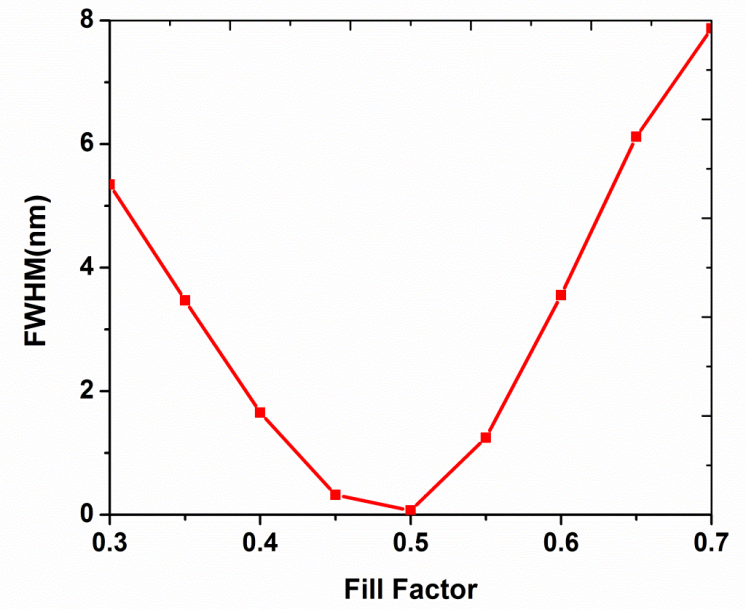

Figure 2-11 Variation of FWHM as a function of fill factor. Device parameters are: Λ = 900 nm, d_g = 110 nm, d_h = 335 nm, and n = 3.73.

2.3.3 Variation of Homogeneous Layer Thickness

Figure 2-12 illustrates the resonance behavior as a function of homogeneous layer thickness using the reflectance map. We see that homogeneous layer plays a very important role for making such a narrow-band GMR filter using strongly modulated gratings. The narrow-band resonance occurs at d_h = 335 nm. At this optimum homogeneous layer thickness, the nearby two resonances are strong and symmetric to

the spectral position of the desired narrowband filter. The strength and symmetry of GMR # 2 and GMR #4 determine the behavior of GMR #3, which is explained in Figure 2-13.

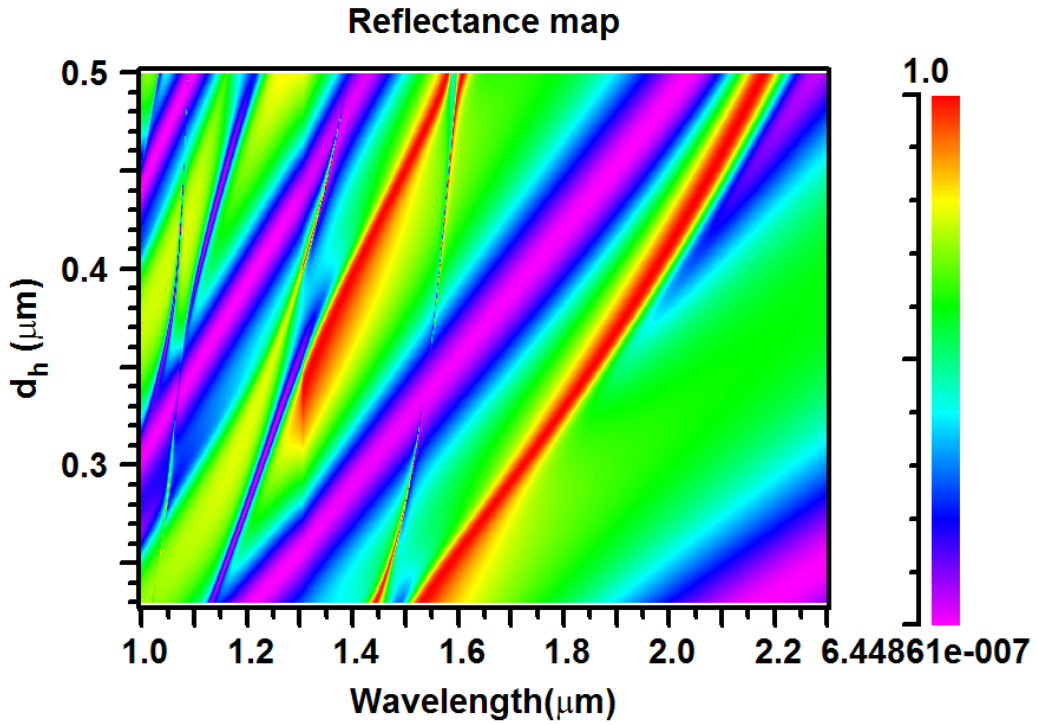

Figure 2-12 Reflectance map showing the effect of homogeneous layer thickness in resonance spectra. Device parameters are: Λ = 900 nm, d_g = 110 nm, n = 3.73, F = 0.5.

Figure 2-13 shows the spectral response of the filter for different homogeneous layer thickness. Figures 2-13(a) to (f) depict the interacting resonances, their strength and their spectral position relative to that of the desired narrow band filter. Figures 2-13 (a) to (d) show how the interacting left (GMR #4) resonance gets stronger and comes closer to the right (GMR #2) resonance. When their spectral positions are symmetric and strong, we get the desired narrowband filter (GMR #3) in the middle of these two resonances. Figure 2-12 (e) and (f) show that when the right resonance moves away, the symmetry collapses and the narrow-band response with lower side bands vanishes.

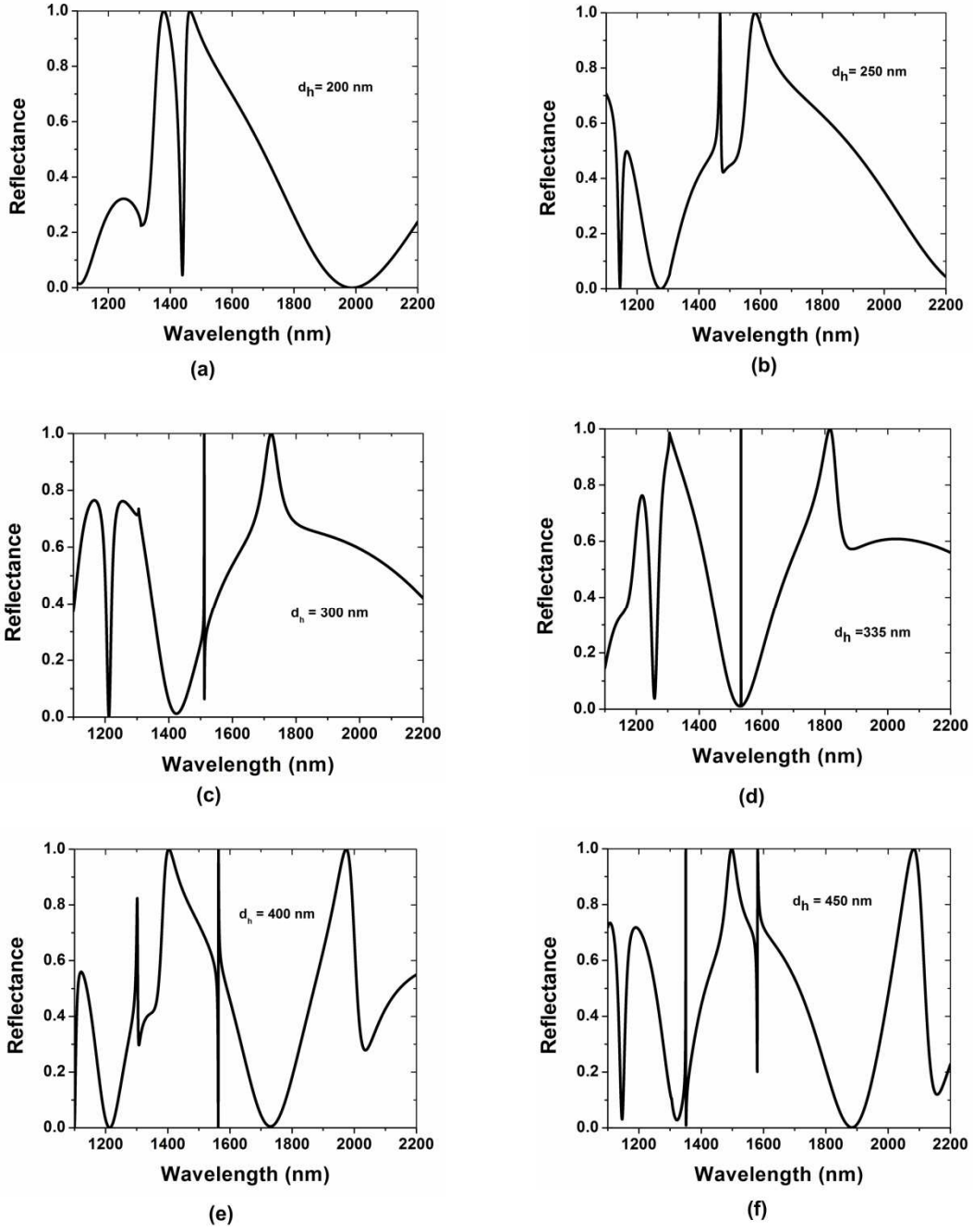

Figure 2-13 Resonance behavior of the device for varying homogeneous layer thickness.

Device parameters are: Λ = 900 nm, d_g = 110 nm, n = 3.73, F = 0.47.

2.3.4 Effect of Material Loss

Material loss strongly affects the narrow-band resonance discussed in this study. Figure 2-14 demonstrates the reflectance for different extinction coefficients. The device parameters used for simulation are: Λ = 900 nm, d_h = 335 nm, d_g = 110 nm, n = 3.73, F = 0.5. We see that the extinction coefficient should be less than 10^{-5} to sustain such narrow band filter response.

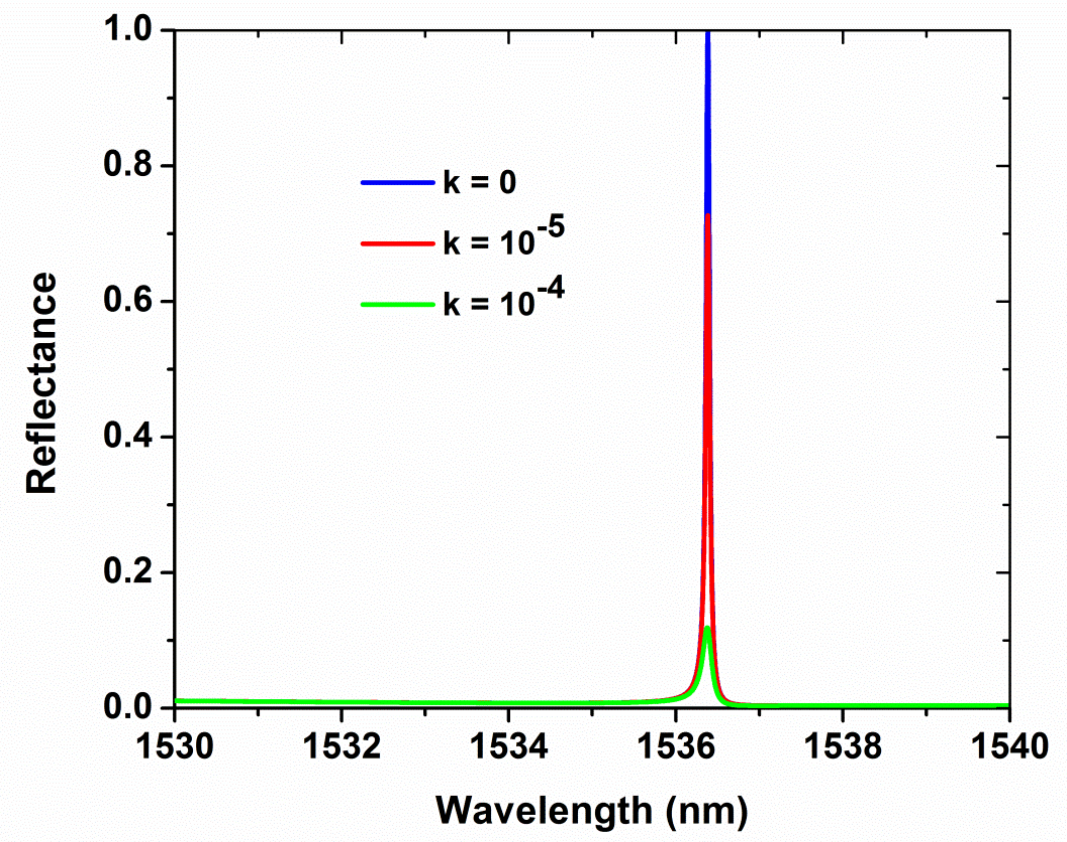

Figure 2-14 Effect of extinction co-efficient on narrowband GMR filter response.

2.5 Thermo-Optic Tunability

The narrow-band filter designed in this study is thermo-optically tunable because Si has a high thermo-optic coefficient. The refractive index of Si is modulated due to the temperature variation and this modulation gives the resonance shift resulting in a tunable optical filter. The dependence of refractive index on temperature is given as follows:

$$n = n(T_0) + \alpha(T - T_0) \tag{2.1}$$

$\alpha = dn/dT$ = thermo-optic coefficient of the material.

T_0 = Room temperature

T = Temperature

For a-Si, the thermo-optic coefficient used in this calculation is 3.25 ×10^{-4}.

The value of n influences N, the effective index of the waveguide gratings; thus affecting the resonance wavelength.

Figure 2-15 shows the thermo-optic tuning of the designed optical filter. There is a 13.3 nm resonance shift with 100℃ rise in temper ature which gives tuning sensitivity of 0.133 nm per degree Celsius. With this temperature variation, the designed filter can cover more than 40 WDM channels with 0.2 nm (25 GHz) channel spacing. Therefore, the designed filter has good potential of finding application in WDM communication systems.

Figure 2-16 shows the shift of resonance wavelength with temperature change. We see that there is a linear relationship between the resonance shift and temperature.

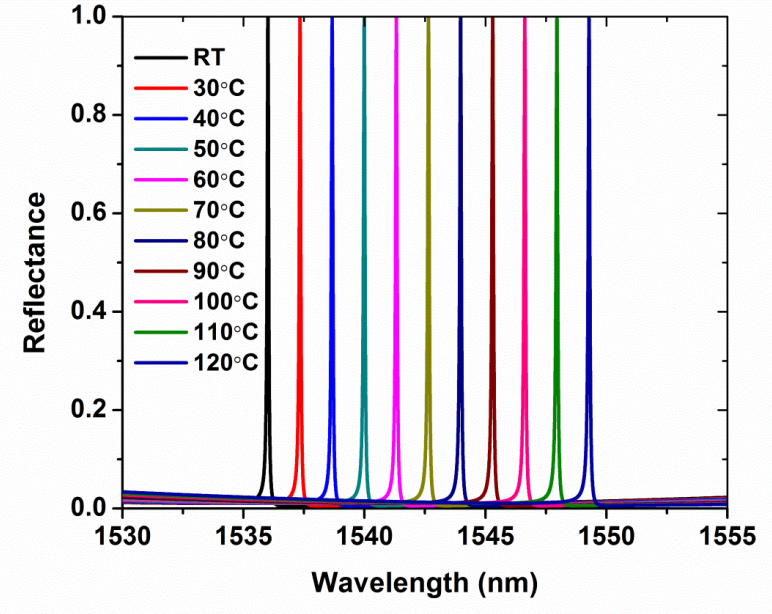

Figure 2-15 Design of thermo-optic TOF using ultra-narrow band filter. Device parameters are: Λ = 900 nm, d_h = 335 nm, d_g = 110 nm, n = 3.73, F = 0.5, and α = 3.25 $\times 10^{-4}$. The calculated tuning range is 13.3 nm for a temperature change of 100℃.

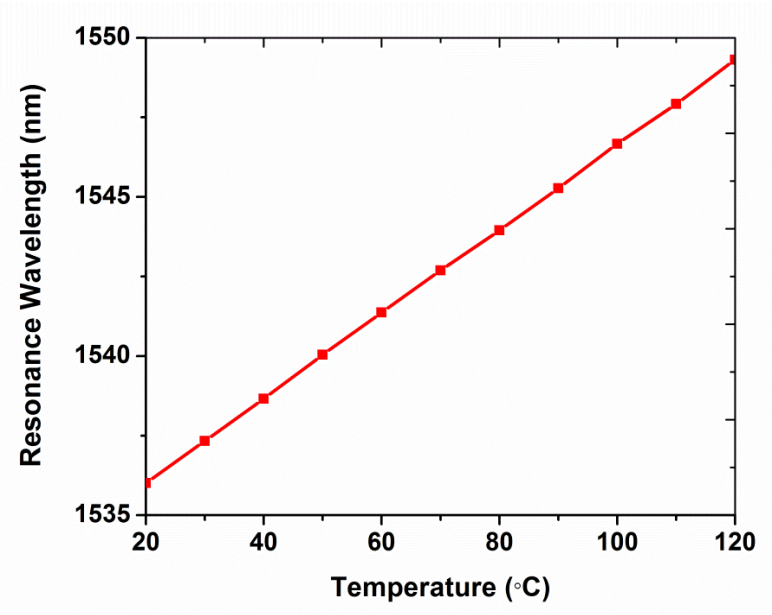

Figure 2-16 Resonance shift as a function of temperature.

Chapter 3

Fabrication and Characterization of Guided-Mode Resonant Thermo-Optic Tunable Filters

We experimentally demonstrate electrically controlled guided-mode resonant thermo-optic tunable optical filters. We design the devices using numerical methods based on rigorous coupled-wave analysis (RCWA) and pattern the structure with a UV laser interferometric lithography system. The fabricated devices consist of subwavelength amorphous silicon (a-Si) gratings along with homogeneous a-Si waveguides on glass substrates. We fabricate deep (~120 nm) and shallow (~20 nm) grating filters that work in the C and L optical communication bands. We thermo-optically change the refractive index of a-Si using electrical Joule heating to spectrally tune the filters. We achieve 15 nm and 12 nm spectral tuning for these deep and shallow grating devices, respectively, with a temperature increase of 100℃.

3.1 Introduction

Tunable optical filters (TOF) find applications in displays [48,49], optical communications [52], multispectral and hyper-spectral imaging [53], and optical sensing [54]. In optical communications, TOFs are used extensively for wavelength division multiplexing (WDM) functions such as add-drop multiplexing, channel performance monitoring, channel reconfiguration, noise suppression and pulse shaping. In WDM, the capability to dynamically select a particular wavelength channel is particularly useful. TOFs are used in tunable lasers and in imaging and display applications to select a particular band that renders a needed wavelength or color.

Much research has been devoted to finding a TOF with optimum size, cost, sensitivity, resolution, tuning range, response time, compactness and economic fabrication. A TOF with all these desired features remains a challenge. There are many approaches to achieve spectral tuning. The tuning principle can be acousto-optic [55], electro-optic [56], piezo-electric [57, 58], MEMS [59, 60] or thermo-optic [61–66]. The filter structures can have Mach-Zehnder (MZ) [61], Fabry-Perot (FP) [62–64], Bragg grating (BG) [65] or ring resonator (RR) [66] architecture.

The objective of the work reported presently is to investigate a new concept that is potentially useful in the arsenal of tunable filters. Hence, we fabricate guided-mode resonance (GMR) type thermo-optic tunable optical filters (TOTOF). Thermo-optic tuning is effective due to attendant static environment, precise tuning, and freedom from vibrations, high sensitivity, reasonable response time, electrical control and availability of narrow bandwidth devices. Low-loss materials with comparatively high thermo-optic coefficient are available to cover the telecom wavelength band. In these filters, the refractive index is changed by variation of temperature and this consequently changes the center wavelength of the filter. Examples of TOTOFs reported include FP, BG, MZ and RR structures as briefed above. For our GMR-TOTOF, we use a subwavelength a-Si grating along with a homogeneous a-Si waveguide on a glass substrate. In this letter, we describe an electrically controlled thermo-optic tunable resonant filter structure that works in the C and L optical communication bands. We demonstrate fabricated devices along with experimentally measured tunable spectral responses. We achieve reasonable agreement between theoretical and experimental results. A GMR-based TOTOF has not been reported previously to our knowledge.

3.2 Filter Structure and Operation

Our GMR-based TOTOFs consist of a subwavelength a-Si/air diffraction grating with a homogeneous a-Si waveguide layer on a glass substrate. The schematic cross section of the basic GMR structure is given in Figure 3-1 (a); it has lateral dimensions of 5 mm × 5 mm. A GMR occurs when diffracted light from the grating couples with a leaky waveguide mode satisfying the phase-matching condition; as a result, a sharp resonance peak is observed at a particular wavelength. The details of GMR filter operation are explained in [20, 21]. The position of the resonance wavelength can be tuned by changing the refractive index, period, thickness, incident angle and polarization of light as discussed in detail in [20, 21].

In this study, we use the thermo-optic tuning of the refractive index to tune the spectral response of the filter. The refractive index of a material (n) has a linear relationship ($n = n_0 + \alpha\Delta T$) with the temperature deviation (ΔT) limited by the thermo-optic coefficient of the material $\alpha = dn/dT$. The thermo-optic coefficient of a-Si is $3.25 \times 10^{-4}/℃$ [63]. In GMR structures, the resonance wavelength has a linear relationship with the refractive index of the associated materials across small ranges. Therefore, with increase of temperature we observe a red shift of the resonance wavelength. The top view of the TOTOF is given in Figure 3-1 (b). Heating is accomplished by supplying an electric current through a 100 nm thick and 3 mm wide square aluminum (Al) metallic electrode, which is fabricated around the device. Due to Joule heating caused by the sheet resistance of the Al, we raise the temperature thus changing the refractive index. Copper tape is used as contact to make the electrical connection to the power supply.

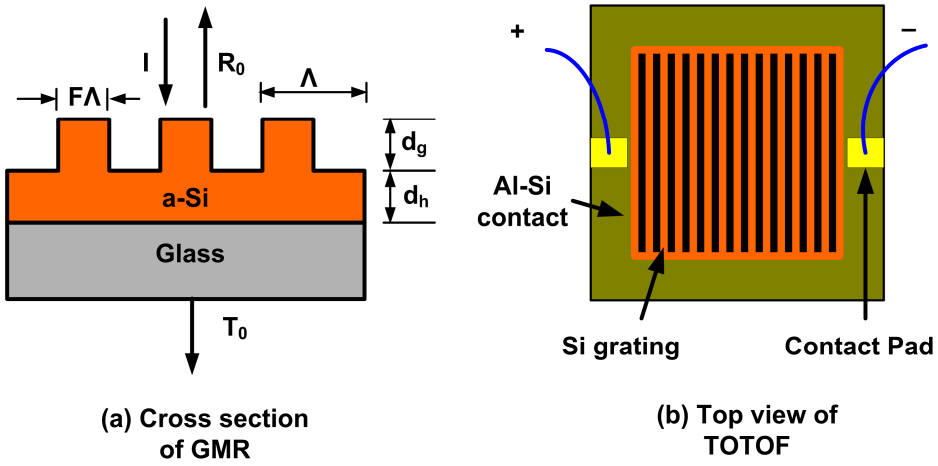

Figure 3-1 (a) Cross section of grating structure. The device parameters are d_g = grating depth, d_h = homogeneous waveguide thickness, F = fill factor, Λ = period, I = incident light wave, T_0 = zero-order transmittance and R_0 = zero-order reflectance. (b) Top view of TOTOF showing Joule heating arrangement.

3.3 Design and Analysis

In this study, we design and fabricate two thermo-optic tunable filters. One filter consists of a deep (120 nm grating depth) and the other filter consists of a shallow (20 nm grating depth) gratings. There is a homogeneous Si layer beneath the grating on a glass substrate for both structures.

3.3.1 Deep Grating Thermo-Optic Tunable GMR Filter

The spectral dependence on structural parameters of a deep grating filter is investigated in detail in Chapter 2 and is not repeated here. We design a deep grating filter with bandwidth exceeding a nanometer. We design the devices using RCWA running under MATLAB as well as with RSoft software. Figure 3-2 shows the spectral

response of a deep grating thermo-optic tunable filter with FWHM of 1.45 nm. The tuning range is 13 nm with a temperature rise of 100℃.

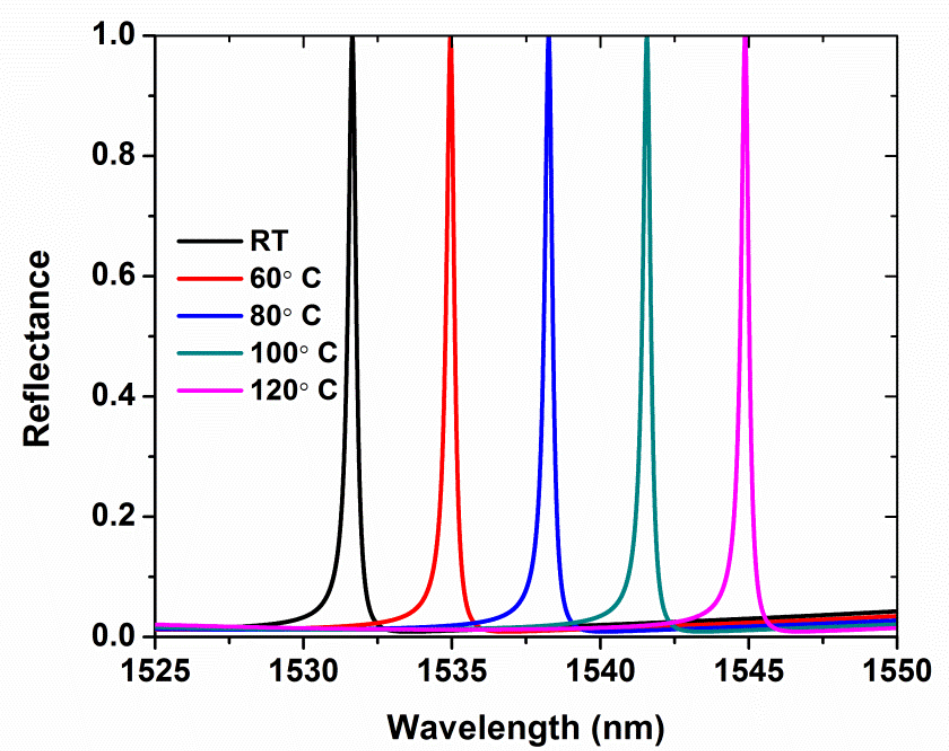

Figure 3-2 Spectral response of a thermo-optic tunable optical filter with a deep Si grating. Design parameters are: d_g = 110 nm, d_h = 335 nm, Λ = 900 nm, F =0.45, n = 3.73, and FWHM = 1.5 nm. Tuning range = 13 nm.

3.3.2 Shallow Grating Thermo-Optic Tunable GMR Filter

The FWHM and resonance wavelength of the deep-grating TOTOF strongly depends on the fill factor as discussed in Chapter 2. To avoid this dependency, an attempt is made to design a thin grating optical filter. Figure 3-3 shows the spectral response of the thin-grating TOTOF. The design parameters are: d_g = 10 nm, d_h = 460 nm, Λ = 676 nm, F = 0.5, n = 3.31. The FWHM of the designed filter is 1.0 nm.

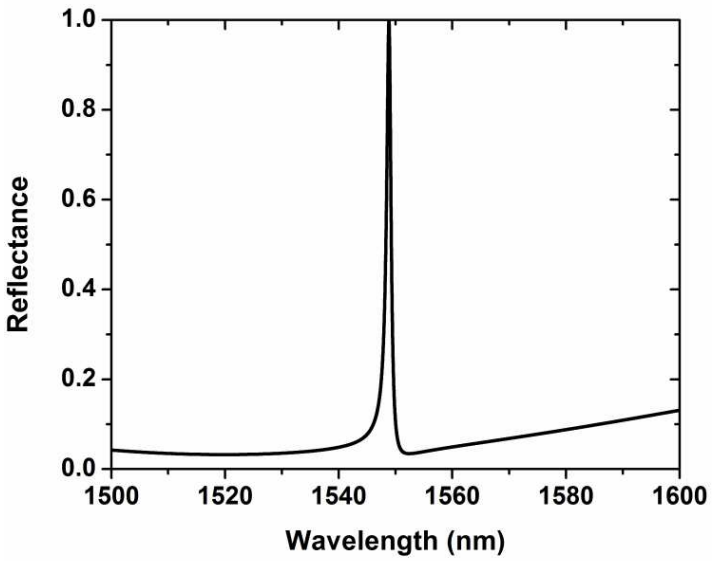

Figure 3-3 Narrow-band guided-mode resonant filter with shallow grating. Design parameters are: d_g = 10 nm, d_h = 460 nm, Λ = 676 nm, F =0.5, n = 3.31, FWHM = 1 nm.

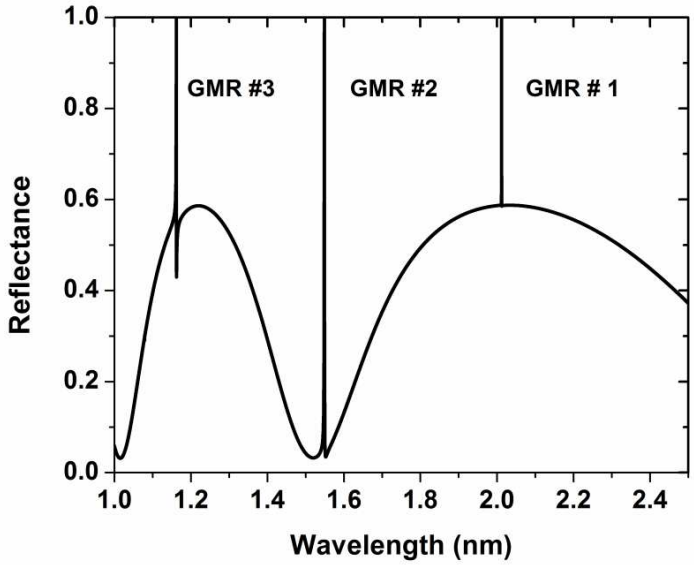

Figure 3-4 Guided mode resonances in a wide spectrum. Design parameters are: d_g = 10 nm, d_h = 460 nm, Λ = 676 nm, F = 0.5, and n = 3.31.

Figure 3-4 shows different resonances that occur in the subwavelength region. There are two resonances in the near subwavelength region and one resonance in the deep subwavelength region. In this thin grating structure, the GMRs arise via first-order coupling. Figure 3-5 gives the field plot associated with each resonance in Figure 3-4.

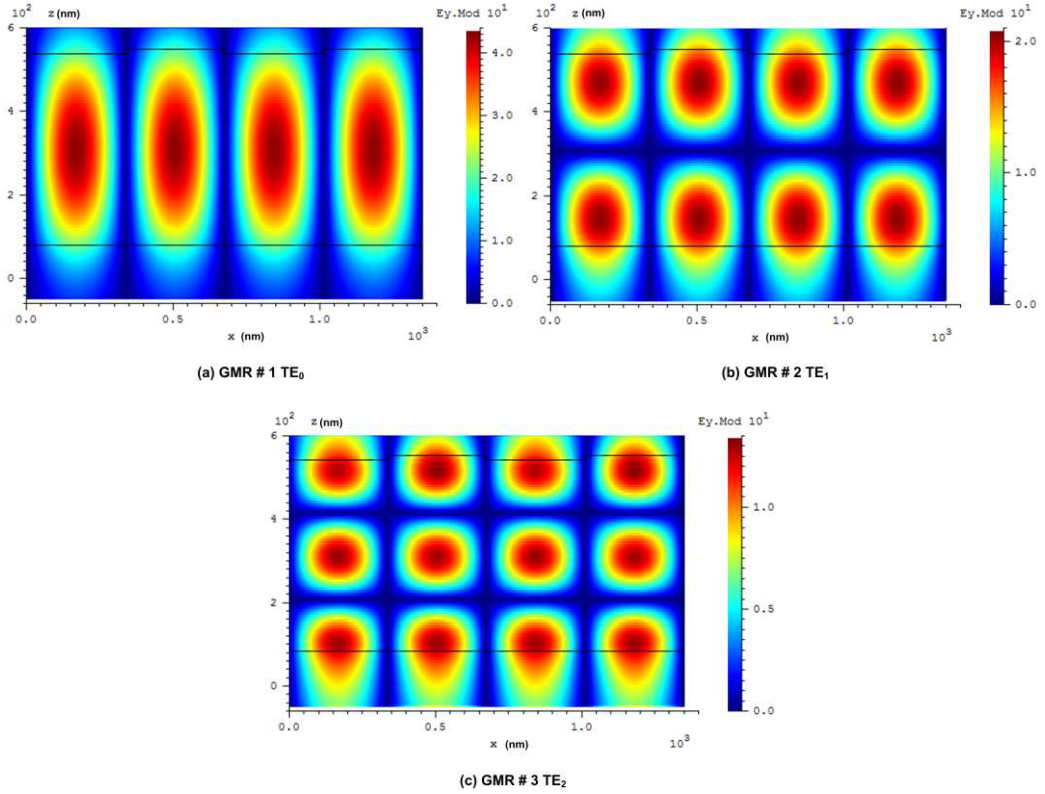

Figure 3-5 Field plots of the GMRs shown in Figure 1.4.1.2. GMR #1 is excited by a $TE_{1,0}$ mode, GMR #2 corresponds to a $TE_{1,1}$ mode and GMR # 3 relates to a $TE_{1,2}$ mode.

Figure 3-6 shows the spectrum pertinent to thermo-optic tuning of the shallow-grating TOTOF. We see a 10.2 nm wavelength tuning with an applied 100° C change in temperature.

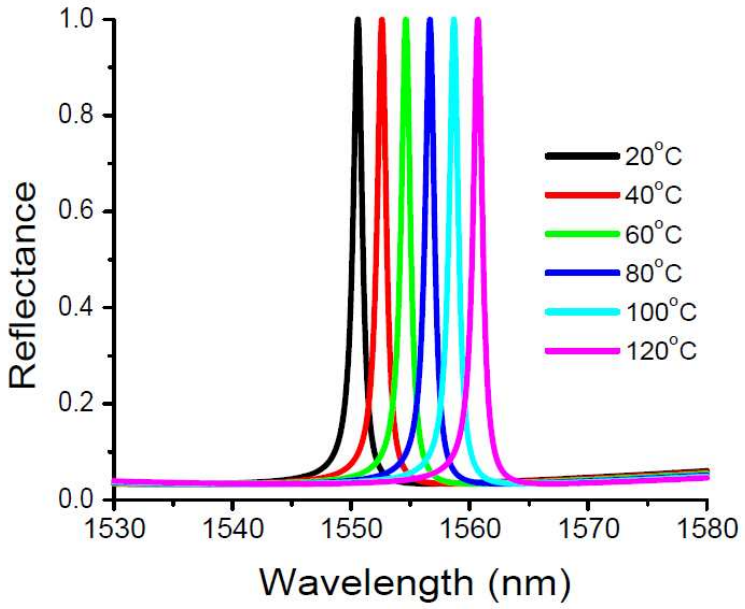

Figure 3-6 Spectrum of a of thermo-optic tunable optical filter with a shallow Si grating. Design parameters are: d_g = 10 nm, d_h = 460 nm, Λ = 676 nm, F =0.5, n = 3.31, and FWHM = 1 nm. Tuning range is 10.2 nm.

3.3.2.1 Fill Factor Variation

The behavior of the deep-grating TOTOF strongly depends on the fill factor. But for the shallow grating structure, we see a very little change of FWHM and resonance wavelength with the change of the fill factor. Figure 3-7 shows the reflectance map showing the minor effect of the fill factor on the resonance wavelength and FWHM. This is because the grating depth is only ~5% of the total thickness; the resonance is dominated by the homogenous layer.

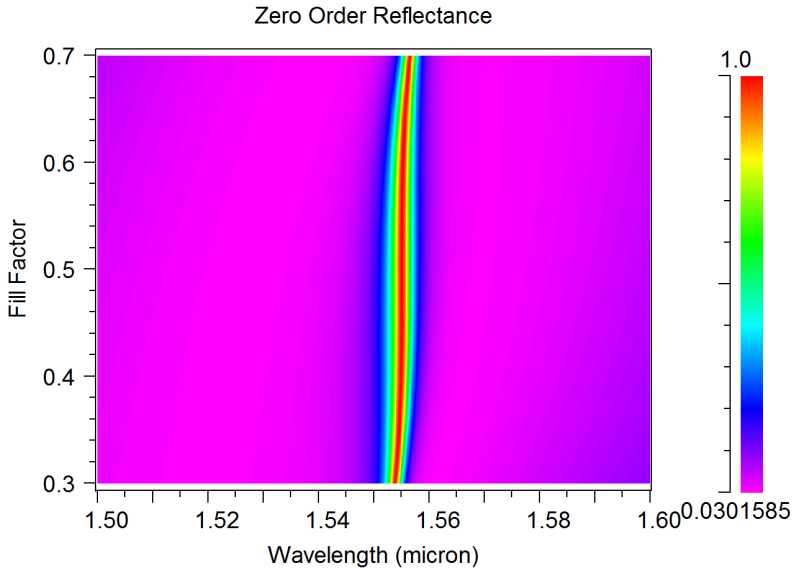

Figure 3-7 Reflectance contour map showing the dependency of the fill factor on resonance wavelength and FWHM. The device parameters for simulation are: d_g = 20 nm, d_h = 455 nm, Λ = 680 nm, n = 3.31.

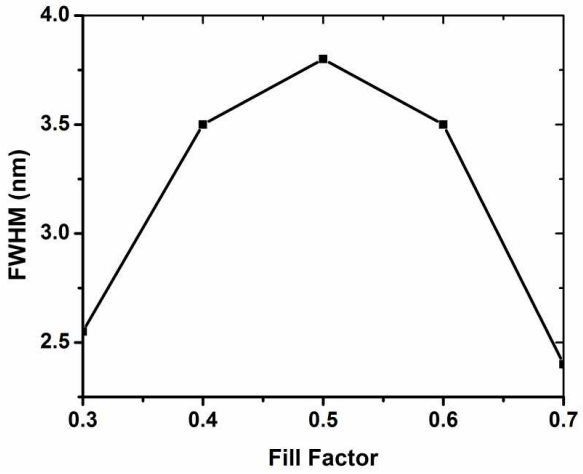

Figure 3-8 Relation between fill factor and FWHM for shallow grating. Device parameters for simulation are: d_g = 20 nm, d_h = 455 nm, Λ = 680 nm, n = 3.31.

Figure 3-8 shows quantitatively how the FWHM changes with the fill factor. Unlike the deep grating filter, the value of FWHM is maximum at 50 % fill factor. It decreases when F deviates from the value 0.5.

3.3.2.2 Variation of Grating Depth

Though the resonance wavelength and FWHM weakly depend on fill factor, they strongly depend on the grating thickness. Figure 3-9 shows the reflectance map of the shallow grating TOTOF for different grating depths. We observe that both the resonance wavelength and FWHM strongly depend on the grating depth. With the increase of grating depth, both of them increase. Figure 3-10 demonstrates the same phenomenon by their spectral response curves.

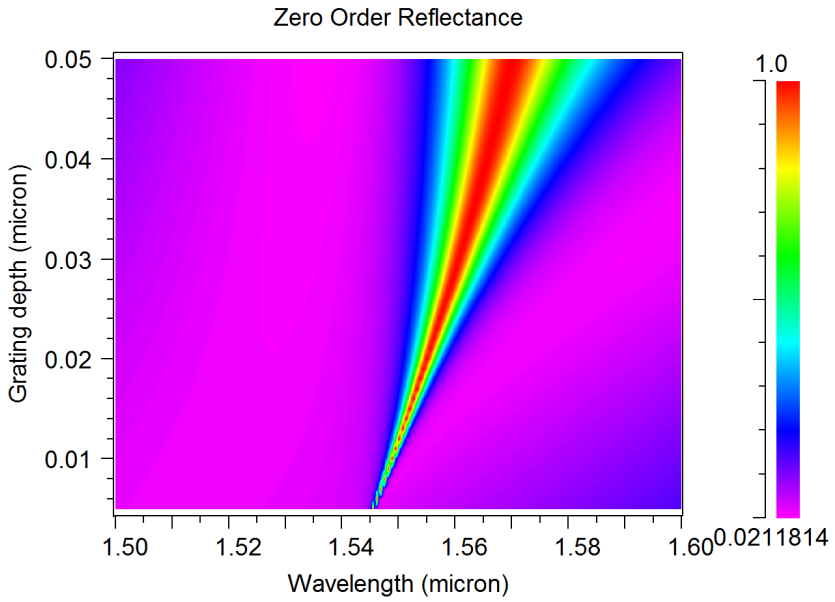

Figure 3-9 Reflectance contour map showing effect of grating thickness on the resonance spectra. Device parameters are: d_h = 455 nm, Λ = 680 nm, F = 0.5, and n = 3.31.

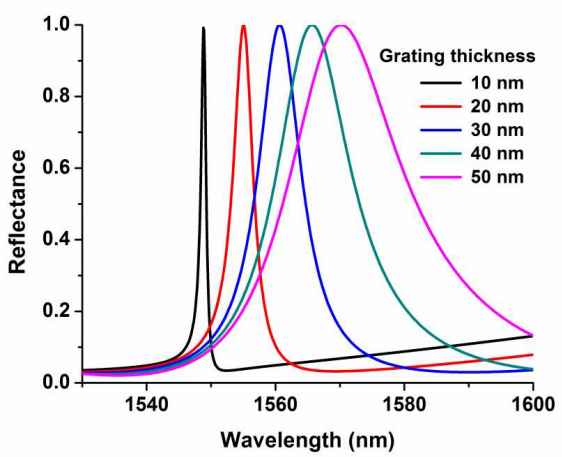

Figure 3-10 Effect of grating thickness on the resonance spectra. Device parameters are: d_h = 455 nm, Λ = 680 nm, F = 0.5, and n = 3.31.

3.3.2.3 Variation of the Thickness of Homogeneous Layer

Figure 3-11 shows that the variation of the homogeneous layer thickness does not change the FWHM a lot but it tunes the resonance wavelength effectively. We have to choose homogeneous layer thickness to get narrow bandwidth and lower sidebands.

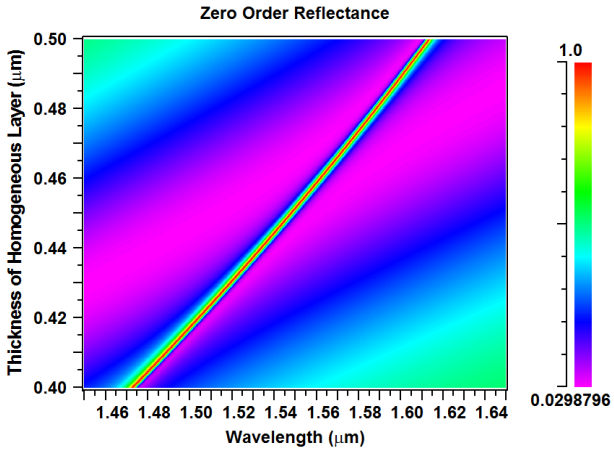

Figure 3-11 Reflectance contour map showing effect of homogeneous thickness on the resonance spectra. Device parameters are: d_g = 20 nm, Λ = 680 nm, F = 0.5, and n = 3.31.

3.4 Device Fabrication

We fabricated prototype thermo-optic tunable filters using deep and shallow Si gratings on glass substrate. Device fabrication starts with a-Si thin-film deposition on a cleaned glass substrate. We use two methods of deposition, namely plasma-enhanced chemical vapor deposition (PECVD) and sputtering. We use PECVD-deposited a-Si for deep grating filters and sputtered a-Si for shallow grating filters. For our equipments, the PECVD films are denser with a higher refractive index. The sputter-deposited a-Si films are more uniform with a lower refractive index than the PECVD-deposited a-Si. The ellipsometrically measured optical constants are shown in Figure 3-12 for PECVD deposited a-Si and in Figure 3-13 for sputter deposited a-Si.

We spin coat a bottom antireflective coating (BARC) followed by a photoresist (PR) layer. Thereafter, we record a periodic pattern using a laser interferometric lithographic (LIL) system where the interference of two laser beams exposes the PR. The BARC layer at the bottom edge of the PR pattern is removed using O_2 plasma. Then the PR pattern is transferred to the a-Si layer by reactive-ion etching using CHF_3 and SF_6 gas mixtures. After a-Si etching, the remaining PR and BARC layers are stripped by O_2 plasma followed by a nanostrip (90% H_2SO_4 and 5% H_2O_2) wet stripping and O_2 plasma ashing. We perform metallization to supply the electrical current for heating. For this purpose, we again spin coat 450 nm PR on the whole device. We selectively expose the structure to create an opening for metal deposition around the GMR device area and deposit 100 nm aluminum using sputtering. Then we remove the surplus metal over the PR mask using the lift-off method by soaking the sample in acetone. Lastly, copper tape is added as contact pad. Figure 3-1 (b) shows the top view of the device
A summary of the fabrication steps is given in Figure 3-14.

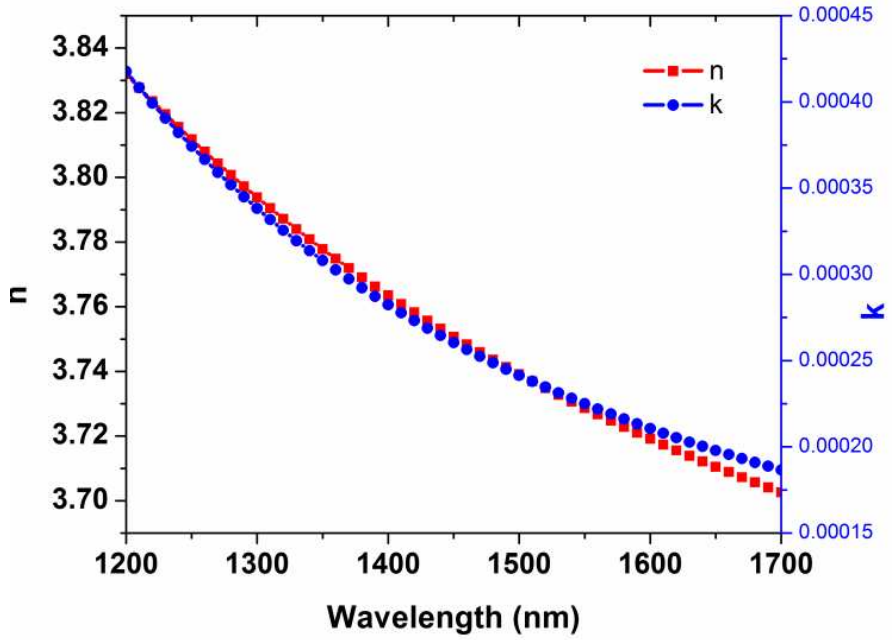

Figure 3-12 Ellipsometrically measured n, k values of PECVD deposited p-type a-Si.

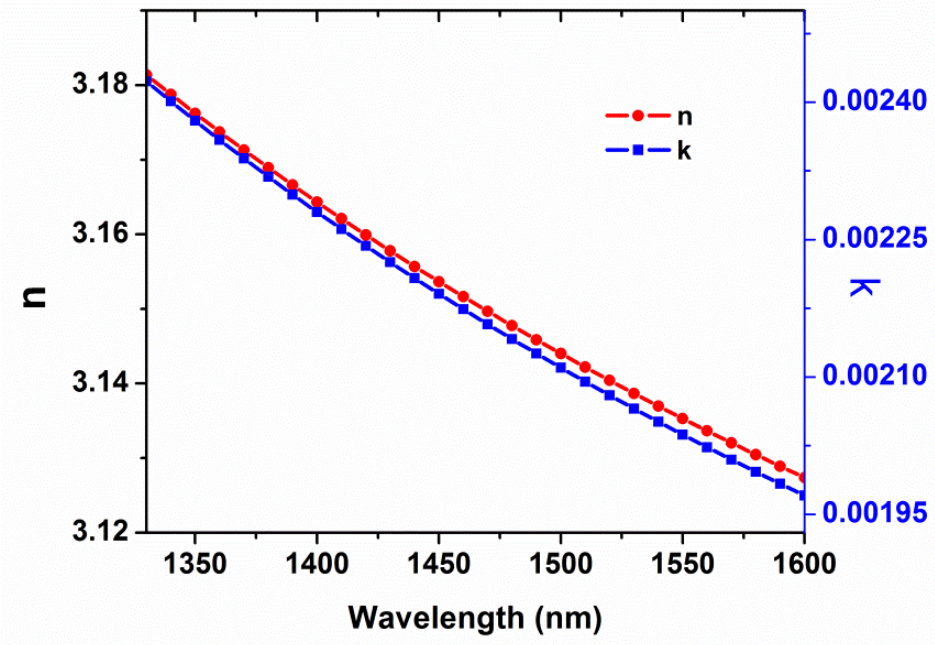

Figure 3-13 Ellipsometrically measured n, k values of sputter deposited a-Si.

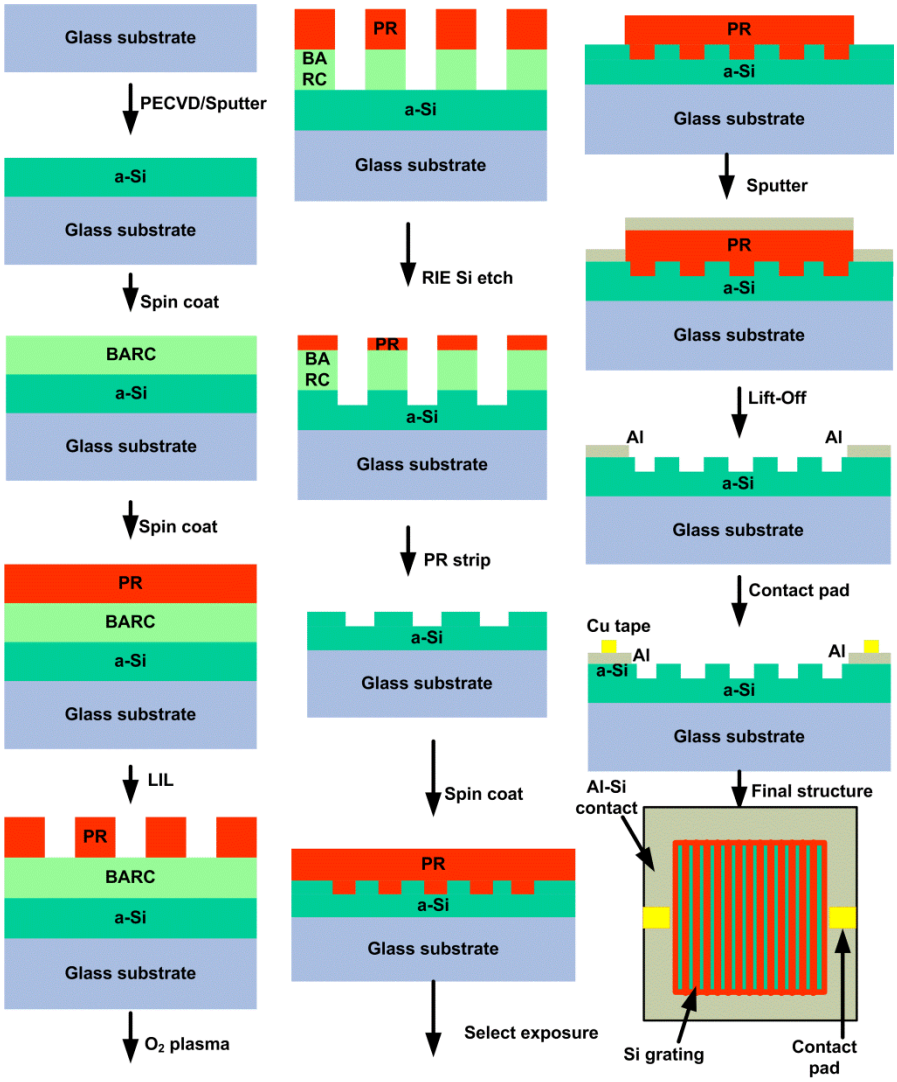

Figure 3-14 Summary of the fabrication steps from left top to bottom right.

3.5 Device Characterization

The device is characterized using an atomic force microscope (AFM) and ellipsometer. Ellipsometry gives the refractive index and thickness of the a-Si film. An AFM image provides the grating profile quantifying period, grating thickness, and the width of the grating ridges.

3.5.1 Deep Grating Tunable Filter

For deep grating filters, measured a-Si film thickness is 450 nm and refractive index is 3.73 at 1550 nm. Figure 3-15 shows the AFM image of a deep grating TOTOF. The device parameters from the AFM and ellipsometry measurements are d_g = 115 nm, d_h = 335 nm, Λ = 901 nm and F = 0.32.

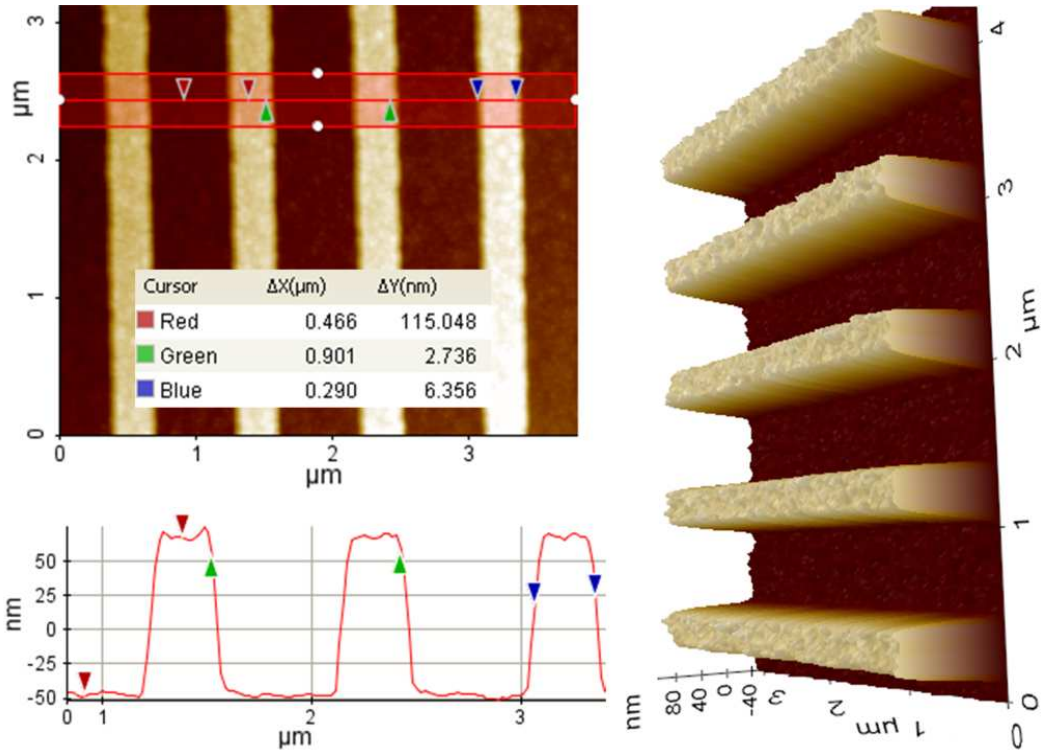

Figure 3-15 AFM image of the deep grating TOTOF. The device parameters are n = 3.73, d_g = 115 nm, d_h = 335 nm, Λ = 901 nm and F = 0.32.

3.5.2 Shallow Grating Tunable Filter

For shallow grating filters, the measured refractive index is 3.13 at 1550 nm and the a-Si film thickness is 520 nm. Figure 3-16 shows the AFM image of the shallow grating TOTOF. The device parameters from the AFM and ellipsometry measurements are d_g = 20.4 nm, d_h = 500 nm, Λ = 745 nm and F = 0.49.

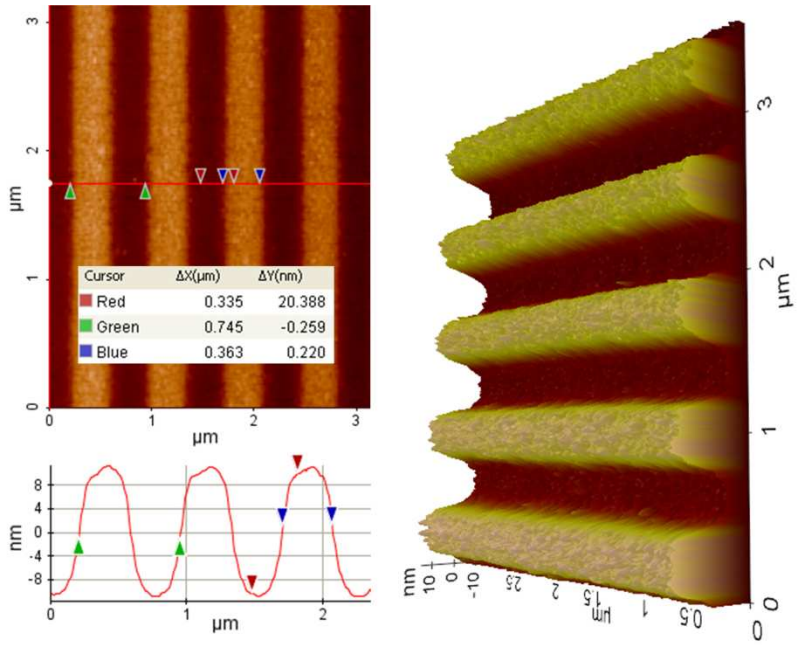

Figure 3-16 AFM image of the shallow grating TOTOF. The device parameters are n = 3.13, d_g = 20.4 nm, d_h = 500 nm, Λ = 745 nm and F = 0.49.

3.6 Results and Discussion

We use a Yokogawa spectrum analyzer and a Koheras SuperK Compact supercontinuum light source with a spectral range of 0.5–2.4 μm to measure the spectral behavior of the fabricated device. We use graded-index multi-mode fibers with a mode diameter of 400 μm to launch and collect light, which limits the resolution of the measurement to 2 nm. We use a polarizer to select the polarization state and lenses to collimate the input light and to focus the output light on the detection fiber. We calculate transmittance by normalizing the transmitted light intensity through the sample with that without the sample.

The period of the device is significantly smaller than the operating wavelength. Thus, it works in the subwavelength region with only zero-order transmitted and reflected

output light. For convenience, we measure zero-order transmittance T_0 and calculate the zero-order reflectance as $R_0 = 1 - T_0$. In the C and L communication bands, the loss in a-Si can be neglected.

3.6.1 Deep Grating Filter

Figure 3-17 compares the theoretical and experimental spectral response of the deep grating TOTOF that works in the C communication band and shows a matched center wavelength of the filter. The theoretical FWHM is 7 nm, and the experimental FWHM is 12 nm.

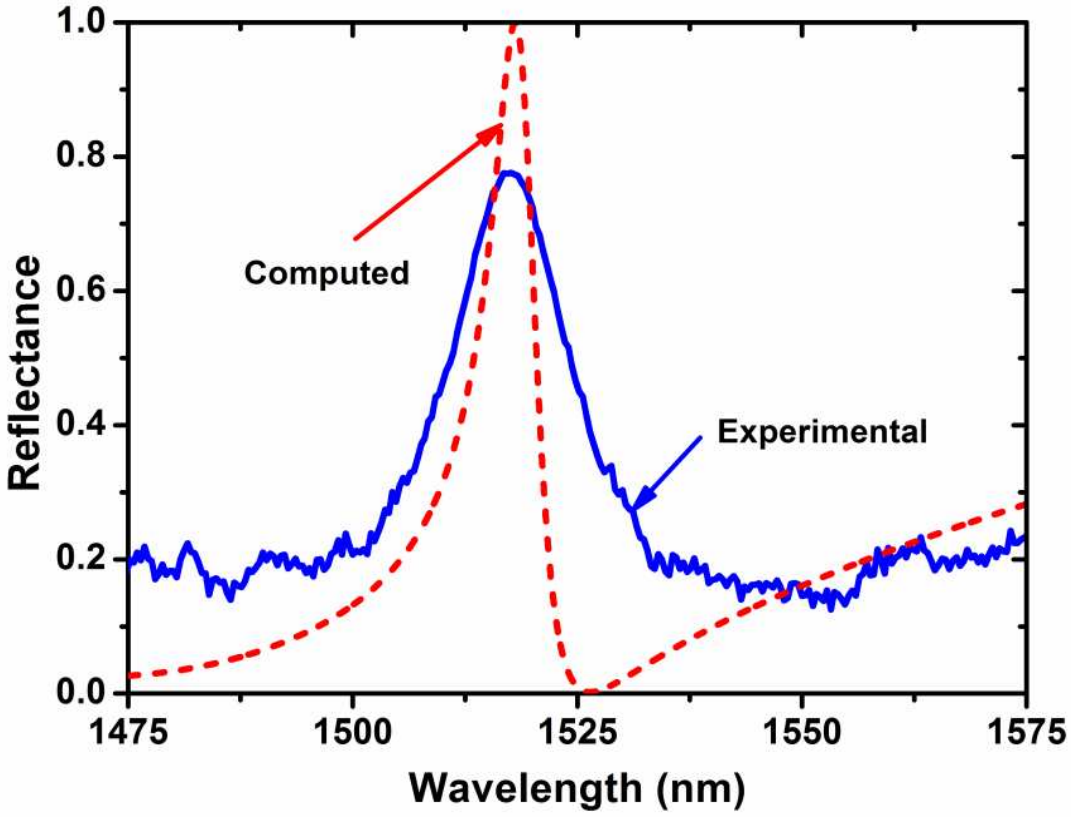

Figure 3-17 Comparison between experimental and computed spectral response of the deep grating TOTOF.

To match the center wavelengths in Figure 3-17, we slightly adjust the device parameters within estimated experimental tolerances. The parameters used for simulation are d_g = 115 nm, d_h = 335 nm, Λ = 895.5 nm, F = 0.25 and n = 3.73; these are close to the fabricated device parameters: dg = 115 nm, d_h = 335 nm, Λ = 901 nm, F = 0.32 and n = 3.73.

Figure 3-18 demonstrates the experimental thermo-optic tuning of this device. We observe a 15 nm tuning of the resonance wavelength by a 100℃ rise in temperature that gives a tuning efficiency of 0.15 nm/℃. We supply electrical current by a 12V variable voltage source. For every 10℃ increase of temperature, the applied electrical power is 0.2 W.

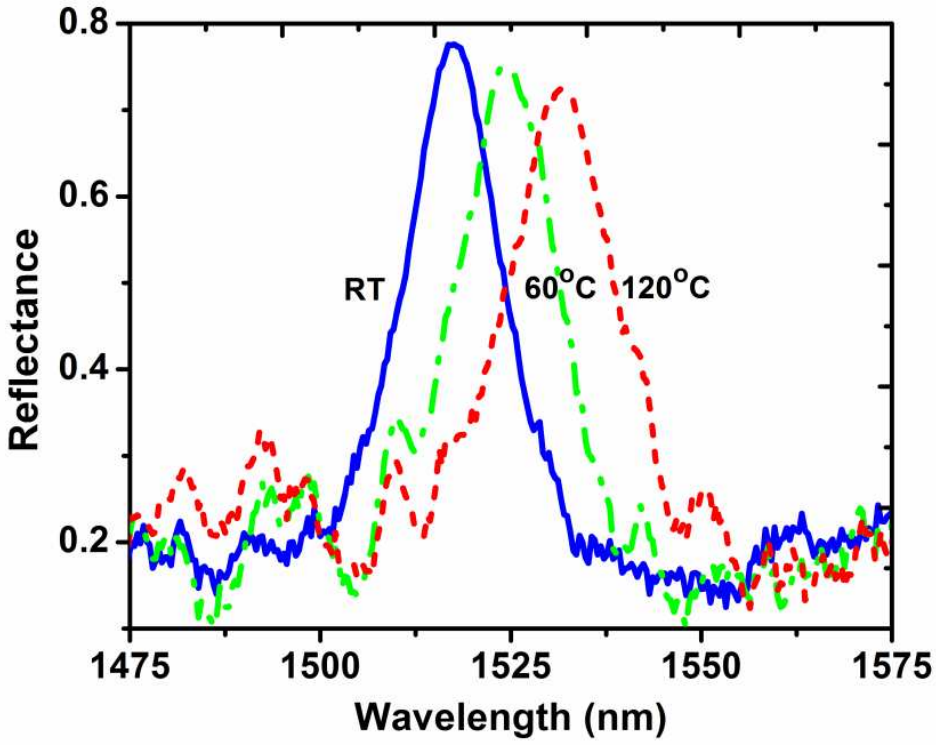

Figure 3-18 Tunable spectral response of the deep grating TOTOF under thermal variation.

3.6.2 Shallow Grating Filter

Figure 3-19 compares the theoretical and experimental spectral responses of the shallow grating TOTOF and shows a matched center wavelength of the filter. The theoretical FWHM is 3.1 nm, and the experimental FWHM is 7 nm in the L-band. Device parameters for the simulation are d_g = 20 nm, d_h = 500 nm, Λ = 750 nm, F = 0.5 and n = 3.12; these are close to the fabricated device parameters: d_g = 20.4 nm, d_h = 500 nm, Λ = 745 nm, F = 0.49 and n = 3.13.

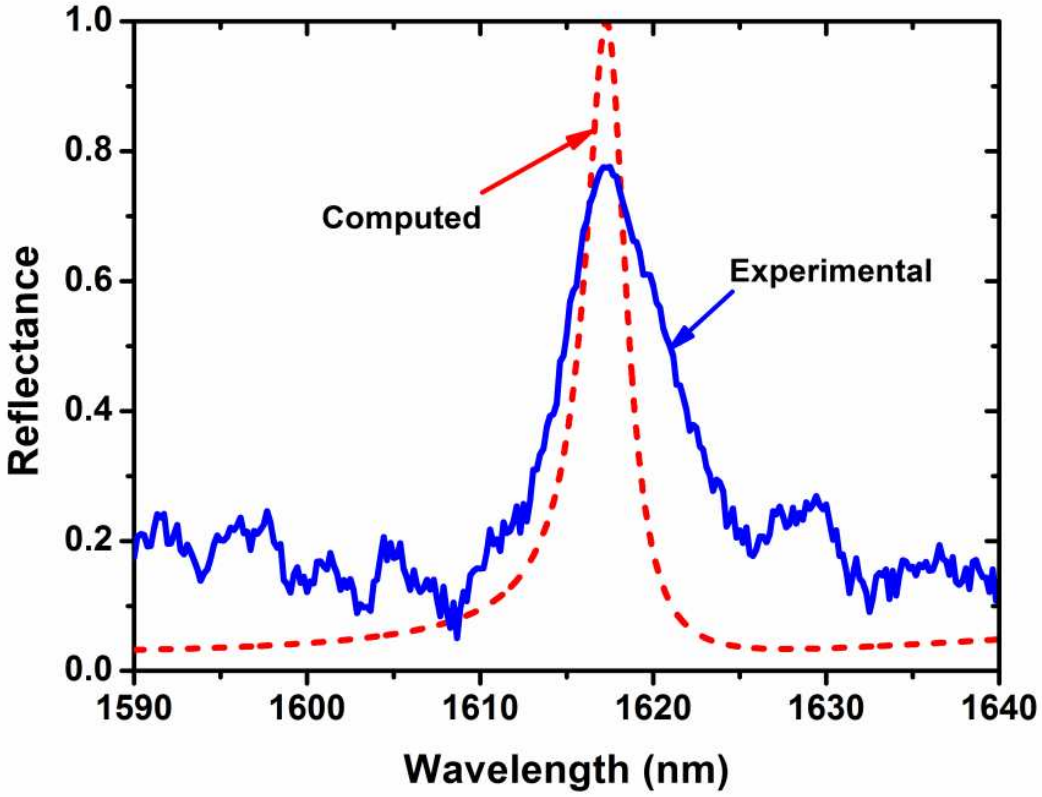

Figure 3-19 Comparison between experimental and calculated spectral response of the shallow grating TOTOF.

In Figures 3-17 and 3-19, we attribute the discrepancy between the measured and computed spectral linewidth to measurement error caused by a slight divergence of the light illuminating the sample. The asymmetry in the side bands and observed noise features arise from Fabry-Perot resonances in the substrate, collimation assembly and fiber coupling.

Figure 3-20 demonstrates the thermo-optic tuning of the shallow grating TOTOF. The device works in the L communication band. We observe a 12 nm wavelength tuning with 100℃ increase of temperature that gives a tuning efficiency of 0.12 nm/℃. The tuning range is comparable to that of published TOTOFs [62, 63].

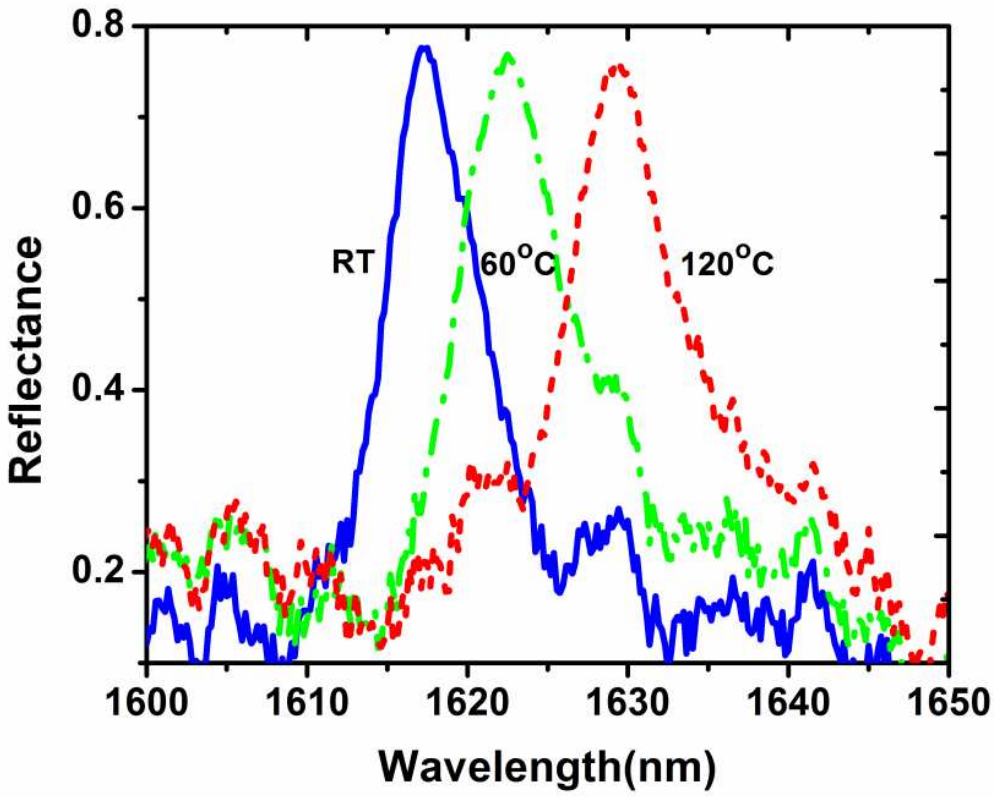

Figure 3-20 Spectral response of shallow grating TOTOF showing the tuning of resonance wavelength with the change of temperature.

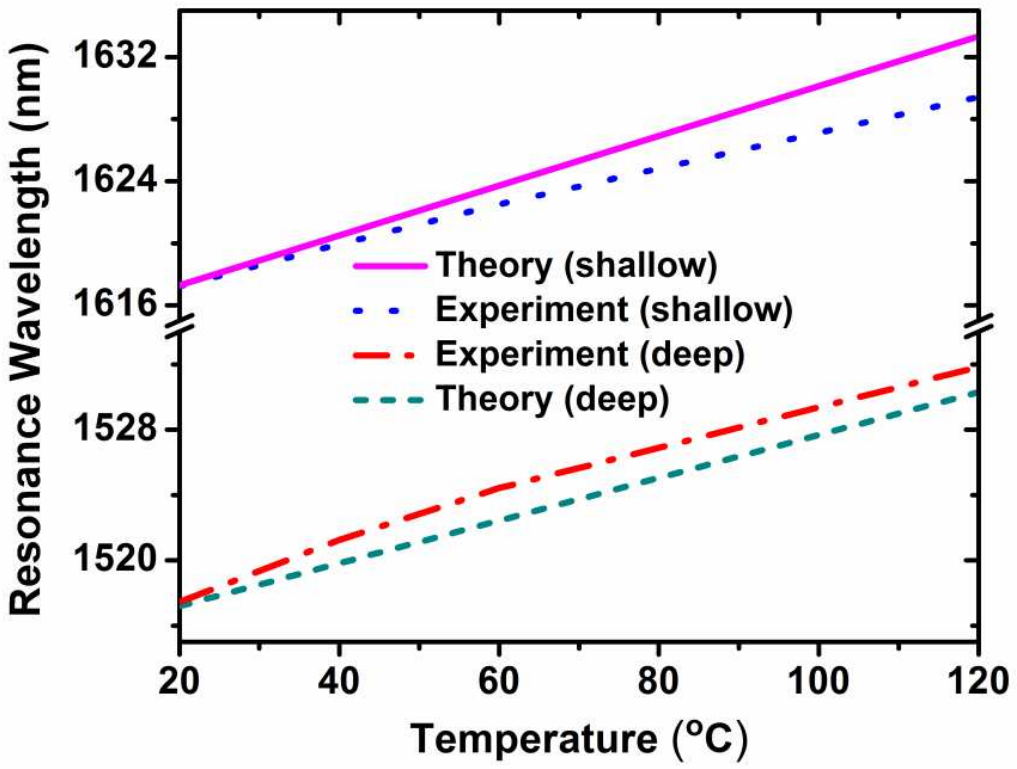

Figure 3-21 Shift of resonance wavelength with temperature variation: Theory and experiment.

Figure 3-21 shows the quantitative shift of the resonance wavelength with the change of temperature for both theory and experiment. For theoretical calculation, we consider only the thermo-optic effect of the a-Si. A constant thermo-optic coefficient of 3.25×10^{-4}/℃ [63] is used for the calculation. The discrepancy between the theory and experiment can be attributed to the slightly different thermo-optic coefficient of the a-Si of the fabricated device relative to that used for calculation.

3.7 Conclusion

GMR-based thermally tunable optical filters have been fabricated with deep and shallow gratings. The deep grating filter has a tuning range of 15 nm with a tuning efficiency of 0.15 nm/℃ working in the C communication band. The shallow grating filter shows a tuning range of 12 nm with tuning efficiency of 0.12 nm/℃ in the L-band. The filter is compact and easy to design and fabricate. It has reasonable tuning efficiency and is electrically controlled with no moving parts. Future work aims to reduce the spectral linewidth while obtaining higher efficiency and lower sidebands.

Chapter 4

Design and Fabrication of Angle-Tuned Resonant Color Filters

Novel tunable color filters based on the guided-mode resonance (GMR) principle are demonstrated experimentally. The devices are designed with numerical methods and patterned with laser interferometric lithography. Two types of tunable color filters with different tuning efficiency and direction are reported. They consist of a 55-nm-deep silicon nitride/air diffraction grating along with a 110-nm-thick silicon-nitride waveguide layer deposited on a glass substrate. The fabricated filter exhibits three primary colors at three different incident angles, with reasonably high efficiency and narrow bandwidth.

4.1 Introduction

Color filters are useful for display devices, image sensors, and many other applications. Common display devices include televisions, computer monitors, mobile phones, projectors, and electronic paper. Image sensors are integral parts of digital cameras. Liquid crystal displays are widely used often with dye-based color filters, which transmit a particular color while absorbing the undesired surrounding spectral components under white-light illumination [67]. Problems with this filter type include low transmission efficiency, heating due to absorption of light, and imperfect color purity. Attempts to improve color filter technology have led to research on diffractive color filters [68–77]. The theory of separating colors using phase gratings is presented in [68, 69]. The grating material can be a semiconductor (silicon) [70, 71]; metal (aluminum) [72–75]; dielectric (nitride/oxide) [76, 77]; or a polymer [78].

Both transmissive and reflective display technologies incorporating color filters are used in practice. Transmission color filters based on silicon and aluminum [70–75]

exhibit low efficiency due to absorption loss in the visible spectral region. Dielectric GMR reflective filters can have high efficiency with narrow bandwidth favorably impacting input light utilization and color purity [79].

Recently, Wang et al. provided computed results pertaining to a reflection-type color filter array using the GMR principle [77]. Prior to that, Kanamori et al. reported GMR color filters with experimental reflection efficiency of ≈ 50% [78]. These results ([71–75], [77], and [78]) were obtained by deploying multiple physical filters (one filter per color) in which pixels with different grating periods produce individual colors.

In this study, we report the design and fabrication of dielectric GMR-based tunable reflective color filters in which a single pixel is used to produce three primary colors using angular tuning. We discuss the structure and theory of basic GMR filters and their application as color filters. We describe fabrication steps, measured device parameters, and spectral measurement results. We achieve high experimental efficiency and narrow bandwidth with good agreement between experimental and theoretical data. We demonstrate two types of angle-tuned color filters. In one filter, with the change of angle, the response moves from blue to red; it is termed a red-shift color filter. In the other filter, the response moves from red to blue with the change of angle; it is denoted a blue-shift color filter.

4.2 Structure and Device Parameters

Our tunable GMR pixel consists of a subwavelength silicon nitride grating along with a silicon nitride homogeneous waveguide layer on a glass substrate. The device layers and parameters are shown in Figure 4-1, where d_g denotes grating depth, d_h homogeneous layer thickness, F fill factor, Λ period, I incident light wave, T_0 zero-order transmittance, R_0 zero-order reflectance, θ_i incident angle, and θ_o angle of zero-order

reflected light. As the period of the grating is chosen to be significantly smaller than the wavelengths defining the visible spectral range, the device works in the zero-order diffraction regime. A GMR takes place when diffracted light from the grating structure is coupled with a leaky waveguide mode satisfying the phase-matching condition; as a result, a sharp resonance peak is observed at a particular wavelength. The details of GMR filter operation are explained in [20]. The position of the resonance wavelength can be tuned by changing the refractive index, period, thickness, incident angle, and incident light polarization as discussed in [20, 21].

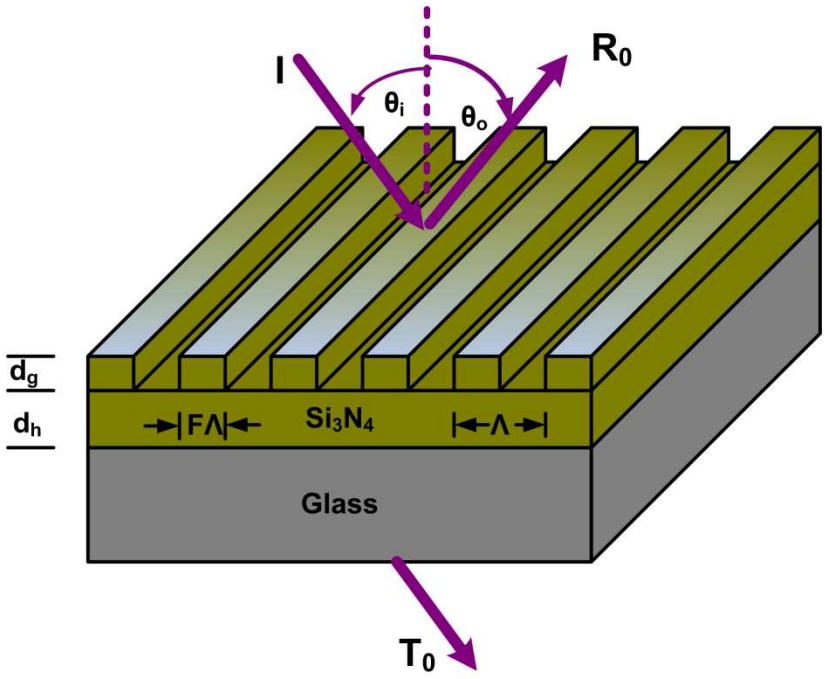

Figure 4-1 Basic structure of GMR based TCF. d_g = grating depth, d_h = homogeneous layer thickness, Λ = period, F Λ = width of the high index region, F = fill factor, I = incident light wave, T_0 = zero-order transmittance, R_0 = zero-order reflectance, θ_i = incident angle, and θ_o = angle of zero-order reflected light.

4.3 Design of Angle-Tuned GMR Color Filters

At normal incidence, GMRs are excited simultaneously by evanescent orders +1 and -1, +2 and -2, and so forth. At oblique angles, the resonances are generally excited by a single order such as +1 or -1. These orders produce different resonance wavelengths, which is geometrically quite clear. In 1993, so called resonance regimes were defined as reported in [21]. An example resonance regime plot is shown in Figure 4-2 for a selected set of parameters.

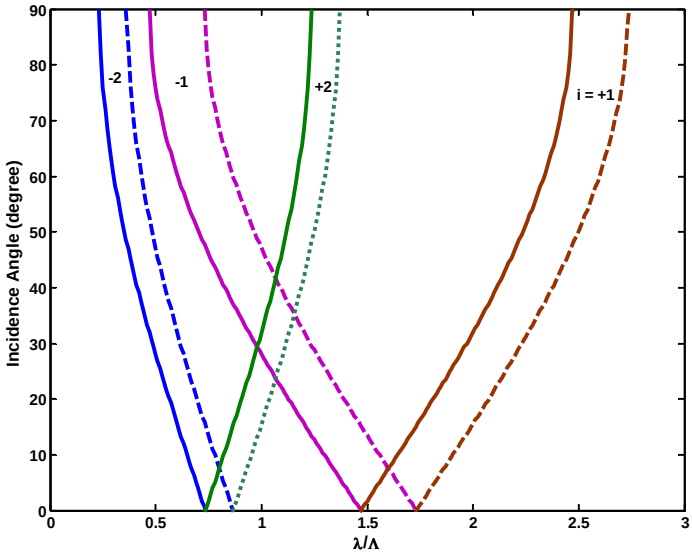

Figure 4-2 Resonance regime showing resonance splitting at off-normal incidence. The device considered for the simulation is a waveguide grating with average index, n_{avg} = 1.732; cover index, n_c = 1, substrate index, n_s = 1.47.

For color filter applications, upon oblique incidence, we design the filter such that one resonance falls outside the visible wavelength range and thus outside the human color perception. In this study, we design two filters: red and blue-shift angle-tuned color filters.

4.3.1 Red-Shift Angle-Tuned Color Filter

For the red-shift TCF, we choose design parameters such that normal incidence resonance wavelength is close to blue wavelength. In this case, when we change the incident angle, one resonance moves toward the smaller wavelength (UV) and falls outside the visible range and has no effect on the eye's color perception. The other resonance moves toward the longer wavelength realizing a blue-to-red pixel shift by the change of incident angle. Figure 4-3 shows such a design where at an angle of 24°, one resonance is at 360 nm which is out of the visible range and other wavelength is in the 550-nm green wavelength range.

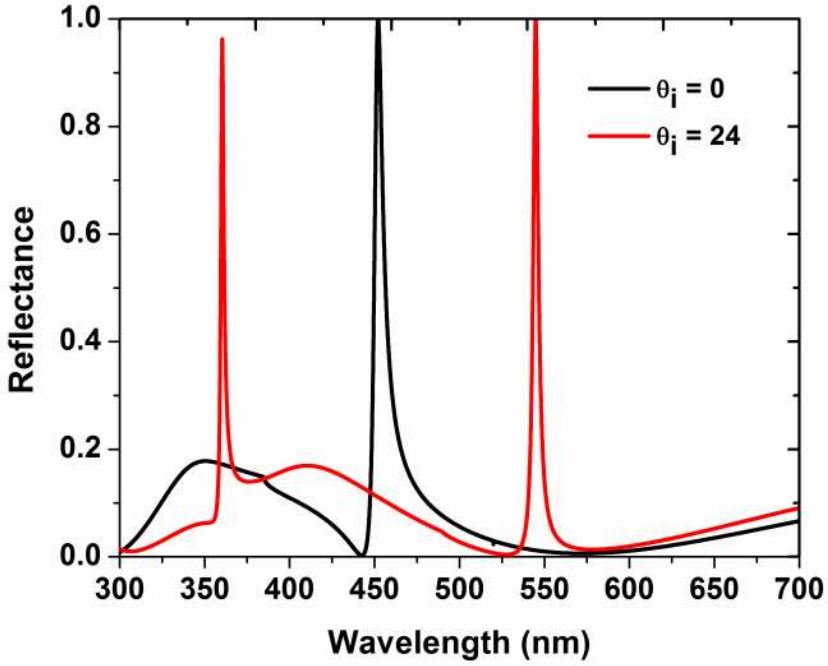

Figure 4-3 Resonance splitting of red-shift angle-tuned color filter at off-normal incidence showing one resonance falling outside the visible region. Design parameters are: d_g = 55 nm, d_h = 110 nm, Λ = 260 nm, n = 2.02, and F = 0.5.

As usual, we design the device using our RCWA-based [13, 15] MATLAB code and RSoft software. We do the forward parametric scans using RSoft to find the parameters for a desired spectral response. Figure 4-4 shows the design of an angle-tuned red-shifted CF. The pixel shows a blue color response at an incident angle of 7°, a green color response at an angle of 24°, and a red color response at an angle of 42°. A total of 35° angular offset is required to tune the color from blue to red.

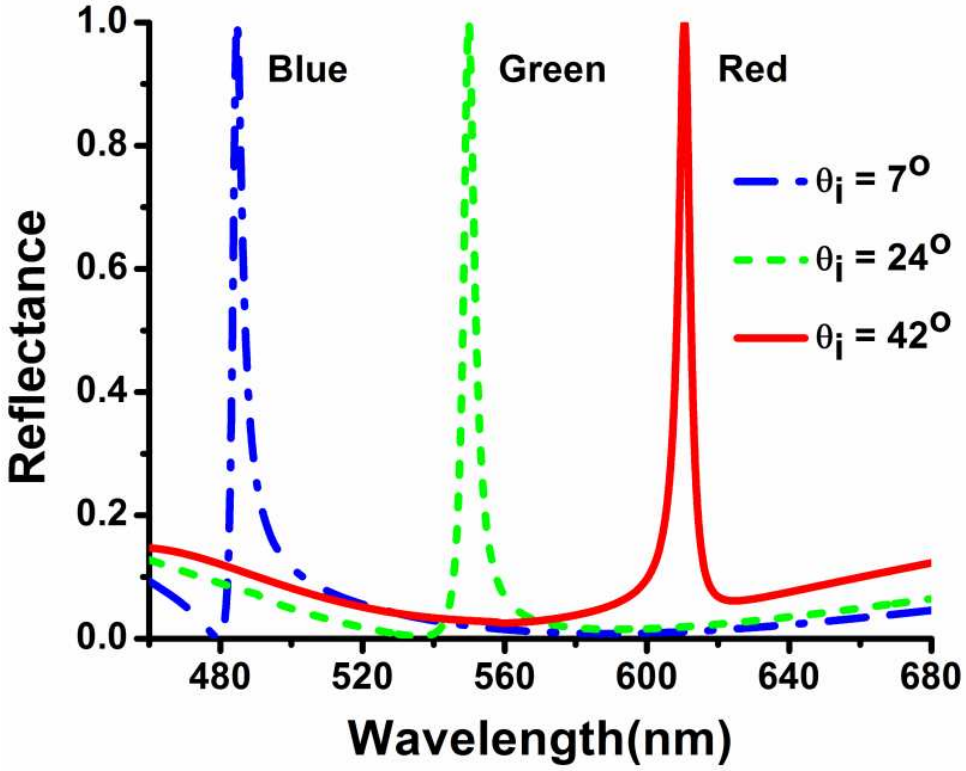

Figure 4-4 Spectra for the designed red-shift angle-tuned color filters. Blue to red pixel shift occurs at an angular movement of 35 degrees. Grating parameters are: d_g = 55 nm, d_h = 110 nm, Λ = 260 nm, and F = 0.5. Angular offset needed = 35 degrees.

4.3.2 Blue-Shift Angle-Tuned Color Filter

For the blue-shift TCF, we choose design parameters such that the normal incidence resonance wavelength is close to the red wavelength. In this case, when we change the angle, one resonance moves toward the higher (IR) wavelengths and falls outside the visible range and has no effect on color perception. The other resonance moves toward the lower wavelength and we obtain a red-to-blue pixel shift by the increase of the incident angle. Figure 4-5 shows such a design where at an angle of 8°, one resonance is at 725 nm which is out of visible range and other wavelength is near the 625-nm red wavelength.

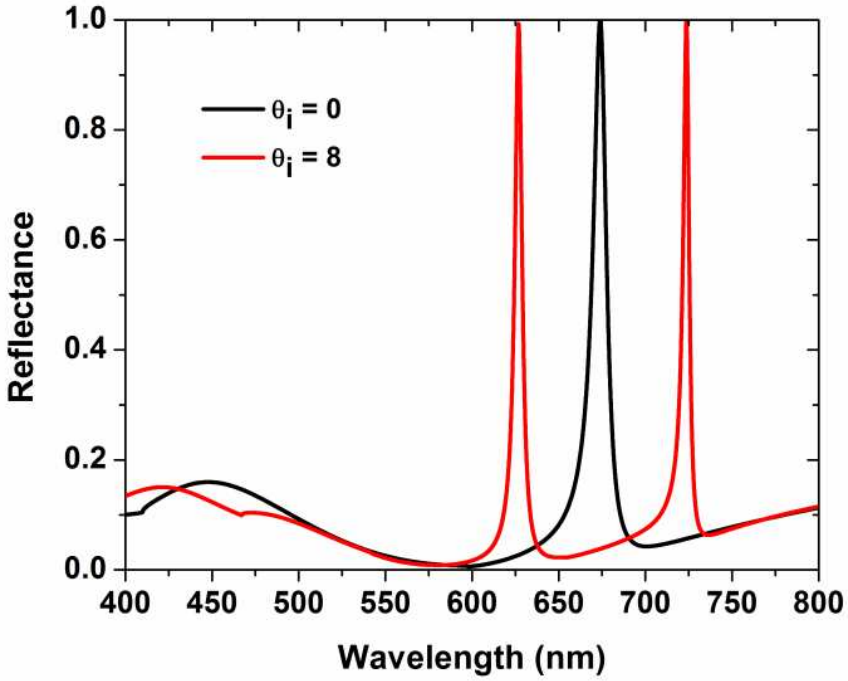

Figure 4-5 Resonance splitting of the blue-shifted angle-tuned CF. At off-normal incidence, one resonance falls outside the visible region and the other falls within it. Design parameters are: d_g = 55 nm, d_h = 110 nm, Λ = 410 nm, n = 2.02, and F = 0.5.

Figure 4-6 shows the designed spectral response of the blue-shift angle-tuned CF. The design parameters are listed in the figure caption. The pixel exhibits a red-to-blue color shift under angular variation of 25°.

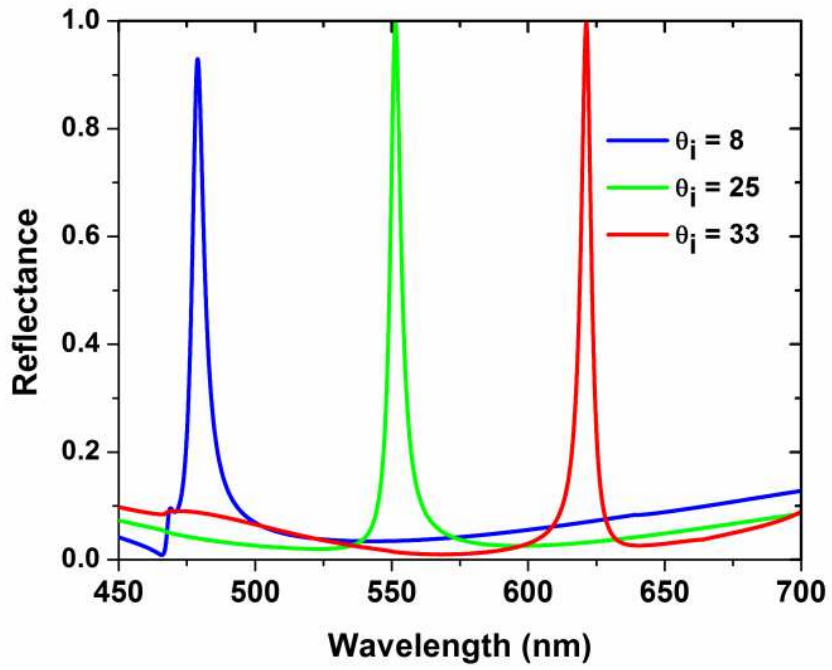

Figure 4-6 Spectrum of the designed blue-shift angle-tuned color filters. Grating parameters are: n = 2.0, d_g = 55 nm, d_h = 110 nm, F = 0.45 and Λ = 410 nm.

The angular offset needed for realizing blue-shift angle-tuned filter is 10 degrees less than that of the red-shift filter. This can be be explained by the following relation, which is derived from the grating equation [20, 21].

$$\frac{d\lambda}{d\theta} \propto \Lambda$$

where λ is the resonance wavelength, θ is the incident angle and □ is the period of the device. We see that the change of resonance wavelength with angular variation is

proportional to the device period. The blue-shift color filter has a larger period and therefore needs a smaller angular offset to cover the same spectral shift.

4.4 Device Fabrication and Characterization

The principal fabrication steps include thin-film deposition, lithographic patterning, and reactive-ion etching (RIE). Device fabrication starts with silicon nitride (Si_3N_4) film deposition on a cleaned microscopic glass substrate using a sputtering system. The optical constants and thickness of the film are measured using ellipsometry and found to be n = 2.02 and k = 2 x 10^{-4} at 550 nm wavelength with the film thickness being 165 nm. Figure 4-7 shows the ellipsometrically measured n, k values of the sputter deposited Si_3N_4 for the visible wavelength range.

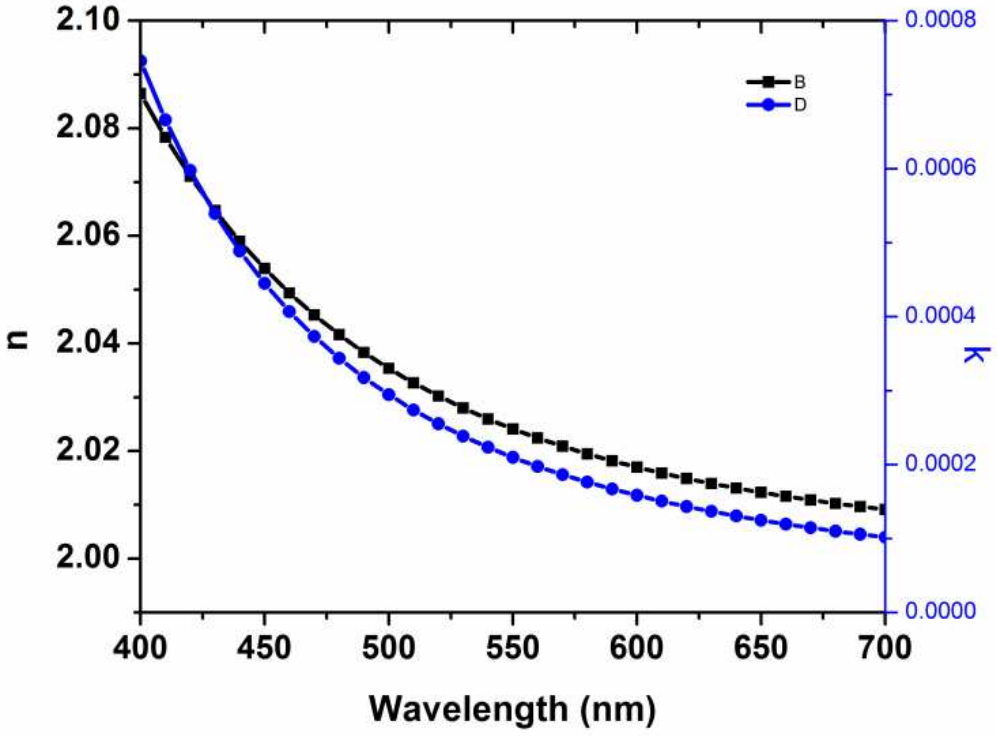

Figure 4-7 Result ellipsometric measurements of sputter-deposited Si_3N_4 film for red-shift TCF. It has n = 2.02 and k ≈ 2.5 × 10^{-4} at λ = 550 nm.

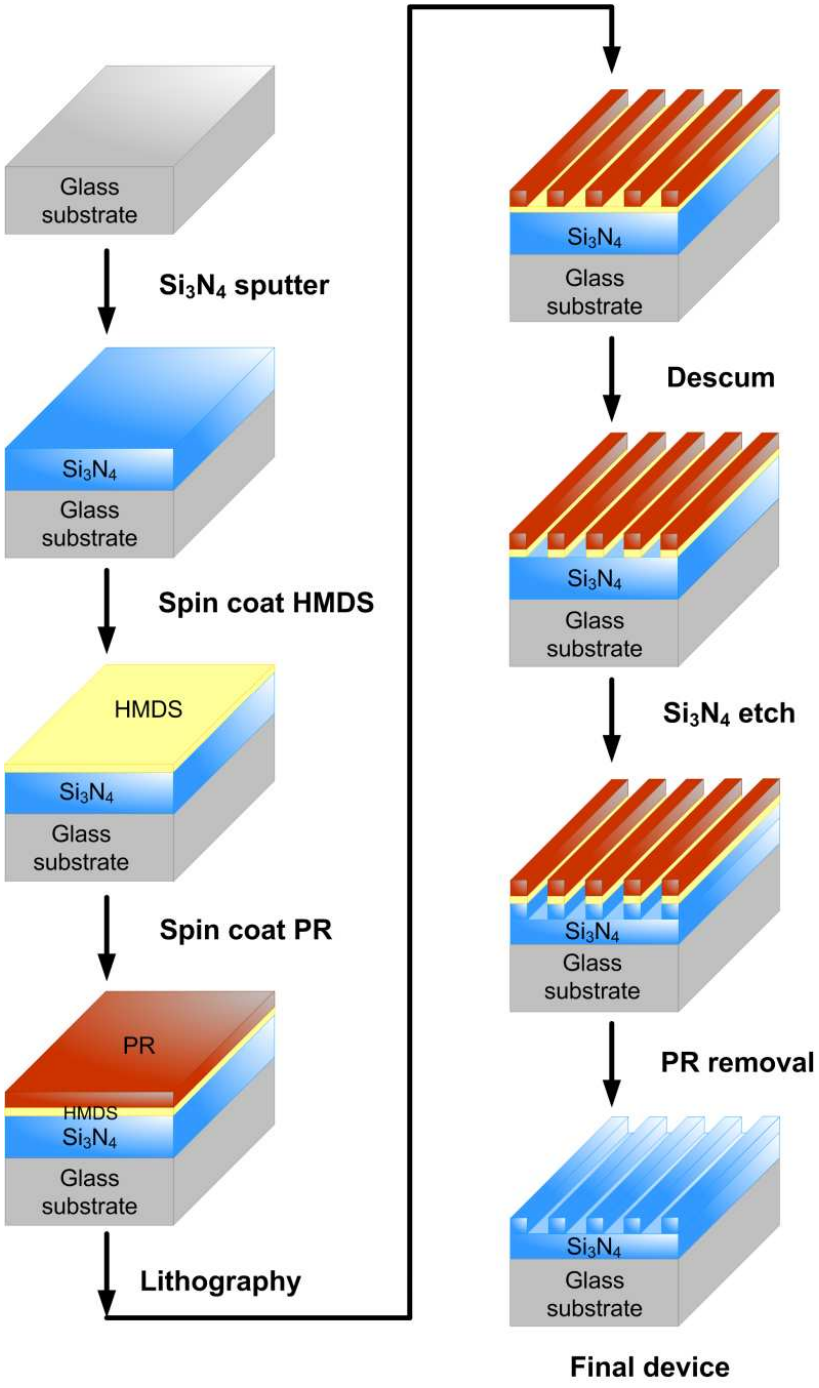

Figure 4-8 Summary of the fabrication steps for tunable color filters.

Thereafter, a 300-nm-thick positive photoresist (PR) is spin coated and a 1D grating pattern is recorded using an interferometric lithography system. To increase the adhesion of the PR to the nitride film, a hexamethyldisiloxane (HDMS) primer is spin coated and baked before the application of the PR. To etch the nitride film, we use RIE involving a gas mixture of trifluromethane (CHF_3) and oxygen (O_2). A short 10 s descum recipe using O_2 plasma is run before the etching step. After RIE, a thin PR film still exists on the nitride grating and it is stripped using O_2 plasma. Wet cleaning with nanostrip (90% H_2SO_4 and 5% H_2O_2) ensures that no PR remains on the nitride grating. Figure 4-8 shows the summary of the steps used to fabricate the angle-tuned color filters. The same steps are used to fabricate both the red and blue-shifted angle-tuned color filters.

4.4.1 Red-Shift Tunable Color Filter

To characterize the red-shift color filter we use SEM and AFM image along with the ellipsometric data. We use AFM images to extract the device parameters such as period and grating depth. Once we know the grating depth, we can calculate the homogeneous layer thickness by subtracting the grating thickness from the total film thickness. From the AFM image in Figure 4-9, the grating profile parameters are: d_g = 55 nm, Λ = 268 nm, F = ≈ 50%.

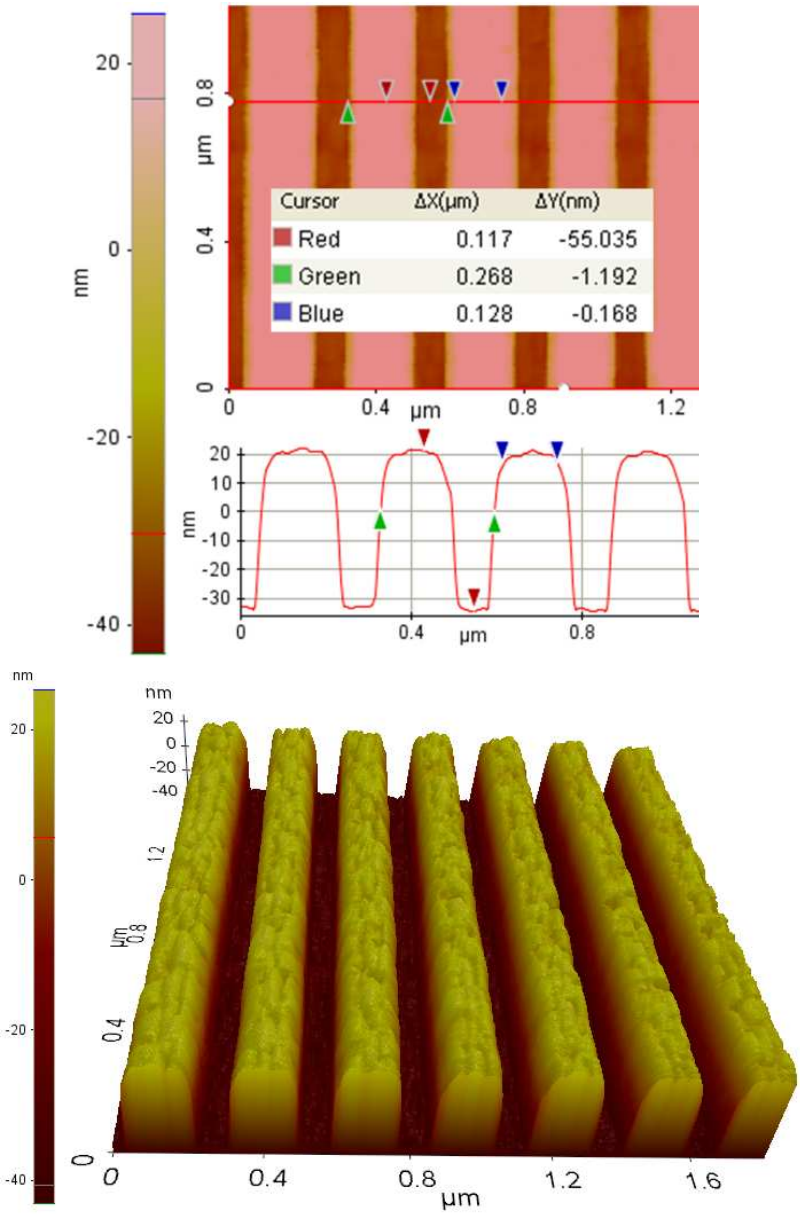

Figure 4-9 AFM image of the fabricated device. From the AFM image, d_g = 55 nm, Λ = 268 nm, F = 50%.

The homogeneous waveguide thickness can also be measured using the cross-sectional image of the SEM. The SEM image gives more accurate grating width and waveguide thickness due to its high magnification capability. Figure 4-10 gives the SEM

image of the fabricated red-shift tunable device. The device parameters from the SEM image in Figure 4-10 are: d_g = 63 nm, Λ = 273 nm, d_h = 115 nm, F = 44%.

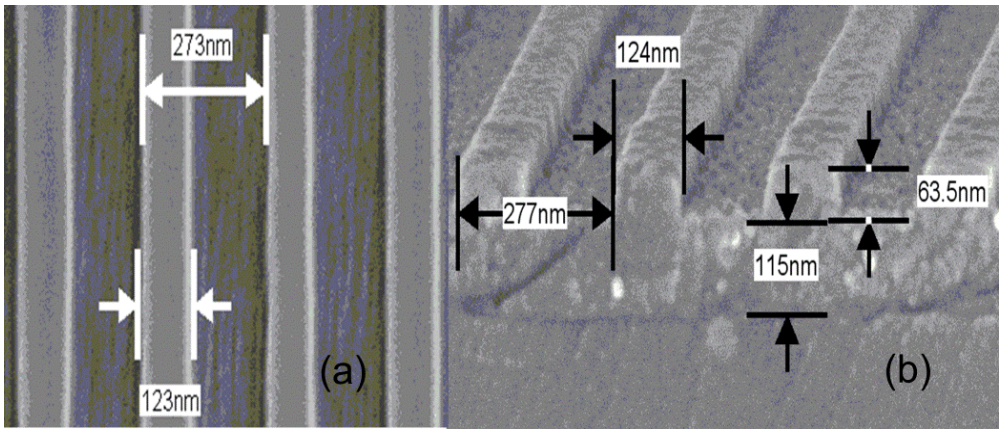

Figure 4-10 SEM image showing device parameters: d_g = 63 nm, Λ = 273 nm, d_h = 115 nm, and F = 0.44.

From the AFM and SEM data, the device parameters are found to be $d_g \approx 55$ nm, $d_h \approx 115$ nm, $\Lambda \approx 268$ nm, and $F \approx 0.45$. The fabricated device parameters are close to the initial design parameters. The effective pixel size can be calculated using the decay length of the leaky waveguide mode. The decay length is approximately [18],

$$L_d \approx \frac{\Lambda\lambda}{4\pi\Delta\lambda}$$

where $\Delta\lambda$ is the spectral linewidth of the color filter. Using this equation, we estimate the decay length as ~2 μm. Thus, this pixel should work well with 10×10 μm^2 lateral dimensions. The fabricated device presented here is considerably larger (5×5 mm^2) for convenience of characterization and spectral measurement.

4.4.2 Blue-Shift Tunable Color Filter

The grating profile of the fabricated blue-shift angle-tuned color filter device is characterized by AFM and ellipsometry data. Figure 4-11 gives the AFM image of the fabricated device. From the AFM image and the ellipsometry data, the device parameters are d_g = 57.3 nm, d_h = 107.7 nm, Λ = 418 nm, and F = 0.49; these are close to the original design parameters.

For the red-shifted filter, the period of the designed device was 260 nm. The period is taken to be small so that the normal incidence resonance stays below the blue wavelength. With this period, and for F = 0.4, the process linewidth, or feature size, is approximately 100 nm. If we use a blue-shift filter, the normal incidence resonance wavelength should be kept above the red wavelength so that under angular tuning we get red, green, and blue pixels. To keep the normal incidence resonance above the red color, the designed period is chosen to be 420 nm. This gives the feature size of the process ~210 nm for F = 0.4, which is twice that of the red-shift color filter. With larger features, we have more process flexibility and easier device fabrication using the laser interferometry lithography system.

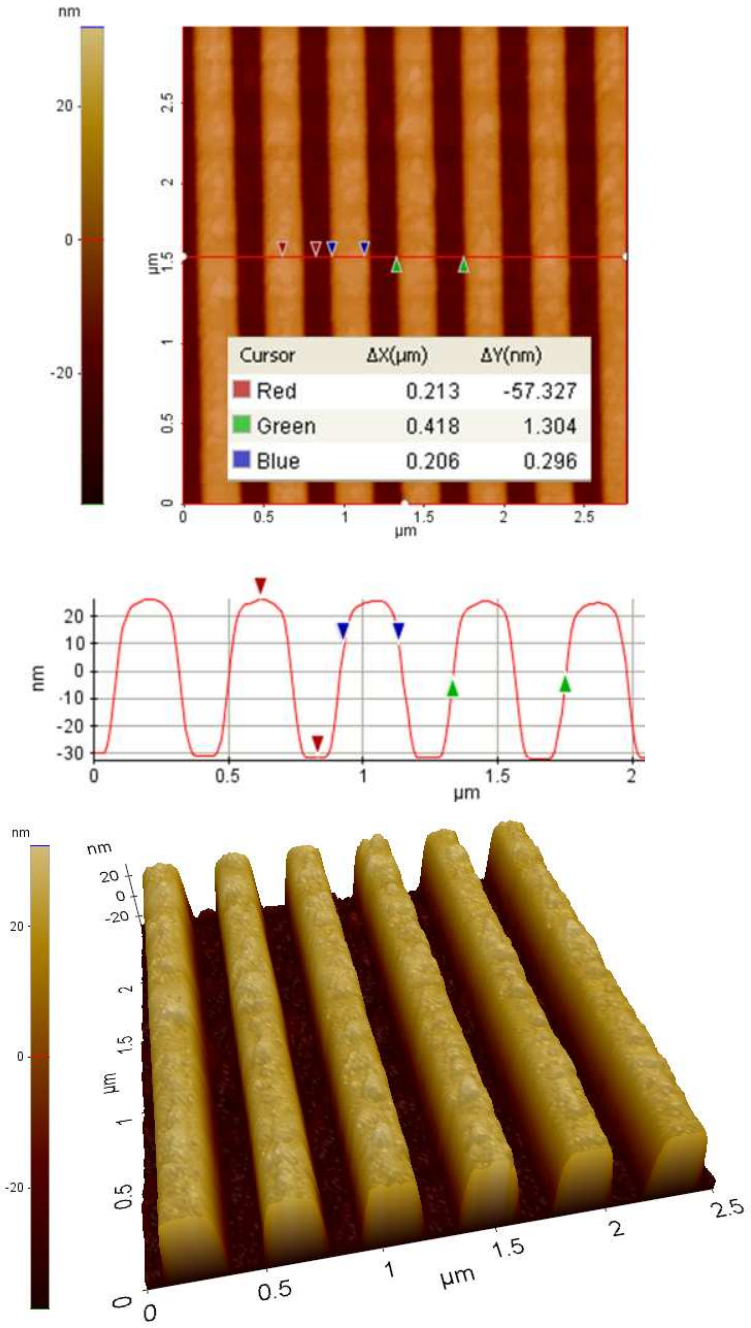

Figure 4-11 AFM image of the fabricated angle-tuned blue-shift color filter: The device parameters from the AFM image are: d_g = 57.327 nm, Λ = 418 nm, and F = 0.49.

4.5 Spectral measurement

The spectral response of the fabricated color filter is measured using a spectrum analyzer. A tungsten halogen lamp with a wavelength range of 360–1100 nm serves as a light source. A polarizer is mounted in front of the light source to select a specific polarization state. We use TE polarized light in which the electric field vector is normal to the plane of incidence and along the grating grooves in Figure 4-1. The angular tuning of the device is achieved by rotating the sample stage to the desired angle.

In commercial device application of angle-tuned color filter, a synchronized mirror can be used along with the sample so that the reflected light always goes to a fixed detector point. If the synchronized mirror is rotated at the same angle as the sample, light always goes to the same point at the eye. Figure 4-12 shows such an arrangement.

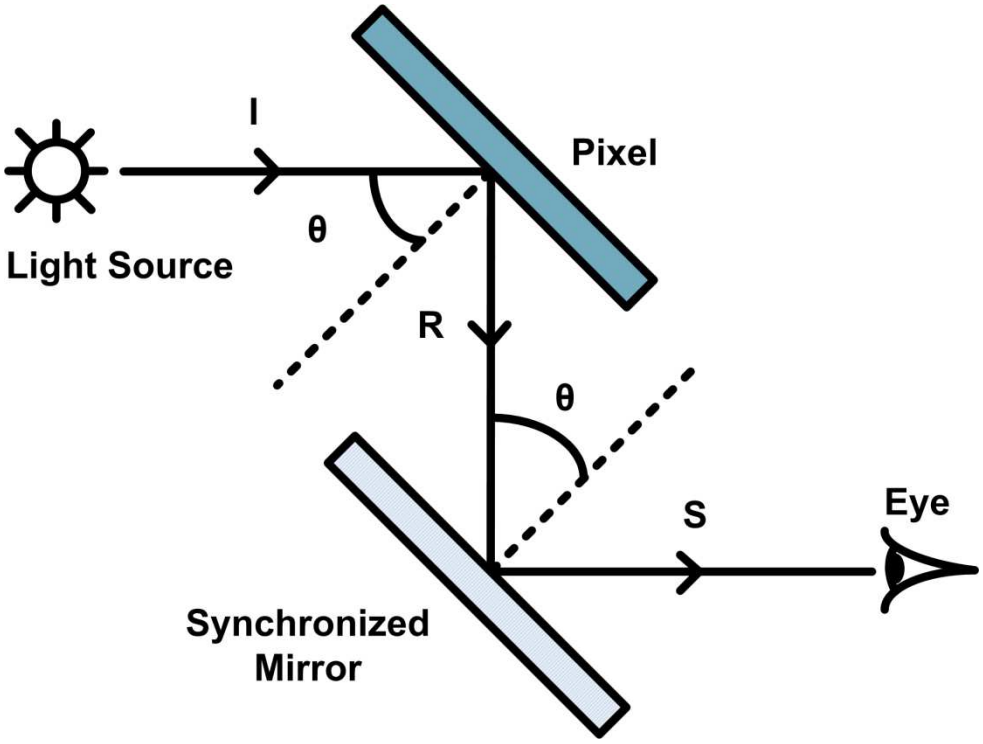

Figure 4-12 Arrangement to direct the reflected light always to a fixed point with a synchronized mirror.

4.5.1 Spectral Measurement of Red-Shift Tunable Filters

Figure 4-13 demonstrates the spectral response of the red-shifted tunable pixel at $\theta_i = 20°$. It compares the original design with experimental and simulation results. We observe a 15-nm resonance shift between the design and experimental spectra due to deviation of the fabricated-device parameters relative to the original design. The simulated spectrum using the experimental device parameters matches the experimental result well with the main discrepancy in the sideband levels.

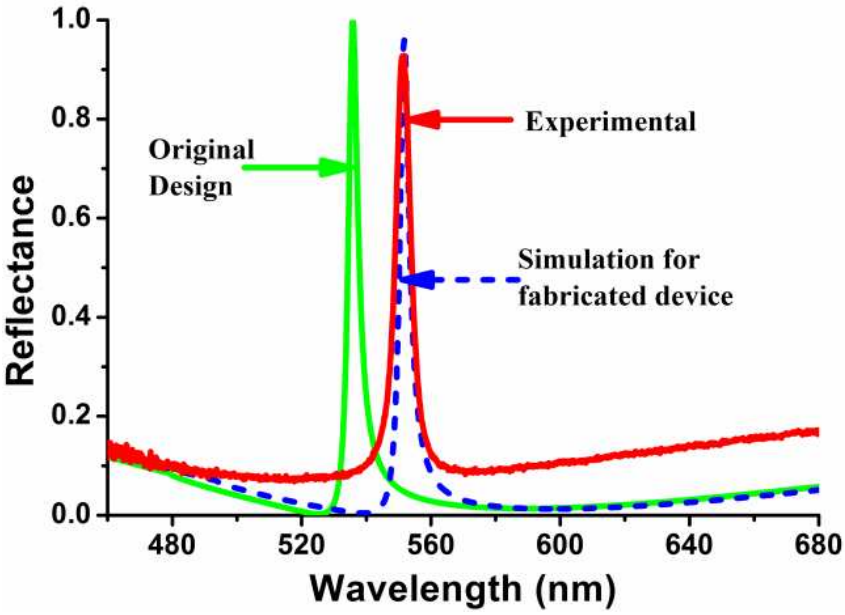

Figure 4-13 Spectral response of the color filter for θi = 20° showing comparison between the design, experimental results, and simulation results. Fabricated device parameters are: $d_g \approx 55$ nm, $d_h \approx 115$ nm, $\Lambda \approx 268$ nm, and $F \approx 0.45$. Designed device parameters are: $d_g = 55$ nm, $d_h = 110$ nm, $\Lambda = 260$ nm, and $F = 0.5$.

Figure 4-14 shows the pixel response under angular tuning. We observe blue, green, and red pixel response for incident angles of 8°, 20° and 35°, respectively. For these angles, the center wavelengths reported here for blue, green, and red are 505 nm, 551 nm, and 607 nm, respectively. The bandwidth of the pixel is approximately 10 nm,

which is 5 to 8 times narrower than reported in published experimental results for transmission filters [70–75] and ~x2 narrower than reported results in [78]. The filter has high reflection efficiency of 95% for red, 92% for green, and 88% for blue, considerably exceeding the experimental efficiencies of transmission filters [70–75] and reflection filters [78] reported previously.

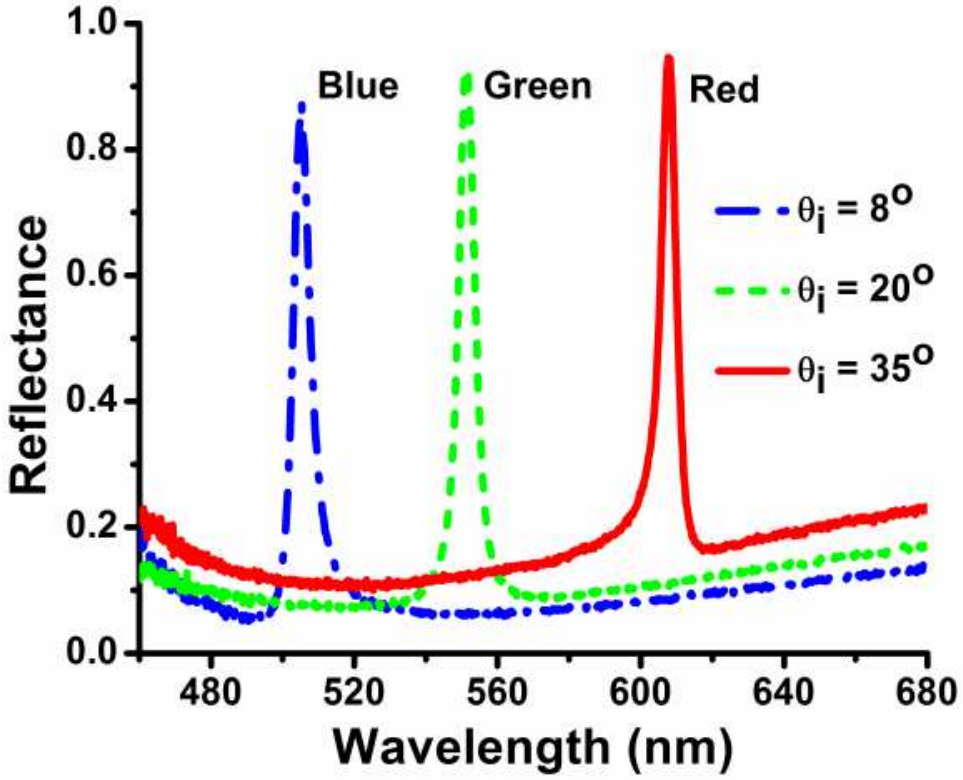

Figure 4-14 Experimental spectral response of the tunable color filter showing blue, green, and red color output with incident angles of 8°, 20°, and 35°, respectively.

4.5.2 Spectral Measurement of Blue-Shift Tunable Filters

Figure 4-15 compares the theoretical and experimental spectral response of the color filter showing a green pixel response. We get a reasonable match between the experimental results and the simulated data. The fitting parameters are d_g = 55 nm, d_h =

100 nm, Λ = 411.5 nm, and F = 0.45, which are close to the fabricated device parameters: $d_g \approx 57$ nm, $d_h \approx 108$ nm, $\Lambda \approx 417$ nm, and $F \approx 0.45$.

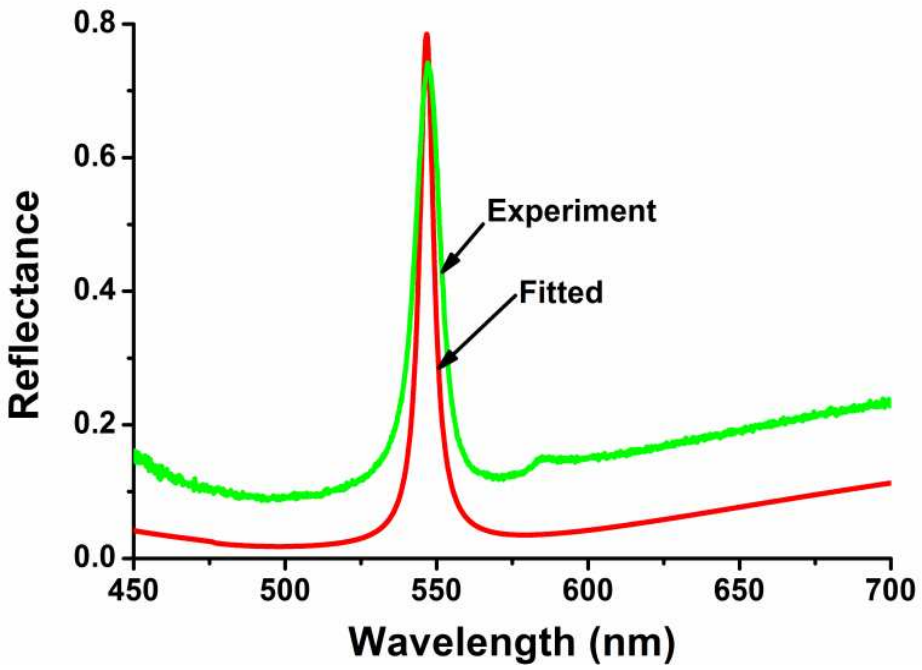

Figure 4-15 Spectral response of the color filter for $\theta_i = 20°$ showing comparison between experimental and fitted results. Fitting parameters are: $d_g = 55$ nm, $d_h = 100$ nm, $\Lambda = 411.5$ nm, and $F = 0.45$. Experimental device parameters are: $d_g \approx 57$ nm, $d_h \approx 108$ nm, $\Lambda \approx 417$ nm, and $F \approx 0.45$.

Figure 4-16 shows the color filter response under angular tuning. We observe a red to blue pixel shift with an angular tuning of 25 degrees. The device has FWHM of 10 nm and efficiency of 75%.

The efficiency of the blue-shift color filters is not as good for the red-shift filters. The reason behind this can be attributed to the nitride quality, which is lossy with a higher k value in the order of 10^{-3}. The fabricated pattern is not also as smooth as that for the red-shift filter. With improved nitride and more precise fabrication, this result can be improved.

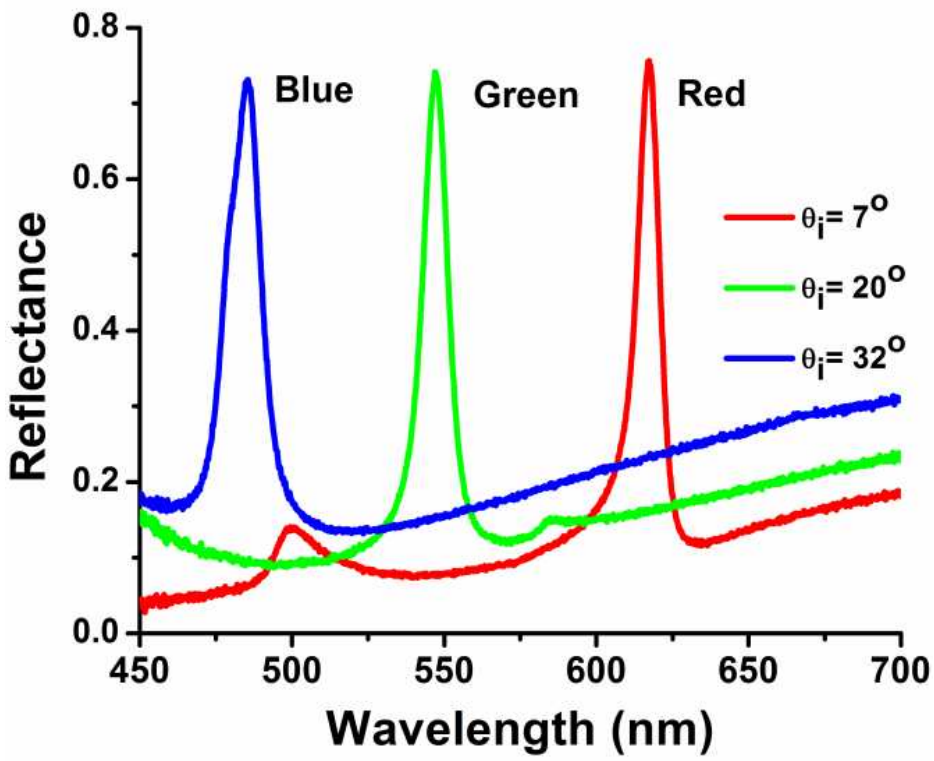

Figure 4-16 Experimental RGB pixel demonstration using angular tuning. Experimental device parameters are: $d_g \approx 57$ nm, $d_h \approx 108$ nm, $\Lambda \approx 417$ nm, and $F \approx 0.45$.

4.6 Conclusion

New reflection-type tunable pixels are designed and fabricated using subwavelength silicon-nitride waveguide gratings on glass substrate. Two alternate ways namely red- and blue-shift tunable pixels are demonstrated. The basic pixel separates incident TE-polarized white light into its three primary colors (red, green, and blue) that appear at different incidence angles. It exhibits high efficiency as well as high color purity due to narrow bandwidth. Its size can be as small as 100 μm^2. We find a good match between the experimental data and theoretical simulation results. The device has potential for applications in reflective projection display technology.

Chapter 5

Design and Fabrication of Polarization-Controlled Tunable Resonant Color Filters

Achieving a static tunable color filter with high experimental efficiency and good color separation is a big challenge. We demonstrate the design and fabrication efficient GMR tunable color filters. The color output of the device is controlled by simply controlling the polarization state of the input incident light. The device is designed using numerical methods based on RCWA and is patterned using UV-laser interferometric lithography. It consists of a subwavelength silicon nitride grating along with a homogeneous silicon nitride waveguide on a glass substrate. Two color filters with grating periods of 300 nm and 370 nm have been designed and fabricated from which we can effectively get six output colors by changing the polarization. The device with grating period 300 nm exhibits green color for TE polarization and blue color for TM polarization. The device with grating period 370 nm exhibits red color for TE polarization and yellow color for TM polarization. The pixels have a spectral bandwidth of ~12 nm with efficiencies of more than 90% for TE polarization and 80% for TM polarization. The devices will find application in display and imaging technologies.

5.1 Introduction

Color filters are key elements for display devices like televisions, computers, mobile phones, digital cameras, e-readers, and multimedia projectors. They can be transmissive or reflective depending on the display technology. Dye-based transmissive color filters, that are very common in liquid crystal display (LCD) devices [67], are limited by their low efficiency, heating and wastage of light due to absorption, as well as by imperfect color selectivity. To overcome those limitations, grating-based color filters

[70−78] are of increasing research interests on account of possible high efficiency and improved band selection. Feasible grating materials include semiconductors (silicon) [70, 71], metals (aluminum) [72–75], dielectrics (nitride/oxide) [76, 77], or polymers [78]. Among those materials silicon- and aluminum-based transmissive color filters suffer from low efficiency [70−75] due to high absorption in the visible spectral region. On the other hand, dielectric reflective filters [48-49, 76] can have high efficiency with reasonably narrow bandwidths ensuring better input light utilization and color purity.

Display devices can be transmissive, reflective, or transflective. Transmissive displays use an internal light source whereas reflective displays use the ambient light; transflective displays use both internal and external light sources. Reflective displays may be based on grating light-valves [79], digital micro-mirror devices [80], and interferometric modulators [81]. In reflective displays, the color filters must be highly efficient to reflect most of the light. Dielectric GMR reflective filters can have high efficiency with reasonably narrow bandwidth [5]. Recently, we reported resonant reflective angle-tuned color filters and color filter array with high experimental efficiency and narrow bandwidth [48,49]. Prior to that, Wang et al. [77] provided computed results of reflective color filters using photoresist based on the GMR principle; Kanamori et al. [78] reported polymer-based reflective color filters with experimental efficiency of 50%; Cho et al. [82] reported reflective filters with efficiencies 30%, 75%, and 85% for the blue, green, and red colors, respectively. A plasmonic polarization-dependent color filter using metallic nanoantenna is reported in [83]. The authors demonstrated a blue to yellow color shift with the change of polarization from TM to TE.

In this study, we report the design results and fabrication of a GMR-based polarization controlled tunable color filter using subwavelength silicon nitride (Si_3N_4) gratings on a glass substrate. We design and optimize the filter parameters using

numerical methods based on RCWA [25]. We fabricate the filters using laser interferometric lithography for patterning and reactive-ion etching for pattern transfer. We report two pixels, one of which switches between red and yellow while the other switches between green and blue depending on the polarization state of the input light. We report efficiency exceeding 90% for TE polarized light and near 80% for TM polarized light at the center wavelength the respective filters. The color filters developed in this research show static tunable response accompanied by high experimental efficiency and color purity. Dielectric reflective polarization-controlled tunable color filters with comparable experimental efficiency have not been reported previously. The tunable filters have potential applications in display and imaging technology.

5.2 Theory and Design

The polarization controlled tunable color filter under consideration consists of a subwavelength silicon nitride grating along with a silicon nitride homogeneous waveguide layer on a glass substrate. The device layers and parameters are shown in Figure 5-1, where d_g denotes grating depth, d_h homogeneous layer thickness, F fill factor, Λ period, I incident light wave, T_0 zero-order transmittance, and R_0 zero-order reflectance. A GMR takes place when diffracted light from the grating structure couples with a leaky waveguide mode satisfying the phase-matching condition; a sharp resonance peak with 100% reflectance is observed at a particular wavelength. The operation details of GMR filters are explained in [20, 21].

For color filter applications, we aim to have one resonance at a particular color in the visible wavelength range. This is possible when the device is in the zero-order regime in the visible spectrum. Thus, we set the grating period to be significantly smaller than the wavelengths in the visible range, which allows the device to work in the zero-order

diffraction regime. The dimensions of the gratings such as grating-groove widths and periods are optimized to achieve particular resonance wavelength with lower sidebands for the unwanted part of the spectrum. The position of the resonance wavelength can be tuned by changing the structural and material properties of the device such as refractive index, period, thickness, and incident angle as discussed in [20, 21]. The resonance wavelength also depends on the polarization of the input light [20, 21]. In this study, we control the resonance wavelength (output color) by controlling the input light polarization. In this sense, the device works as an active filter.

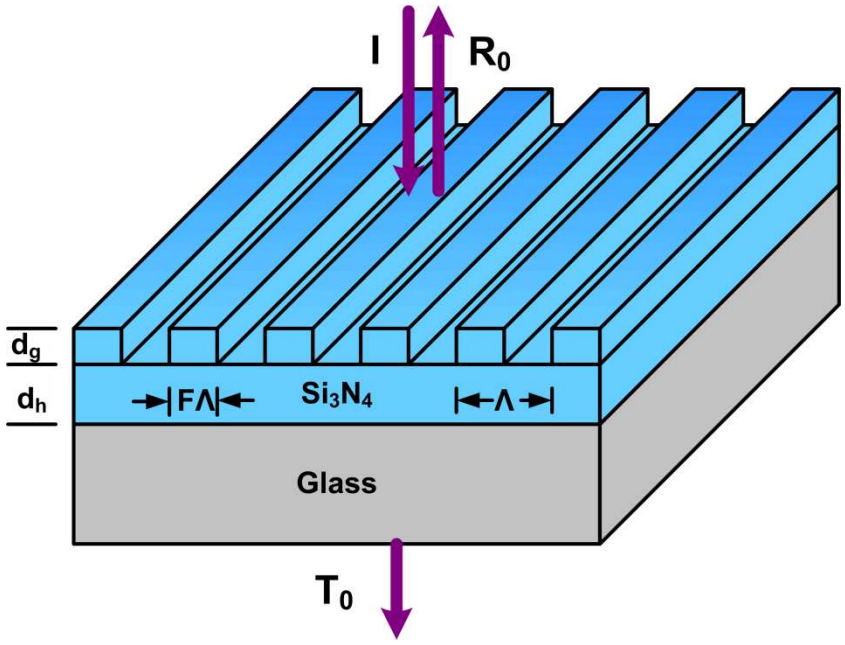

Figure 5-1 Basic GMR color filter structure showing the materials and device parameters. d_g = grating depth, d_h = thickness of homogeneous layer, F = fill factor, Λ = period, I = incident light wave, T_0 = zero-order transmittance, and R_0 = zero-order reflectance.

We design the device using numerical methods based on RCWA [13,15]. To achieve optimal reflectance, we adjust the device parameters including period, grating depth, and waveguide thickness. The optimized design parameters for our pixels are

determined to be d_g = 55 nm, d_h = 110 nm, and F = 0.5. The optimized periods of the device are 300 nm for the green-blue tunable color filter, and 370 nm for red-yellow tunable color filter.

We change the polarization state of the input incident light to get different colors from the same physical filter. The device possesses a symmetric grating profile exhibiting a single resonance under normal incidence for TE or TM polarization state. But when the polarization angle is changed, we have the superposition of the TE and TM polarization and both resonance peaks remain active based on the following relation.

$$R(\varphi,\lambda) = R_{TM}(\lambda)\cos^2\varphi + R_{TE}(\lambda)\sin^2\varphi \tag{5.1}$$

where $R_{TM}(\lambda)$ = reflectance of the TM polarized light

$R_{TE}(\lambda)$ = reflectance of the TE polarized light

φ = Polarization angle; φ = 0° $\rightarrow$TM polarization, φ = 90° $\rightarrow$ TE polarization

The reflectance for resonance peak wavelengths can be given as,

$$\begin{aligned} R(\lambda_{TM}) &= \cos^2\varphi \\ R(\lambda_{TE}) &= \sin^2\varphi \end{aligned} \tag{5.2}$$

λ_{TM} = the resonance wavelength for TM polarized light, and

λ_{TE} = the resonance wavelength for TE polarized light.

Figure 5-2 shows the computed spectral response for the green-blue polarization tunable filter. For φ = 0°, the incident light is TM polarized and for φ = 90°, the incident light is TE polarized. For TE polarized light the output color is green at a wavelength of 520 nm and for TM polarized light, the output color is blue at a wavelength of 480 nm. At φ = 45°, we get 50% green and 50% blue that will gen erate a cyan output color.

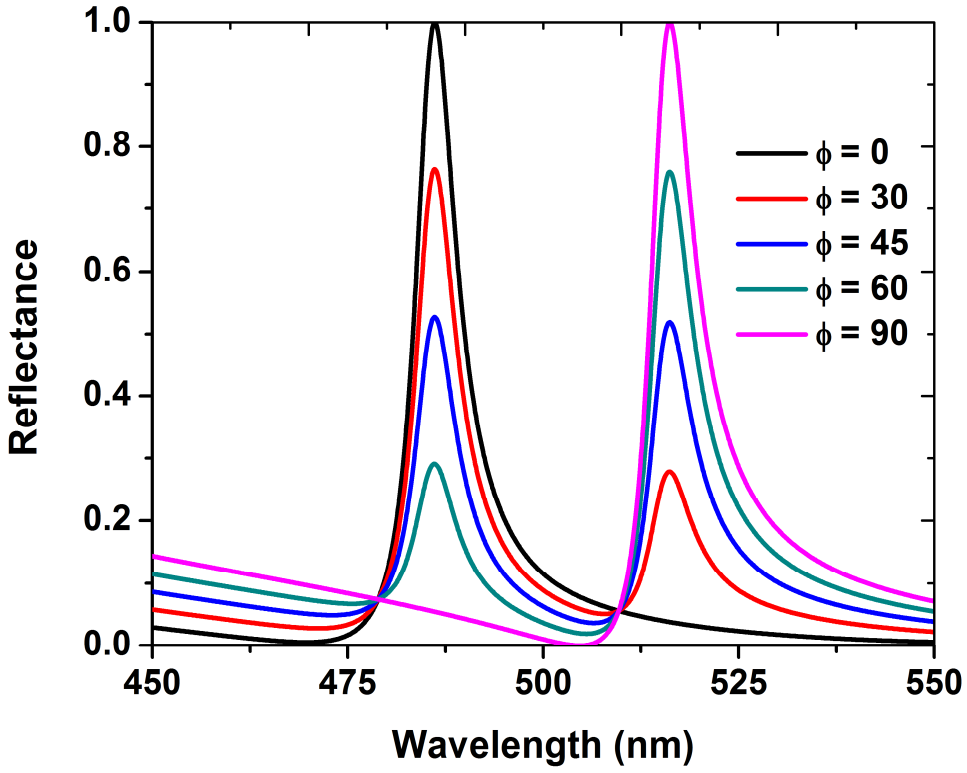

Figure 5-2 Computed spectral response of the green-blue polarization controlled tunable color filter. At φ = 0°, TM polarized incident light results in a blu e color. At φ = 90°, incident TE polarized light yields a green color. At any intermediate linear polarization, the power is distributed among TE and TM polarization components. Design parameters are d_g = 55 nm, d_h = 110 nm, F = 0.5, and Λ = 300 nm.

Figure 5-3 shows the computed spectral response for a red-yellow polarization tunable color filter. For φ = 0°, the incident light is TE polarized, and the output color is red centered at 620 nm. For φ = 90°, the incident light is TM polarized, and the output color is yellow centered at 570 nm. At φ = 45°, we get 50% red and 50% yellow color that will generate an output orange color.

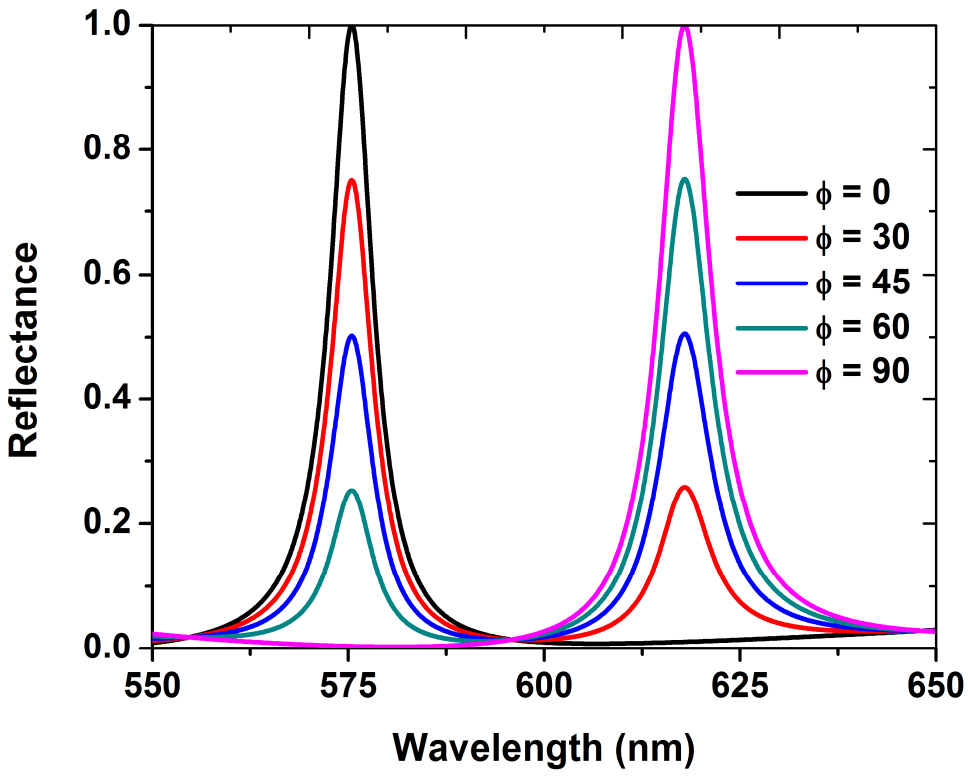

Figure 5-3 Computed spectral response of the red-yellow polarization controlled tunable color filter. At $\varphi = 0°$, TM incident polarized light creates a yellow color. At $\varphi = 90°$, incident TE polarized light results in a red color. At any intermediate linear polarization, the power is distributed among TE and TM polarization components. Design parameters are $d_g = 55$ nm, $d_h = 110$ nm, F = 0.5, and $\Lambda = 370$ nm.

Figure 5-4 shows the reflectance map of the green-blue tunable color filter for the whole polarization range of 0 to 360°. We can see the symmetric nature at the polarization angle of 180°.

Figure 5-5 shows the reflectance map of the red-yellow polarization tunable color for the change of polarization from 0 to 360°.

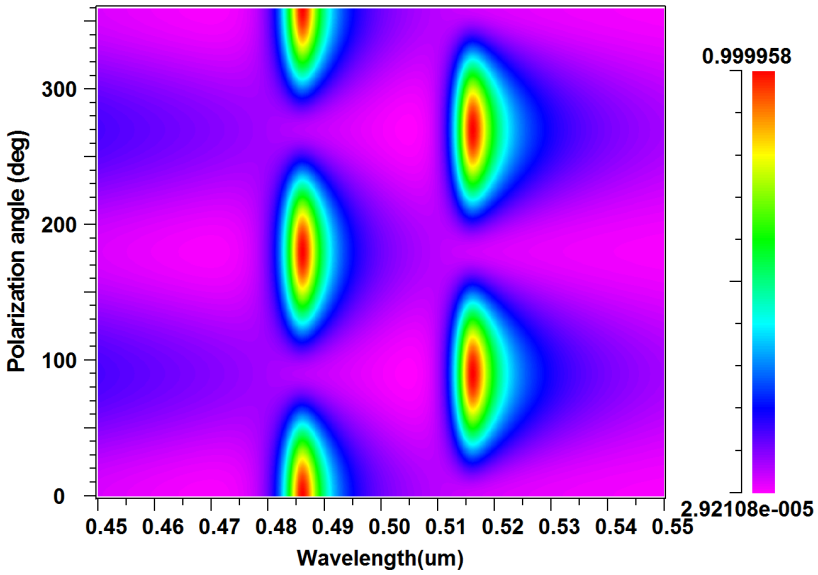

Figure 5-4 Reflectance map of a green-blue polarization-tunable pixel for a polarization angle sweep of 360 degrees. The map is symmetric around the angle of 180°.

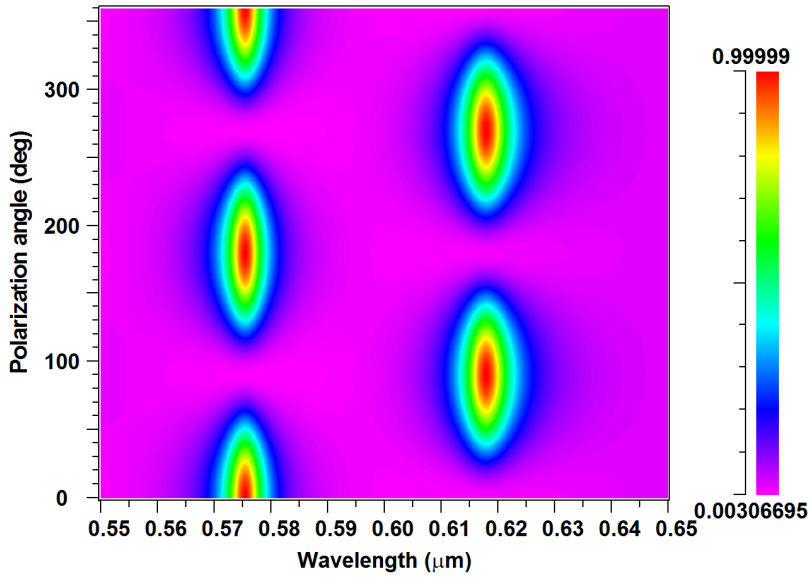

Figure 5-5 Reflectance map of a red-yellow polarization-tunable filter for a polarization angle sweep of 360°. The map is symmetric around th e angle of 180°.

Using the reflectance of the color filters, the displayable red, green, and blue primary colors can be calculated using standard equations as provided in [84]. The first step is to calculate the Commission Internationale de l'Eclairage (CIE) XYZ tristimulus values of a color as expressed by,

$$X = p\int_{\lambda} D(\lambda)R(\lambda)\bar{x}(\lambda)d\lambda$$
$$Y = p\int_{\lambda} D(\lambda)R(\lambda)\bar{y}(\lambda)d\lambda \quad (5.3)$$
$$Z = p\int_{\lambda} D(\lambda)R(\lambda)\bar{z}(\lambda)d\lambda$$

Here $\bar{x}$, $\bar{y}$, and $\bar{z}$ are CIE 1931 standard observer color-matching functions, D(λ) is the energy distribution of the illuminant, and we use CIE normalized illuminant D65 that closely matches the characteristics of daylight. For convenience we use a fourth-order polynomial approximation of this function; p is the normalizing coefficient that can be obtained using Eq. (5.4), which is defined in such a way that an object with a uniform unity reflectance will have the Y component of the tristimulus value equal to unity.

$$1/p = \int_{\lambda} D(\lambda)\bar{y}(\lambda)d\lambda \quad (5.4)$$

Then, a linear matrix multiplication is performed using Eq. (5.3) to calculate the intermediate linear RGB colors. The numerical values used for the conversion matrix match those specified in the IEC 61966-2-1: 1999 standard.

$$\begin{bmatrix} R_{linear} \\ G_{linear} \\ B_{linear} \end{bmatrix} = \begin{bmatrix} 3.2406 & -1.5372 & -0.4986 \\ -0.9689 & 1.8758 & -0.0415 \\ 0.0557 & -0.2040 & 1.0570 \end{bmatrix} \begin{bmatrix} X \\ Y \\ Z \end{bmatrix} \quad (5.5)$$

Thereafter, using Eq. (5.4) below, these linear RGB values are converted into standard RGB components (sRGB). In Eq. (5.4), a = 0.055, C_{srgb} represents R_{srgb}, G_{srgb}, or B_{srgb}, and C_{linear} represents R_{linear}, G_{linear}, or B_{linear}. Finally, the values of C_{srgb} are

changed to the 8-bit range of 0 to 255 by multiplying it with 255 and rounding off to the closest integer. The perceived color then can be constructed from the integer C_{srgb} values.

$$C_{srgb} = \begin{cases} 12.92C_{linear} & C_{linear} \le 0.0031308 \\ (1+a)C_{linear}^{1/2.4} - a & C_{linear} > 0.0031308 \end{cases} \quad (5.6)$$

5.3 Device Fabrication and Characterization

To fabricate the proposed color filters, we first deposit Si_3N_4 thin-film using a sputtering system on a cleaned microscopic glass substrate. Thereafter, we spin-coat a 300-nm-thick positive photoresist (PR) on Si_3N_4.To increase the adhesion between PR and Si_3N_4 , we spin coat a very thin layer of hexamethyldisiloxane (HMDS) on Si_3N_4 film before applying the PR. HMDS crosslinks PR with Si_3N_4 and increases the adhesion. Then we record a 1D grating pattern on the PR using a laser interferometric lithography system. Our laser interferometric lithography system is based on a classic Lloyd-mirror geometry with a pattern period conveniently controlled by a simple stage rotation. The exposing laser has a 266-nm wavelength; it is well polarized and provides up to 200 mW output power in a very narrow spectral band. To etch the nitride film, we use reactive ion etching (RIE) involving a gas mixture of trifluromethane (CHF_3) and oxygen (O_2). After RIE, a thin PR film still exists on the nitride grating and it is stripped using O_2 plasma. Finally, we use wet cleaning with nanostrip (90% H_2SO_4 and 5% H_2O_2) followed by O_2 plasma ashing to ensure that no PR remains on the nitride grating. Figure 5-6 shows a clear summary of the steps used to fabricate the color filter.

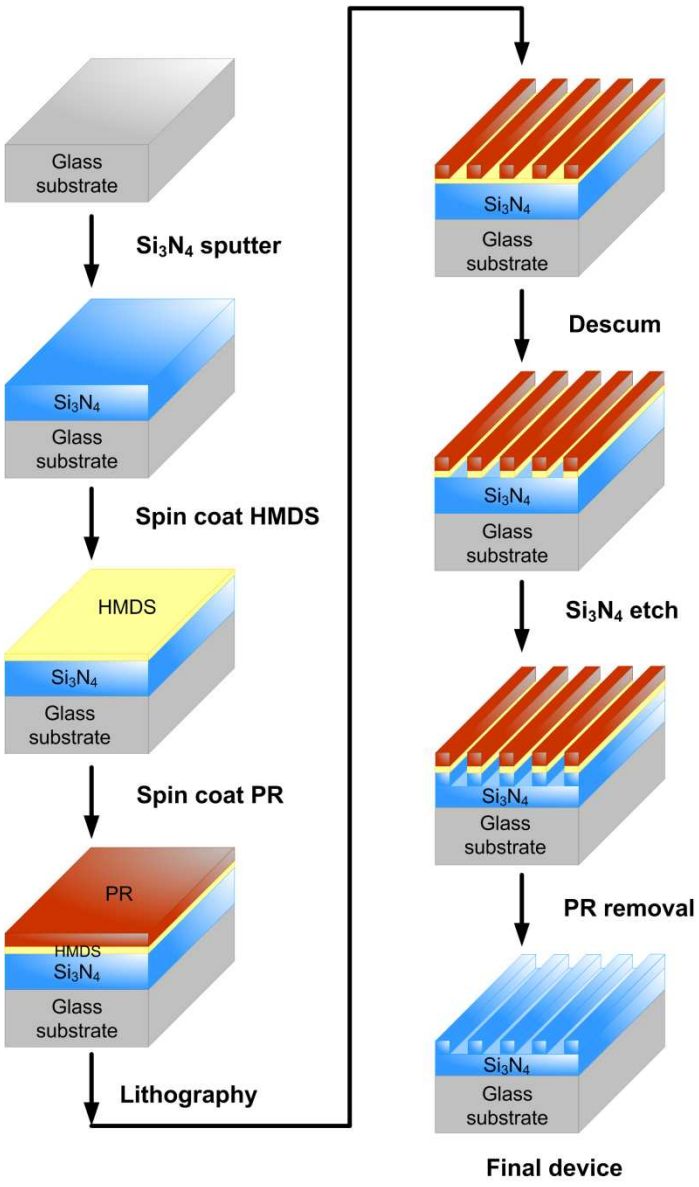

Figure 5-6 Summary of the fabrication steps applied to realize the color filters under study.

We characterize the devices using an atomic force microscope (AFM). From the AFM image, we verify the period, grating thickness, and fill factor. We find the homogeneous waveguide thickness by subtracting the grating thickness from the film

thickness, which is measured by ellipsometry. The AFM image in Figure 5-7 shows the grating profile of the green-blue polarization-controlled tunable pixel. From the AFM image, the fabricated device parameters are $d_g \approx 54$ nm, $\Lambda \approx 301$ nm, and $F \approx 0.5$. The ellipsometrically measured parameters for the nitride film used for green-blue tunable filter are d = 160 nm, n = 2.05, and $k = 2\times 10^{-4}$ at wavelength of 550 nm where d is the film thickness, n is the refractive index and k is the extinction coefficient. From the AFM data and ellipsometry measurement, we get the homogeneous layer thickness as $d_h \approx$ 106 nm. Figure 5-8 shows the grating profile of the red-yellow tunable filter; the fabricated device parameters are $d_g \approx 60.5$ nm, $\Lambda \approx 369$ nm, and $F \approx 0.46$. The ellipsometric parameters for the nitride film used for the red-yellow tunable filter are d = 165 nm, n = 2.02 and $k = 2\times 10^{-4}$ at wavelength of 550 nm. From the AFM results and ellipsometry data the homogenous waveguide thickness is $d_h \approx 104.5$ nm.

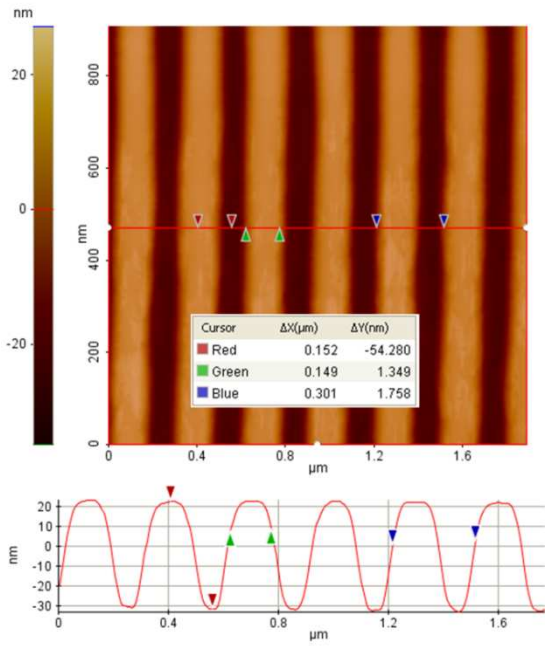

Figure 5-7 AFM image showing the grating profile of the green-blue PCTCF. Device parameters are: $d_g \approx 54$ nm, $d_h \approx 106$ nm, $\Lambda \approx 301$ nm, and $F \approx 0.5$.

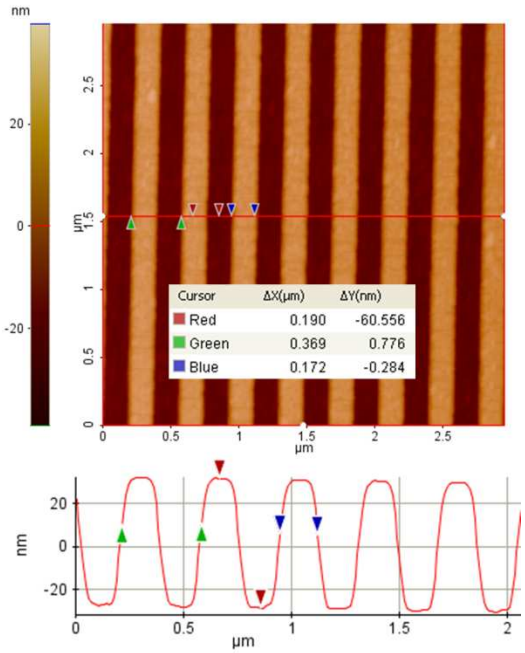

Figure 5-8 AFM image showing the grating profile of the red-yellow PCTCF pixel. Device parameters are $d_g \approx 60$ nm, $d_h \approx 105$ nm, $\Lambda \approx 369$ nm, and $F \approx 0.46$.

The fabricated devices parameters found from AFM and ellipsometry measurement are close to the design parameters. The fabricated pixels presented here are considerably large (5×5 mm^2) for convenience in characterization and spectral measurements. But to apply this technology in devices, the pixel size should be finite and smaller in dimension. The effective pixel size can be calculated using the decay length of the leaky waveguide mode. The decay length is approximately $L_d \approx \Lambda\lambda/4\pi\Delta\lambda$, where $\Delta\lambda$ is the spectral linewidth of the color filter [18]. Using this equation, we estimate the decay length as ~2 μm. Thus, this pixel should work well with, for example, 10×10 μm^2 lateral dimensions, which significantly exceed this decay limit. Fabricated device dimensions can be reduced subsequently to ~10-μm scale devices using, for example, smaller apertures in the laser interferometric lithography system.

5.4 Results and Discussion

The reflectance as a function of wavelength of the fabricated color filters is measured using a spectrum analyzer. A tungsten halogen lamp with a wavelength range of 360–1100 nm serves as the light source. A polarizer is mounted in front of the light source to select a specific polarization state. We can change the polarization from 0 to 360 degrees using our measurement setup. But looking at the reflectance for 0 to 90 degrees will give us the picture for whole polarization range; we only measured for this range of polarization angles. 0° polarization angle means that the electric field is in parallel with the plane of incidence, which is known as TM polarized light. 90° polarization angle means the electric field is in orthogonal direction with the plane of incidence resulting a TE polarized light. At first, we measure the reflected light intensity as a function of wavelength from a reference mirror. Then, we measure the reflected light intensity from the color filter. Finally, we calculate the reflectance of the color filter by taking the ratio of reflected intensity from the sample to the reflected intensity from the reference mirror for each wavelength.

Figure 5-9 shows the experimental and theoretical reflectance of the fabricated blue-green tunable filter. For $\varphi = 0°$, the output color is blue and the center wave length is 480 nm for both theory and experiment. For $\varphi = 90°$, the output color is green with the center wavelength 518 nm for experiment and 525 nm for theory. The measured FWHM or spectral width is 14 nm for TE polarized light and 12 nm for TM polarized light. The theoretical spectral width is 12 nm for TE and 10 nm for TM polarized light. The simulated reflectance is calculated using the device parameters found by AFM and ellipsometry. The fabricated device parameters are $\Lambda = 301$ nm, $d_g = 54$ nm, $F = 0.5$, $d_h = 106$ nm, and $n = 2.05$ and these same parameters are used for simulation.

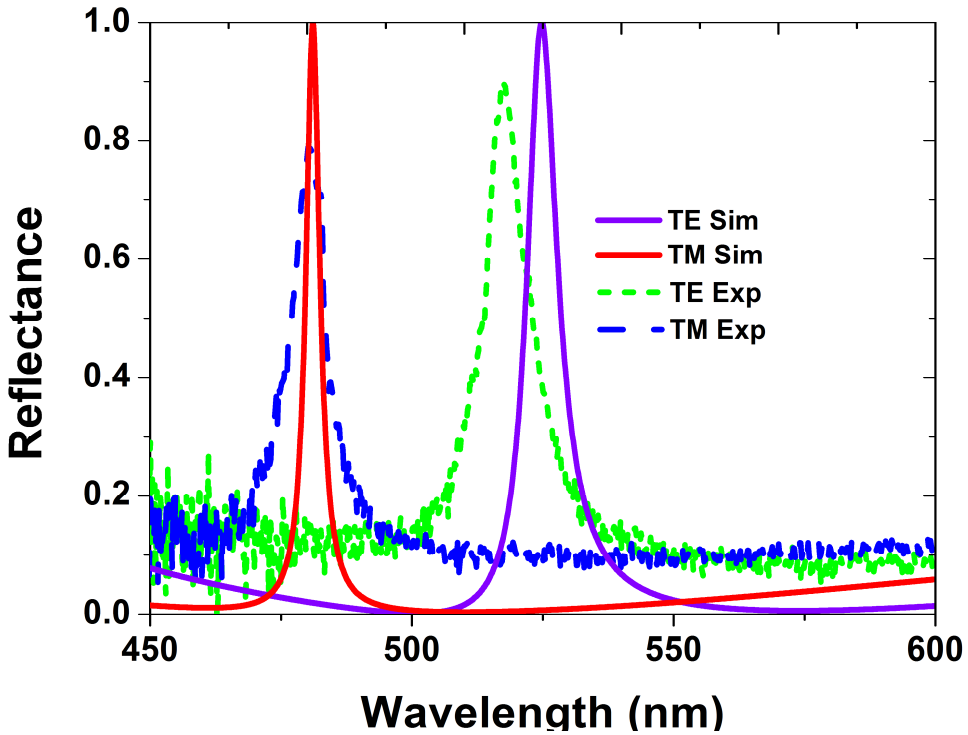

Figure 5-9 Spectral response of the green-blue polarization-tunable color filter. Blue filter: λ_c = 480 nm for theory and experiment, R_0 = 80 % (experiment) green filter: λ_c = 518 nm (experiment) and 525 nm (theory) R_0 = 90% (experiment). Theoretical R_0 for both blue and green filter is 100%; λ_c = center wavelength of a pixel, where the efficiency is maximum.

Figure 5-10 compares the experimental and simulated reflectance of the fabricated red-yellow tunable pixel. For φ = 0°, the output color is yellow and the center wavelength is 570 nm for both theory and experiment. For φ = 90°, the output color is red with the center wavelength 620 nm for experiment and 625 nm for theory. The measured full width at half maximum, or spectral width, is ~ 14 nm for TE polarized light and 12 nm for TM polarized light. The theoretical spectral width is 12 nm for TE and 10 nm for TM

polarized light. The simulated reflectance is calculated using the device parameters found by AFM and ellipsometric measurements. The fabricated device parameters are Λ = 369.5 nm, d_g = 60.5 nm, F = 0.46, d_h = 104.5, and n = 2.02 nm and these same parameters are used for simulation. The resonance shift between the theory and experimental results is due to the inaccuracy in the AFM measured data.

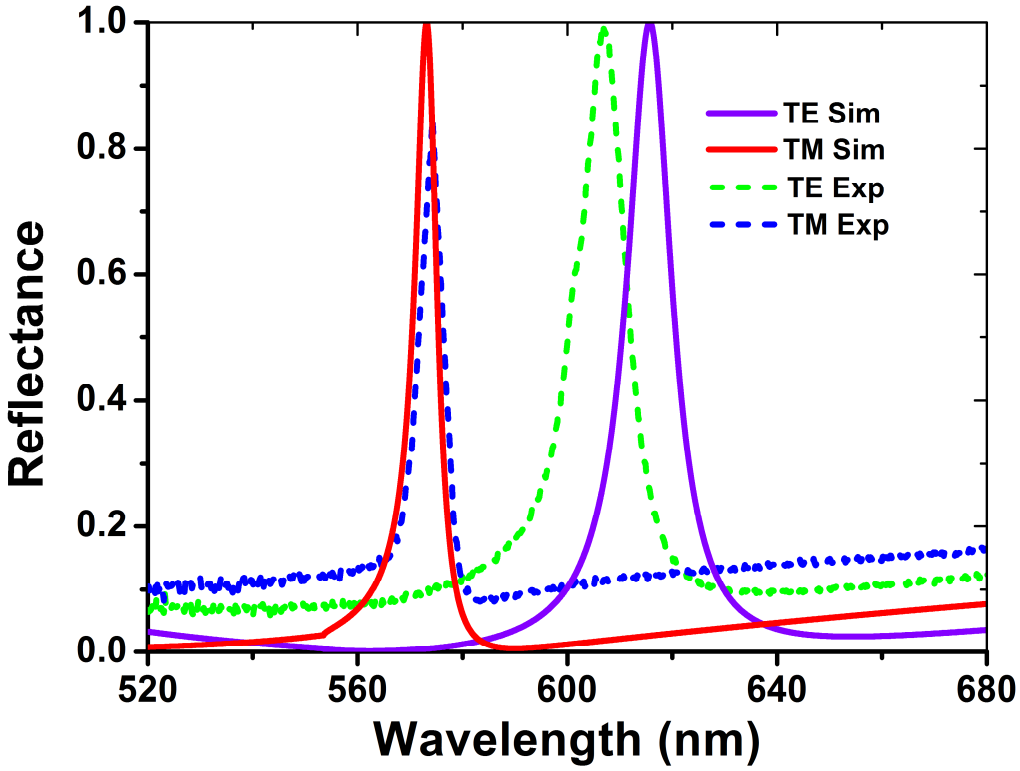

Figure 5-10 Spectral response of the red-yellow polarization tunable color filter. Yellow filter: λ_c = 570 nm for theory and experiment, R_0 = 82%(experiment) red filter: λ_c = 620 nm (experiment) and 625 nm(theory) R_0 = 98% (experiment). Theoretical R_0 for both red and yellow filter is 100% ; λ_c = center wavelength of a pixel, where the efficiency is maximum.

Figure 5-11 shows the CIE chromaticity diagram displaying the color gamut of the polarization controlled tunable color filter. Due to the availability of four RGYB colors from two pixels, it shows a quadrilateral color gamut instead of the conventional triangular color gamut from RGB pixel. The coordinates of RGYB colors in the chromaticity diagram are calculated from the calculated CIE tri-stimulus values (XYZ) from equation (5.3) by using the following equation,

$$x = \frac{X}{X+Y+Z}$$
$$y = \frac{Y}{X+Y+Z} \qquad (5.7)$$

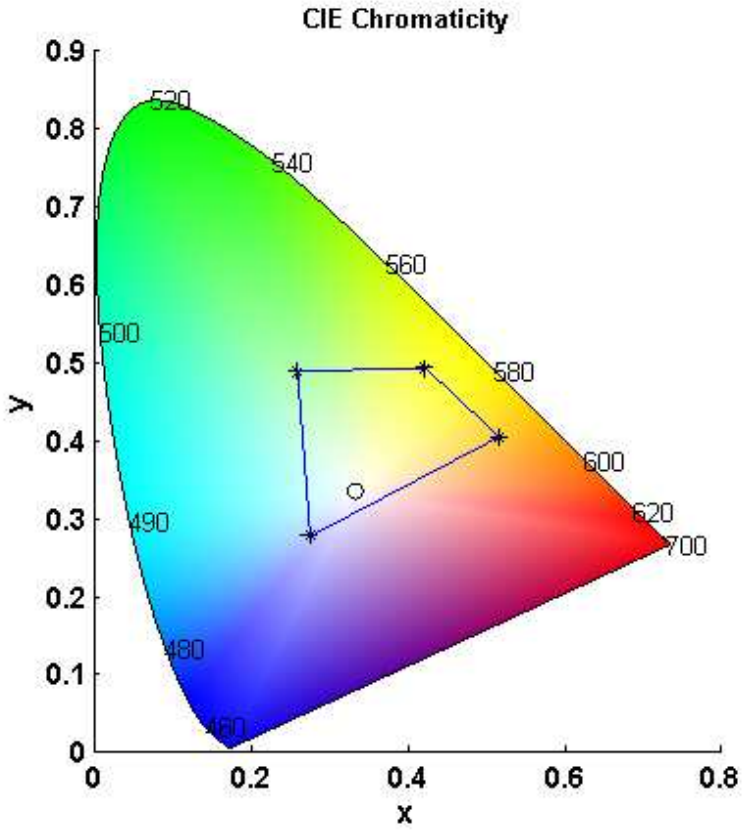

Figure 5-11CIE chromaticity diagram showing the color gamut of the prototype tunable color filters.

From the experimental reflectance values, standard RGB components (sRGB) values are calculated using Eqs. (5.1) − (5.4). The sRGB values are 105, 107, and 133 for the blue pixels; 0, 145, and 85 for the green pixels; 162, 85, and 27 for the red pixels and 128, 123, and 27 for yellow filter. Figure 5-12 shows the perceived colors using the sRGB values of the pixels found from the experimentally observed reflectance values of the pixels.

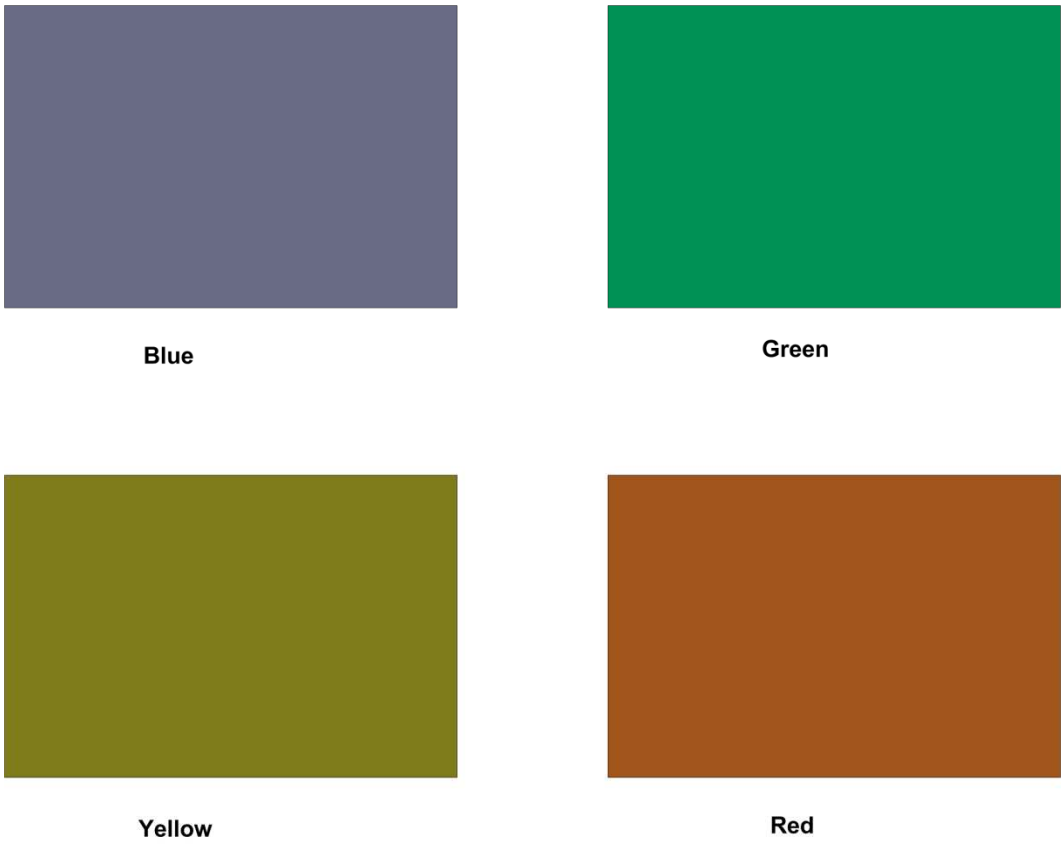

Figure 5-12 Perceived colors constructed from the experimentally observed reflectance values.

5.5 Conclusion

An efficient GMR-based reflective tunable polarization-controlled tunable color filter is designed and fabricated using a subwavelength Si_3N_4 grating along with a homogeneous Si_3N_4 layer on a glass substrate. A red color filter with TE polarized light can produce yellow color for TM polarized light. A green filter for TE polarized light can produce blue color with TM polarized light. Therefore, the two pixels can successfully generate four colors without any intermediate mixing. The fabricated filters possess high experimental efficiency with narrow bandwidth. We find a reasonably good match between the experimental data and theoretical simulation results. The device has potential for applications in displays, image sensors and biomedical imaging.

Chapter 6

Highly Efficient Color Filter Array Using Resonant Si_3N_4 Gratings

We demonstrate the design and fabrication of a highly efficient guided-mode resonant color filter array. The device is designed using numerical methods based on RCWA and is patterned using UV-laser interferometric lithography. It consists of a 60-nm-thick subwavelength silicon nitride grating along with a 105-nm-thick homogeneous silicon nitride waveguide on a glass substrate. The fabricated device exhibits blue, green, and red color response for grating periods of 274, 327, and 369 nm, respectively. The pixels have a spectral bandwidth of ~12 nm with efficiencies of 94%, 96%, and 99% at the center wavelength of blue, green, and red color filter, respectively. These are higher efficiencies than reported in the literature previously.

6.1 Introduction

Electronic devices such as televisions, computers, mobile phones, digital cameras, e-readers, and multimedia projectors contain various color filters for image display. The liquid crystal display (LCD) is a dominant technology primarily using dye-based color filters, which transmit a particular color under white light illumination [67]. Limitations include low efficiency, heating due to light absorption, and imperfect color selectivity. The class of grating-based color filters [70−78] is an interesting alternative, potentially overcoming these limitations on account of high efficiency and improved band selection. Feasible grating materials include semiconductors (silicon) [70,71], metals (aluminum) [72–75], dielectrics (nitride/oxide) [76,77], or polymers [78].

Displays can be transmissive, reflective, or transflective. In transmissive displays, an internal light source is required whereas reflective displays can work with ambient light; transflective displays use both internal and external light sources to augment low

ambient light levels. Transmissive displays often apply silicon and aluminum with attendant low efficiency [70−75] due to high absorption in the visible spectrum region. Well-known transmissive displays are LCD televisions and computer monitors. Reflective display technologies may be based on grating light-valves [79], digital micro-mirror devices [80], and interferometric modulators [81]. These displays use micro-electro-mechanical systems-based control of the pixels. In reflective displays under ambient light, the color filters must be highly efficient to reflect most of the light. We define efficiency as the ratio of the intensity of the reflected output light to the intensity of the input light at a particular wavelength, which is also known as reflectance. Dielectric guided-mode resonance (GMR) reflective filters can have high efficiency with reasonably narrow bandwidth [20, 21], favorably impacting input light utilization and color purity. Recently, we reported an angle-tuned highly efficient color filter [48] for projection display applications. Prior to that, Wang et al. [77] provided computed results of a reflection-type color filter array using photoresist material based on the GMR principle; Kanamori et al. [78] reported a polymer-based reflection color filter array (CFA) with experimental efficiency of 50%. Cho et al. [82] reported an a-Si-based reflection CFA with experimental efficiency of 30% for the blue, 75% for the green, and 85% for the red color filter.

In this study, we report the design results and fabrication of a GMR-based CFA using subwavelength silicon nitride (Si_3N_4) gratings on a glass substrate. We design and optimize the filter parameters using numerical methods based on RCWA [13,15]. We fabricate the filters using laser interferometric lithography for patterning. We realize three pixels on the same substrate with differing periods and attendant resonance wavelengths. We report efficiency exceeding 94% at the center wavelength of the fabricated blue, green, and red color filters. A dielectric reflective CFA with comparable experimental efficiency has not been reported previously. The color filters developed in

this research show improved input light utilization due to higher efficiency and higher color purity due to narrower bandwidth. The CFA can be incorporated with existing reflective LCD display technology to produce colored displays. It may also find use in reflective projection display technology.

6.2 Theory and Design

The color filter array under consideration consists of a subwavelength silicon nitride grating along with a silicon nitride homogeneous waveguide layer on a glass substrate. The device layers and parameters are shown in Figure 6-1, where d_g denotes grating depth, d_h homogeneous waveguide thickness, F fill factor, Λ period, I incident light wave, T_0 zero-order transmittance, and R_0 zero-order reflectance. A GMR takes place when diffracted light from the grating structure couples with a leaky waveguide mode satisfying the phase-matching condition; a resulting sharp resonance peak with 100% reflectance is observed at a particular wavelength. GMR filter operation details are explained in [20, 21]. We set the grating period to be significantly smaller than the wavelengths in the visible range, which allows the device to work in the zero-order diffraction regime. The dimensions of the gratings such as grating grooves and periods are optimized to achieve particular (RGB) resonance wavelengths and attendant lower sidebands for the unwanted part of the spectrum. The position of the resonance wavelength can be tuned by changing the refractive index, period, thickness, and incident angle as discussed in [20, 21].

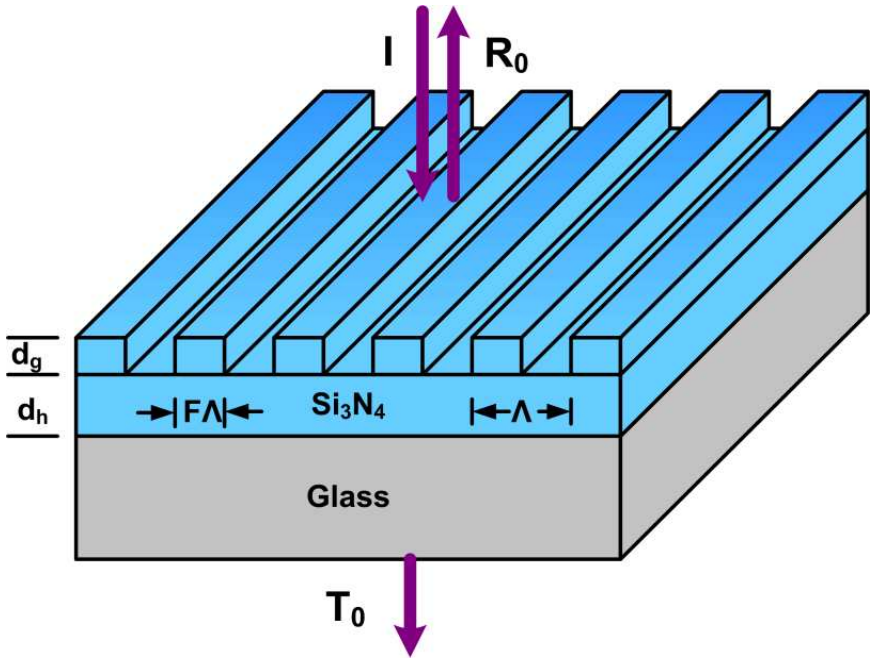

Figure 6-1 Basic GMR color filter structure showing the materials and device parameters. d_g = grating depth, d_h = thickness of homogeneous layer, F = fill factor, Λ = period, I = incident light wave, T_0 = zero-order transmittance, and R_0 = zero-order reflectance.

In this study, we use different grating periods of the GMR filter, keeping other device parameters constant to obtain three primary colors. The device possesses a symmetric grating profile exhibiting a single resonance under normal incidence. We design the device using numerical methods based on RCWA. To achieve optimal reflectance, we adjust the device parameters including period, grating depth, and waveguide thickness. The optimized design parameters for all pixels are d_g = 55 nm, d_h = 110 nm, and F = 0.5. The optimized periods of the device are 275 nm for the blue, 325 nm for the green, and 375 nm for the red color. Computed reflectance of the designed CFA for the normally incident transverse-electric (TE) polarized light is given in Figure 6-2. The center wavelengths for blue, green, and red pixels are 484 nm, 555 nm, and 626

nm, respectively, with FWHM of ≈ 10 nm. We use the wavelength-dependent dispersive optical constants of Si_3N_4 as shown in Figure 6-3 for the design of the filters.

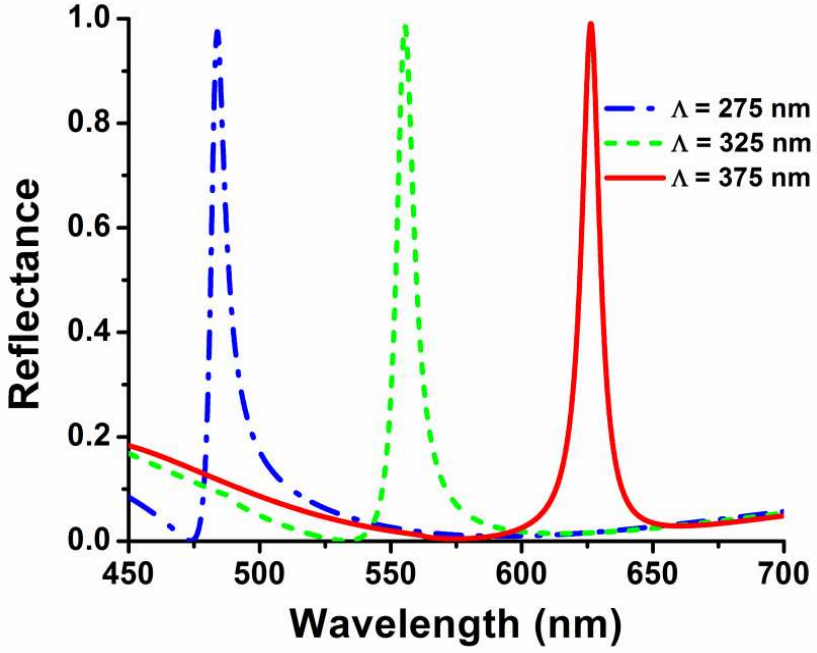

Figure 6-2 Reflectance of the designed color filter array for normally incident TE polarized light. Design parameters are d_g = 55 nm, d_h = 110 nm, and F = 0.5; Λ is 275 nm for blue, 325 nm for green, and 375 nm for red color. TE polarized light has an electric field vector normal to the plane of incidence and along the grating grooves in Figure 6-1.

Using the reflectance of the color filters, the displayable red, green, and blue primary colors can be calculated using standard equations as provided in [86]. The first step is to calculate the Commission Internationale de l'Eclairage (CIE) XYZ tristimulus values of a color as expressed by,

$$X = p\int_{\lambda} D(\lambda)R(\lambda)\bar{x}(\lambda)d\lambda$$
$$Y = p\int_{\lambda} D(\lambda)R(\lambda)\bar{y}(\lambda)d\lambda \quad (6.1)$$
$$Z = p\int_{\lambda} D(\lambda)R(\lambda)\bar{z}(\lambda)d\lambda$$

Here $\bar{x}$, $\bar{y}$, and $\bar{z}$ are CIE 1931 standard observer color-matching functions, D(λ) is the energy distribution of the illuminant, and we use CIE normalized illuminant D65 that closely matches the characteristics of daylight. For convenience we use a fourth-order polynomial approximation of this function; p is the normalizing coefficient that can be obtained using Eq. (6.2), which is defined in such a way that an object with a uniform unity reflectance will have the Y component of the tristimulus value equal to unity.

$$1/p = \int_{\lambda} D(\lambda)\bar{y}(\lambda)d\lambda \quad (6.2)$$

Then, a linear matrix multiplication is performed using Eq. (6.3) to calculate the intermediate linear RGB colors. The numerical values used for the conversion matrix match those specified in the IEC 61966-2-1: 1999 standard.

$$\begin{bmatrix} R_{linear} \\ G_{linear} \\ B_{linear} \end{bmatrix} = \begin{bmatrix} 3.2406 & -1.5372 & -0.4986 \\ -0.9689 & 1.8758 & -0.0415 \\ 0.0557 & -0.2040 & 1.0570 \end{bmatrix} \begin{bmatrix} X \\ Y \\ Z \end{bmatrix} \quad (6.3)$$

Thereafter, using Eq. (6.4) below, these linear RGB values are converted into standard RGB components (sRGB). In Eq. (6.4), a = 0.055, C_{srgb} represents R_{srgb}, G_{srgb}, or B_{srgb}, and C_{linear} represents R_{linear}, G_{linear}, or B_{linear}. Finally, the values of C_{srgb} are changed to the 8-bit range of 0 to 255 by multiplying it with 255 and rounding off to the closest integer. The perceived color then can be constructed from the integer C_{srgb} values.

$$C_{srgb} = \begin{cases} 12.92C_{linear} & C_{linear} \le 0.0031308 \\ (1+a)C_{linear}^{1/2.4} - a & C_{linear} > 0.0031308 \end{cases} \quad (6.4)$$

6.3 Device Fabrication and Characterization

Device fabrication starts with Si_3N_4 thin-film deposition on a clean microscopic glass substrate using a sputtering system. The optical constants and thickness of the film are measured using ellipsometry. The film thickness is 165 nm and the measured optical constants for the Si_3N_4 film in the visible spectral region are given in Figure 6-3.

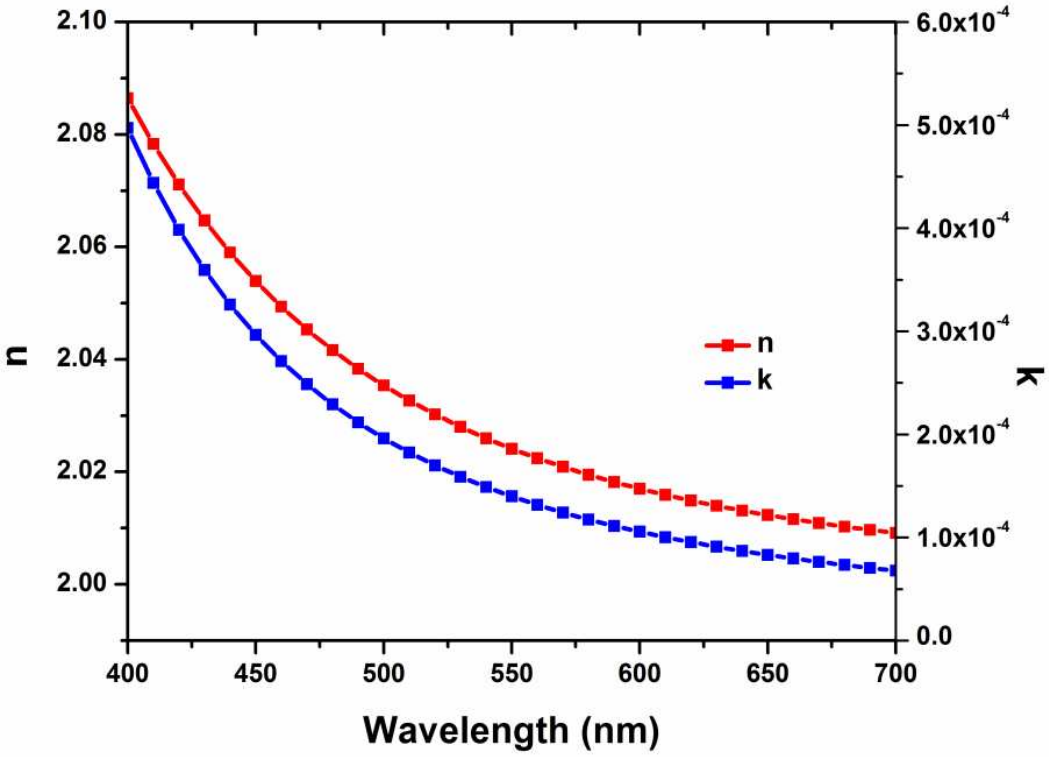

Figure 6-3 Ellipsometry measured n, k values of sputter-deposited Si_3N_4 in the visible region.

Thereafter, a 300-nm-thick positive photoresist (PR) is spin coated at 2000 rpm on Si_3N_4. The adhesion of PR with Si_3N_4 is not very strong. To increase the adhesion, a very thin hexamethyldisiloxane (HMDS) layer is spin coated at 3000 rpm on Si_3N_4 film before applying the photoresist. HMDS crosslinks PR with Si_3N_4 and increases the adhesion. The HMDS is baked at 120ºC for 120 seconds, and the PR is baked at 110ºC for 90 seconds. Then a 1D grating pattern is recorded on the PR using a laser interferometric lithography system. Our laser interferometric lithography system is based on a classic Lloyd-mirror geometry with a pattern period conveniently controlled by a simple stage rotation. The exposing laser has a 266-nm wavelength; it is well polarized and provides up to 200 mW output power in a very narrow spectral band. The exposed PR is developed for 50 seconds in AZ 917 MIF developer followed by DI water rinsing for 60 seconds. To etch the nitride film, we use reactive ion etching (RIE) involving a gas mixture of trifluromethane (CHF_3) and oxygen (O_2). We run a short 10-s descum recipe using O_2 plasma before the etching step to ensure no PR remains at the bottom of PR pattern. After RIE, a thin PR film still exists on the nitride grating and it is stripped using O_2 plasma. Finally, we use wet cleaning with nanostrip (90% H_2SO_4 and 5% H_2O_2) followed by O_2 plasma ashing to ensure that no PR remains on the nitride grating. Figure 6-4 shows a clear summary of the steps used to fabricate the CFA.

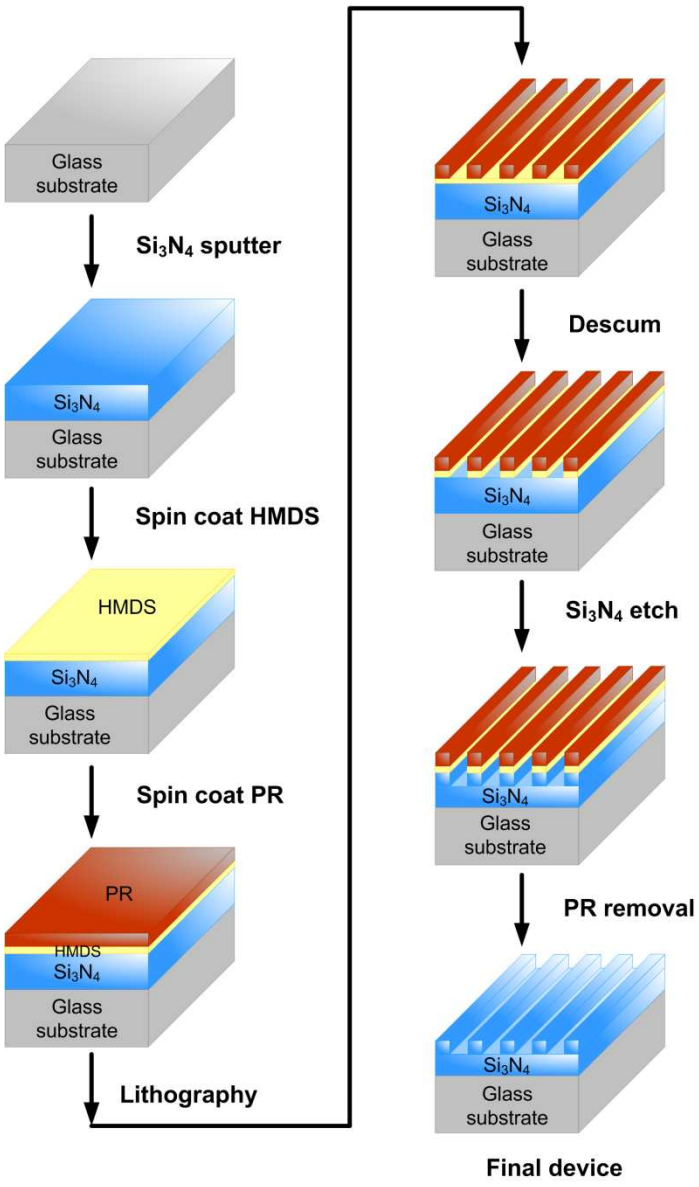

Figure 6-4 Summary of the fabrication steps of CFA.

The device is characterized using an atomic force microscope (AFM). From the AFM image, we verify the period, grating thickness, and fill factor. The waveguide thickness is calculated by subtracting the grating thickness from the film thickness, which is measured by ellipsometry. The AFM image in Figure 6-5 shows the grating profile of

the blue pixel. From the AFM image and ellipsometric data, the fabricated device parameters are $d_g \approx 58.5$ nm, $d_h \approx 106.5$ nm, $\Lambda \approx 274$ nm, and $F \approx 0.46$. Figure 6-6 shows the grating profile of the green pixel; the fabricated device parameters are $d_g \approx 59.2$ nm, $d_h \approx 105.8$ nm, $\Lambda \approx 327$ nm, and $F \approx 0.46$. Figure 6-7 shows the grating profile of the red pixel; the fabricated device parameters are:$d_g \approx 60.5$ nm, $d_h \approx 104.5$ nm, $\Lambda \approx 369$ nm, and $F \approx 0.46$. We see that for devices with larger periods, the grating depth is a bit larger than that of the lower period devices. This phenomenon is known as the macroscopic loading effect [85]. For higher periods, due to the larger opening area, a higher density of gases reacts with the material to be etched. This creates a larger grating depth for devices with larger periods even though the etch time is the same.

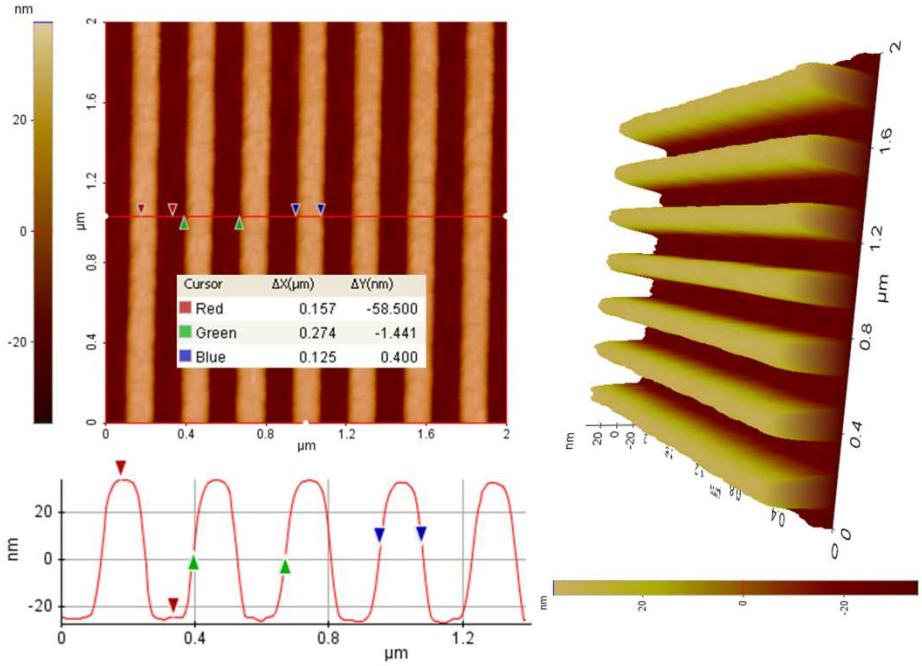

Figure 6-5 AFM image showing the grating profile of the blue pixel. Device parameters are $d_g \approx 58.5$ nm, $d_h \approx 106.5$ nm, $\Lambda \approx 274$ nm, and $F \approx 0.46$.

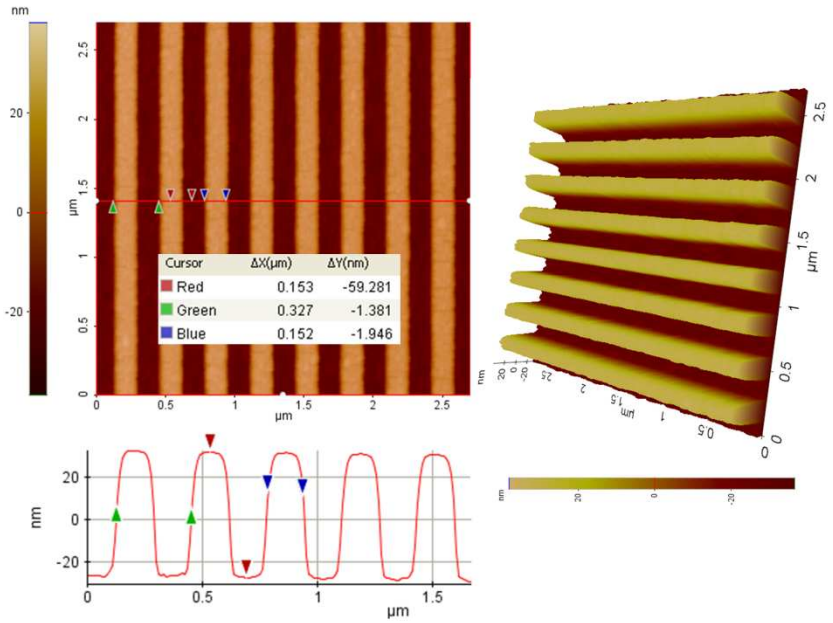

Figure 6-6 AFM image showing the grating profile of the green pixel. Device parameters are $d_g \approx 59.2$ nm, $d_h \approx 105.8$ nm, $\Lambda \approx 327$ nm, and $F \approx 0.46$.

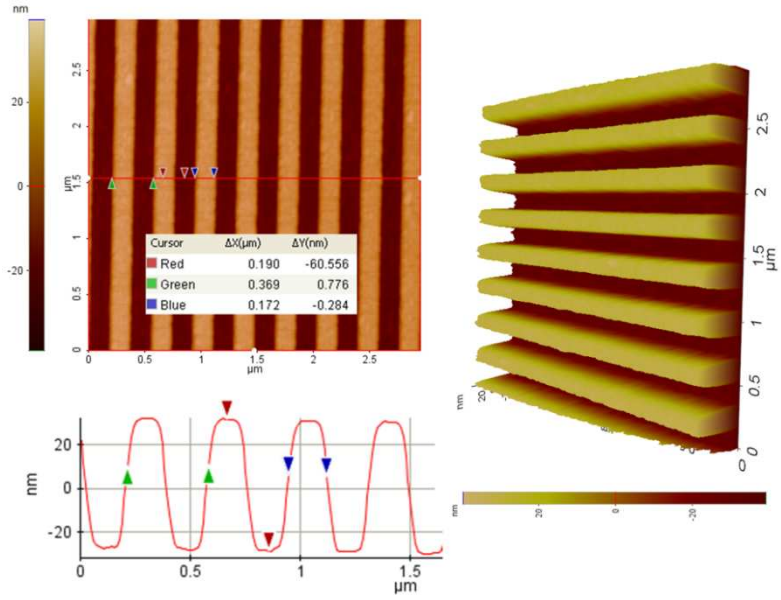

Figure 6-7 AFM image showing the grating profile of the red pixel. Device parameters are: $d_g \approx 60.5$ nm, $d_h \approx 104.5$ nm, $\Lambda \approx 369$ nm, and $F \approx 0.46$.

The fabricated devices have an approximate grating thickness of 60 nm and a waveguide thickness of 105 nm, which are close to the initial design parameters (grating thickness of 55 nm and waveguide thickness of 110 nm). The periods (274 nm, 327 nm, and 369 nm) of the fabricated pixels are also close to the initial design parameters (275 nm, 325 nm, and 375 nm).

The effective pixel size can be calculated using the decay length of the leaky waveguide mode. The decay length is approximately $L_d \approx \Lambda\lambda/4\pi\Delta\lambda$, where $\Delta\lambda$ is the spectral linewidth of the color filter [18]. Using this equation, we estimate the decay length as ~2 μm. Thus, this pixel should work well with, for example, 10×10 μm^2 lateral dimensions, which significantly exceed this decay limit. The fabricated pixels presented here are considerably larger (5×5 mm^2) for convenience in characterization and spectral measurements. Fabricated device dimensions can be reduced subsequently to ~10-μm scale devices using, for example, smaller apertures in the laser interferometric lithography system.

6.4 Results and Discussion

The reflectance or efficiency as a function of wavelength of the fabricated color filters is measured using a spectrum analyzer. A tungsten halogen lamp with a wavelength range of 360–1100 nm serves as the light source. A polarizer is mounted in front of the light source to select a specific polarization state. We use normally incident TE polarized light in which the electric field vector is normal to the plane of incidence and along the grating grooves in Figure 6-1. At first, we measure the reflected light intensity as a function of wavelength from a reference mirror. Then, we measure the reflected light intensity from the color filter. The computer stores these data in separate files. Then, we

calculate the reflectance of the color filter by taking the ratio of reflected intensity from the sample to the reflected intensity from the reference mirror for each wavelength.

Figure 6-8 shows the reflectance of the fabricated blue, green, and red pixels. For the blue pixel, efficiency is 93.7% at the center wavelength of 479.5 nm; for the green pixel, efficiency is 95.9% at the center wavelength of 551 nm; for the red pixel, efficiency is 99.6% at the center wavelength of 607 nm. The measured FWHM or spectral width is ~ 12 nm. The pixels have the same grating thickness, homogeneous layer waveguide thickness, and fill factor, but three different grating periods, as shown in Figure 6-8 to reflect the three primary colors.

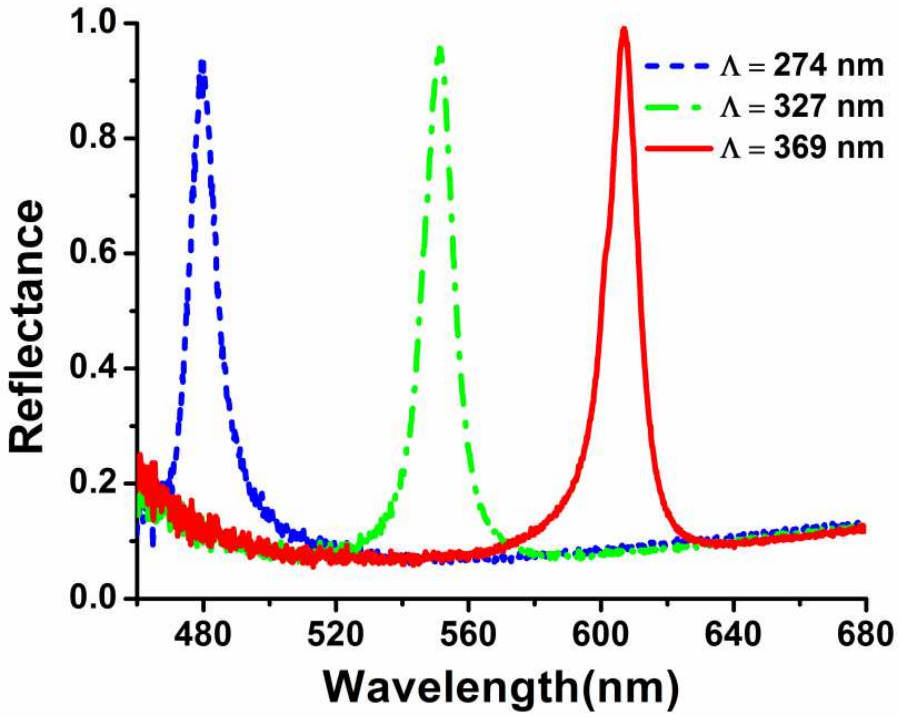

Figure 6-8 Spectral response of the tunable CFA. Blue filter: λ_c = 479.5 nm, R_0 = 93.7%; green filter: λ_c = 551 nm, R_0 = 95.9%; red filter: λ_c = 607 nm, R_0 = 99.6%. λ_c = center wavelength of a pixel, where the efficiency is maximum.

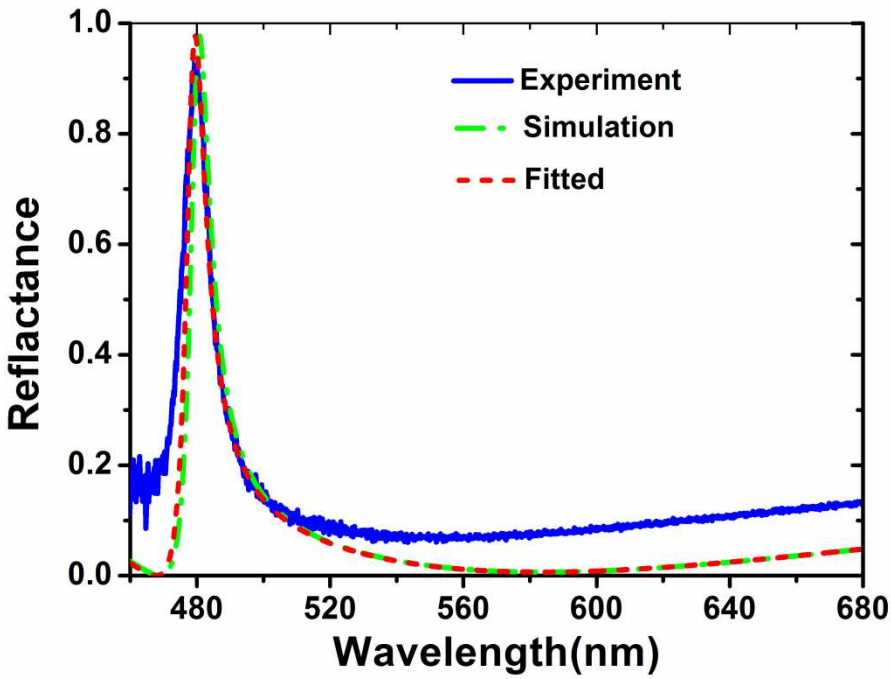

Figure 6-9 Experimental, simulated, and fitted results for the fabricated blue pixel. The fabricated device parameters are Λ = 274 nm, d_g = 58.5 nm, F = 0.46, and d_h = 106.5 nm; the fitting parameters are Λ = 273.15 nm, d_g = 58.5 nm, F = 0.46, and d_h = 106.5 nm.

Figure 6-9 compares the experimental, simulated, and fitted reflectance of the fabricated blue pixel. The simulated reflectance is calculated using the device parameters found by AFM and ellipsometry measurements. To fit the reflectance data, we slightly adjust the device parameters to take into account the measurement errors in AFM and ellipsometry so that the calculated and experimental curves match more closely. The fabricated device parameters are Λ = 273.15 nm, d_g = 58.5 nm, F = 0.46, and d_h = 106.5 nm and these same parameters are used for simulation; the parameters for fitted curve are Λ = 276 nm, d_g = 58.5 nm, F = 0.46, and d_h = 106.5 nm.

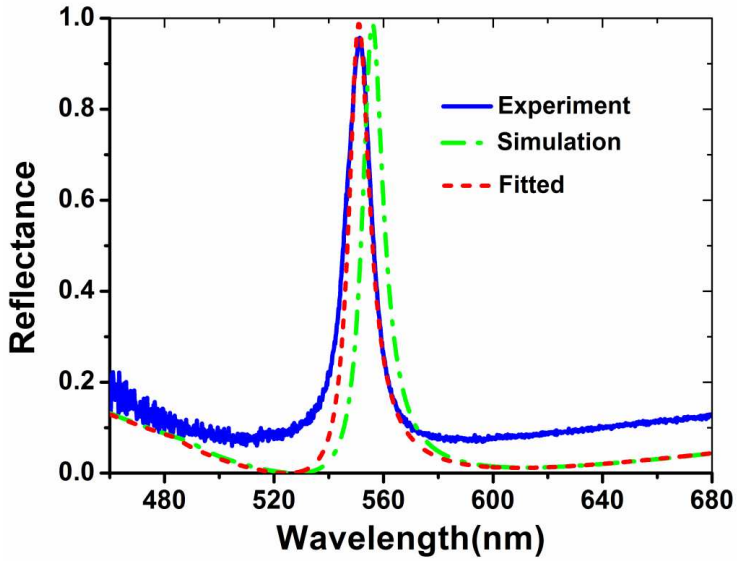

Figure 6-10 Experimental, simulated, and fitted results for the fabricated green pixel. The fabricated device parameters are Λ = 327 nm, d_g = 59.2 nm, F = 0.46, and d_h = 105.8 nm; the fitting parameters are Λ = 323.5 nm, d_g = 59.2 nm, F = 0.46, and d_h = 105.8 nm.

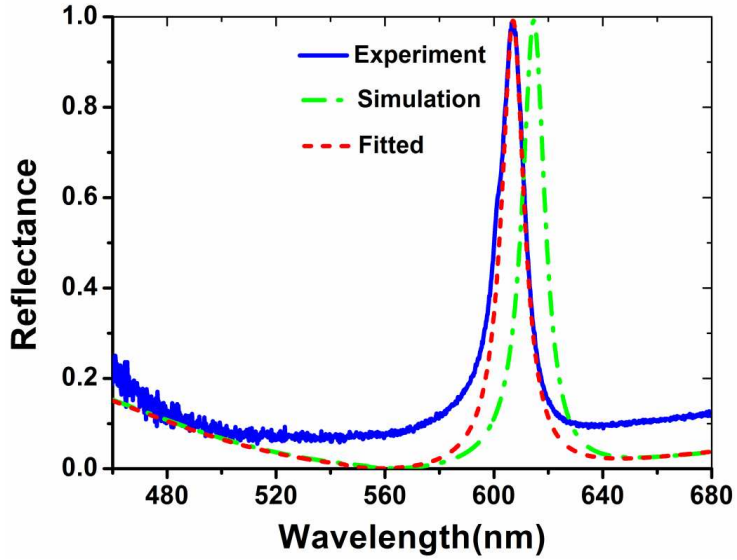

Figure 6-11 Experimental, simulated, and fitted results for the fabricated red pixel. The fabricated device parameters are Λ = 369 nm, d_g = 60.5 nm, F = 0.46, and d_h = 104.5 nm; the fitting parameters are Λ = 363.6 nm, d_g = 60.5 nm, F = 0.46, and d_h = 104.5 nm.

Figure 6-10 compares the experimental, simulated, and fitted reflectance of the fabricated green pixel. The fabricated device parameters are Λ = 327 nm, d_g = 59.2 nm, F = 0.46, and d_h = 105.8 nm and these same parameters are used for simulation; the parameters for fitted curve are Λ = 323.5 nm, d_g = 59.2 nm, F = 0.46, and d_h = 105.8 nm.

Figure 6-11 compares the experimental, simulated, and fitted reflectance of the fabricated red pixel. The fabricated device parameters are Λ = 369 nm, d_g = 60.5 nm, F = 0.46, and d_h = 104.5 nm and these same parameters are used for simulation; the parameters for fitted curve are Λ = 363.6 nm, d_g = 60.5 nm, F = 0.46, and d_h = 104.5 nm.

Table 6-1 summarizes the measured and fitted device parameters used in Figures 6-9 to 6-11. All the device parameters except the periods are kept same. Adjusting the device periods by a few nanometers provides the appropriate fitting of the experimental results, with the exception of the slight deviation in the sidebands.

Table 6-1: Experimental and fitted device parameters for color filter array

	Blue		Green		Red	
	Measured	Fitted	Measured	Fitted	Measured	Fitted
d_g (nm)	58.5	58.5	59.2	59.2	60.5	60.5
d_h (nm)	106.5	106.5	105.8	105.8	104.5	104.5
Λ (nm)	**274**	**273.15**	**327**	**323.5**	**369**	**363.6**
F	0.46	0.46	0.46	0.46	0.46	0.46
λ_c (nm)	479.5	479.5	551	551	607	607
R_0(%) at λ_c	93.7	98	95.9	99.1	99.6	99.7
	λ_c = center wavelength of a pixel, where the efficiency is maximum					

From the experimental reflectance values, standard RGB components (sRGB) values are calculated using Eqs. (6.1) − (6.4). The sRGB values are 90, 98, and 154 for the blue pixels; 92, 148, and 82 for the green pixels; and 162, 83, and 82 for the red

pixels. Figure 6-12 shows the perceived colors using the sRGB values of the pixels found from the experimentally observed reflectance values of the pixels.

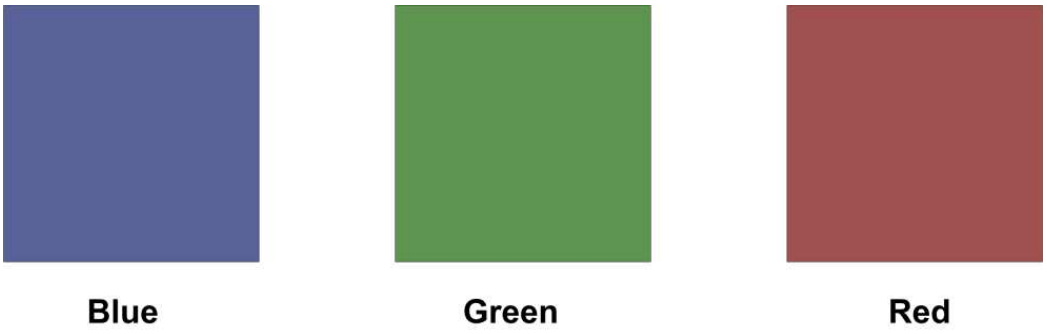

Figure 6-12 Perceived colors constructed from the experimentally observed reflectance values.

6.5 Conclusion

A highly efficient GMR-based reflective CFA is designed and fabricated using a subwavelength Si_3N_4 grating along with a homogeneous Si_3N_4 layer on a glass substrate. The array separates incident TE-polarized white light into its three primary colors: red, green, and blue. It exhibits high efficiency ~95% as well as high color purity due to the narrow bandwidth of ~12 nm. We find a good match between the experimental data and theoretical simulation results. The device has potential for applications in compact reflective LCD display and generally in projection display technology.

Chapter 7

Future Research Directions

This chapter briefly discusses some future research opportunities based on the work done in this thesis.

7.1 Fabrication of GMR LCD display

A GMR color filter array with high efficiency and narrow bandwidth is designed and fabricated in this study [48,49]. We can use this GMR color filters to fabricate a LCD display as shown in the following figure.

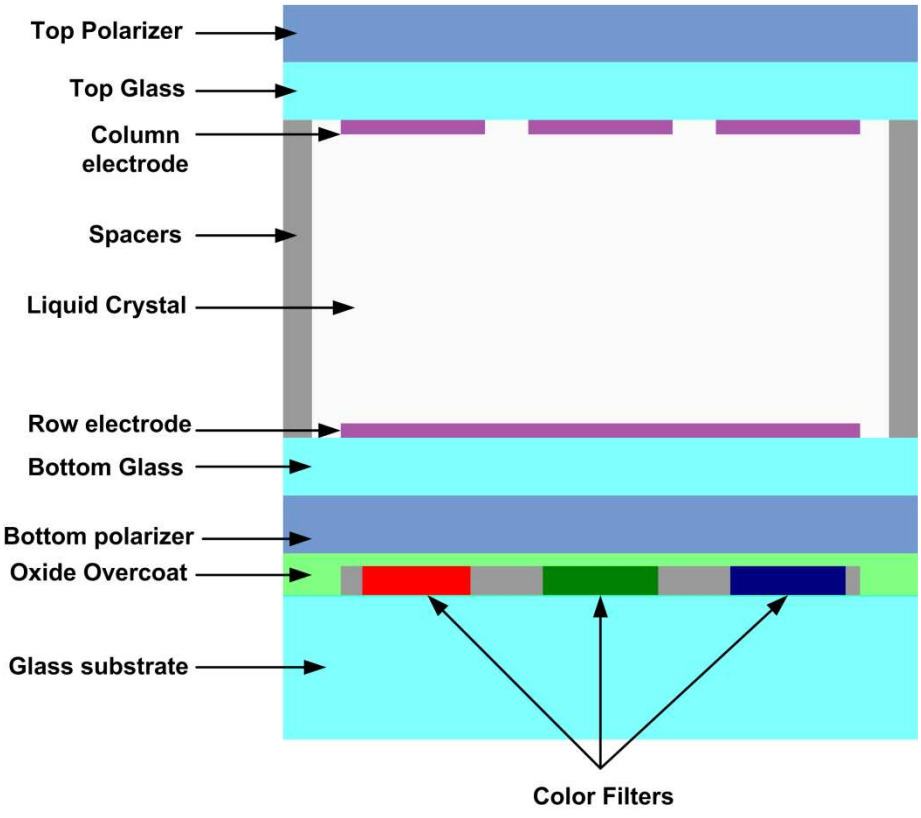

Figure 7-1 Proposed GMR LCD display.

Traditional reflective displays use transmissive color filters and a bottom mirror. As the GMR filters are reflective by nature, in our proposed display we eliminate the bottom mirror.

7.2 Design and Fabrication of Angle Independent GMR Color Filters

The GMR filters developed in this study are angle sensitive in nature. Though this angle dependency produces angle-tuned color filters, it limits the viewing angle and size of the display devices. By careful and appropriate design it is possible to achieve angle independent or angularly tolerant GMR color filters [32]. These angle independent color filters will facilitate the manufacturing of larger GMR display devices.

7.3 Design and Fabrication of Polarization Independent GMR Color Filters

The GMR color filters developed in this study are polarization dependent. This polarization dependency gives rise to a new type of tunable color filter as investigated in this study. But depending on the application requirement, we might need polarization independent operation of the filters. Some research has been carried out to realize polarization independent color filters [86]. By careful and appropriate design it is possible to have polarization independent operation of GMR color filters [32].

7.4 Fabrication of Ultra-Narrowband Thermo-Optic Tunable Filter

In Chapter 2, we demonstrated the design of an ultra-narrow band GMR filter working in the C communication band. The ideal realization of this device needs nearly lossless Si, very precise fabrication techniques, and very high resolution measurement setup. With those facilities available, the fabrication of this ultra narrow-band GMR filter is possible in the future.

Appendix A

List of Publications

Journals:

1. **M. Jalal Uddin** and Robert Magnusson, “Highly efficient color filter array using resonant Si_3N_4 gratings,” *Opt. Express*, vol. 21, no. 10, pp. 12495-12506, May 2013.
2. **M. Jalal Uddin** and Robert Magnusson, “Guided-mode resonant thermo-optic tunable filters,” *IEEE Phot. Technol. Lett.,* vol. 25, no. 15, pp. 1412-1416, Aug. 2013.
3. **M. Jalal Uddin** and Robert Magnusson, “Efficient Guided-Mode Resonant Tunable Color Filter”, *IEEE Photon. Technol. Lett.,* vol. 24, no. 17, pp. 1552-1554, Sep. 2012.
4. **M. Jalal Uddin,** and Robert Magnusson, “Design and Analysis of Narrow-Band Resonant Thermo-Optic Tunable Reflection Filters with Silicon Grating on Glass Substrate,” to be submitted to *Opt. Lett.* 2013.
5. **M. Jalal Uddin,** T Khaleque and Robert Magnusson, “Design and Fabrication of Polarization Controlled Tunable Resonant Color Filters,” to be submitted to *Opt. Express* 2013.
6. T. Khaleque, **M. Jalal Uddin** and Robert Magnusson, “Experimental Verification of Flat-Top Rayleigh Reflector,” to be submitted to *Opt. Lett.* 2013
7. T. Khaleque, **M. Jalal Uddin** and Robert Magnusson, “Design and Fabrication of Broadband Resonant Reflector for TE polarization” to be submitted to *Opt. Express*. 2013.

Conference Proceedings:

1. **M. Jalal Uddin** and R. Magnusson, “Polarization-Controlled Tunable Color Filters Fabricated in Silicon Nitride on Glass Substrates,” in the Proc. of *Frontiers in Optics,* pp. FTh2E.1, Orlando, Florida, USA, October 6-10, 2013.
2. **M. Jalal Uddin** and R. Magnusson, “Guided-Mode Resonant Color Filter Array for Reflective Displays,” in the Proc. of *IEEE Photonic Conference,* pp. MB3.4, Seattle, Washington, USA, September 8-12, 2013.
3. T. Khaleque, **M. Jalal Uddin** and R. Magnusson, “Optical filters enabled by the Rayleigh anomaly: Theory and experiment,” in the Proc. of *IEEE Photonic Conference,* pp. TuH3.3, Washington, USA, September 8-12, 2013.
4. **M. Jalal Uddin** and R. Magnusson, “Tunable Resonant Color Filters Fabricated in Silicon Nitride on Glass Substrates,” in the Proc. of *Frontiers in Optics,* pp. FTh1A.7, New York, USA, October 14-18, 2012.
5. **M. J. Uddin** and R. Magnusson, “Design and Fabrication of Thermo-Optic Tunable Guided-Mode Resonance Filters,” in the Proc. of *IPR,* Toronto, Canada, pp. IMB5, June 12-16, 2011.
6. **M. J. Uddin** and R. Magnusson, “Design and Fabrication of Shallow-Grating Guided-Mode Resonance Thermo-Optic Tunable Filters,” in the Proc. of *3rd IC4N*, Rhodes, Greece, pp. 139, June 26–29, 2011.
7. **M. J. Uddin** and R. Magnusson, “Thermally Tuned Resonant Optical Filters Fabricated in Amorphous Silicon,” in the Proc. of *OSA Frontiers in Optics*, San Jose, California, pp. FWU4, Oct. 16–20, 2011.

References

1. R. W. Wood, “On a remarkable case of uneven distribution of light in a diffraction grating spectrum,” Phil. Mag. **4**, 396-408 (1902).
2. R. W. Wood, “Diffraction gratings with controlled Groove form and abnormal distribution of light intensity,” Phil. Mag. **23**, 310-317 (1912).
3. R. W. Wood, “Anomalous diffraction gratings,” Phys. Rev. 48, 928-936 (1935).
4. Lord Rayleigh, “On the dynamic theory of gratings,” Proc. Roy. Soc. A **79**, 399-416 (1907).
5. U. Fano, “The theory of anomalous diffraction gratings and quasi-stationary waves on metallic surface (Sommerfeld's waves),” J. Opt. Soc. Am. **31**, 213-222(1941).
6. A. Hessel and A. A. Oliner, “A new theory of Wood's anomalies on optical gratings,” Appl. Opt. **4**, 1275-1299(1965).
7. R. H. Ritchie, E. T. Arakawa, J.J. Cowan, and R.N. Hamm, “Surface plasmon resonance effect in grating spectra,” Phys. Rev. Lett. **21**, 1530-1533 (1968).
8. H. Kogelnik, “Coupled wave theory for thick hologram gratings,” Bell Syst. Tech. **48**, 2909-2947 (1969).
9. T. Tamir, “Leaky waves in planar optical waveguide,” Nouv. Rev. Optique. **6**, 273-284 (1975).
10. S. T. Peng, T. Tamir, and H.L. Bertoni, “Theory of periodic dielectric waveguide,” IEEE Trans. Microwave Theory and Tech. MTT- **23**, 123-133 (1975).
11. R. Magnusson and T. K. Gaylord, “ Diffraction efficiencies of thin phase gratings with arbitrary grating shape,” J. Opt. Soc. Am. **68**, 806-809 (1978).
12. P. Vincent and M. Neviere, “Corrugated dielectric waveguides: A numerical study of the second-order stop bands,” Appl. Phys. **20**,345–351(1979).

13. M. G. Moharam and T. K. Gaylord, “Rigorous coupled-wave analysis of planar-grating diffraction,” J. Opt. Soc. Am. **71**, 811-818(1981).
14. T. K. Gaylord and M. G. Moharam, “Planar dielectric grating diffraction theories,” Appl. Phys. B **28**, 1-14(1982).
15. T. K. Gaylord and M. G. Moharam, “Analysis and application of optical diffraction by gratings,” Proc. of the IEEE **73**, 894-936(1985).
16. L. Mashev and E. Popov, “Zero order anomaly of dielectric coated gratings,” Opt. Comm. **55**, 377-380 (1985).
17. G. A. Golubenko, A. S. Svakhin, V. A. Sychugov, and A. V. Tishchenko, “Total reflection of light from a corrugated surface of a dielectric waveguide,” Sov. J. Quantum Electron.**15**, 886-887 (1985).
18. I. A. Avrutsky and V. A. Sychugov, “Reflection of a beam of finite size from a corrugated waveguide,” J. Mod. Opt. **36**, 1527-1539 (1989).
19. S.S. Wang, R. Magnusson, J. S. Bagby and M.G. Moharam, “Guided-mode resonances in planar dielectric-layer diffraction gratings,” J. Opt. Soc. Am. A **7**, 1470-1474 (1990).
20. R. Magnusson and S. S. Wang, “New Principle for optical filters,” Appl. Phys. Lett. **61**, 1275-1297 (1992).
21. S. S. Wang and R. Magnusson, “Theory and applications of guided-mode resonance filters,” Appl. Opt. **32**, 2606-2613(1993).
22. S. Tibuleac, and R. Magnusson, “Diffractive narrow-band transmission filters based on guided-mode resonance effect in thin-film multilayers,” IEEE Photon. Technol. Lett. **9**, 464-467(1997).
23. Z. S. Liu, S. Tibuleac, D. Shin, P. P. Young, and R. Magnusson, “High-efficiency guided-mode resonance filter,” Opt. Lett. **23**, 1556-1558 (1998).

24. S. Tibuleac, R. Magnusson, P. P. Young and T. R. Holzheimer, “Experimental verification of waveguide-mode resonant transmission filters,” IEEE Microwave and Guided Wave Lett. **9**, 19-21(1999).
25. R. Magnusson and S. S. Wang, “Transmission bandpass guided-mode resonance filters,” Appl. Opt. **34**, 8106-8109 (1995).
26. S. Tibuleac and R. Magnusson, “Reflection and Transmissin guided-mode resonance filters,” J. Opt. Soc. Am. A. **14**, 1617-1626 (1997).
27. D. Shin, S. Tibuleac, T. A. Maldonado, and R. Magnusson, “Thin-film optical filters with diffractive elements and waveguides,” Opt. Engg. **37**, 2634-2646 (1998).
28. S. Tibuleac and R. Magnusson, “Narrow-linewidth bandpass filters with diffractive thin-film layers,” Opt. Lett. **26**, 584-586 (2001).
29. S. S. Wang and R. Magnusson, “Design of waveguide-grating filters with symmetric line shapes and low side-bands,” Opt. Lett. **19**, 919-921 (1994).
30. S. S. Wang and R. Magnusson, “Multilayer waveguide-grating filters,” Appl. Opt. **34**, 2414-2420 (1995).
31. R. Magnusson, P. P. Young and D. Shin, “Vertical-cavity laser and laser array incorporating guided-mode resonance effects and methods for making the same,” US Patent No. 6154480 (2000).
32. D. Wawro, S. Tibuleac, R. Magnusson, and H. Liu, “Optical fiber endface biosensor based on resonances in dielectric waveguide gratings,” SPIE BIOS, 22-28(2000).
33. D. Rossenblatt, A. Sharon, and A. A. Friesem, “Resonant grating waveguide structure,” IEEE J. Quant. Electron. **33**, 2038-2058 (1997).
34. Y. ding and R. Magnusson, “Resonant leaky-mode spectral band engineering and device applications,” Opt. Express. **12**, 5661-5674 (2004).

35. K. J. Lee, R. LaComb, B. Britton, M. Shokooh-Saremi, H. Silva, E. Donkor, Y. Ding, and R. Magnusson, “Silicon-layer guided-mode resonance polarizer with 40-nm bandwidth,” IEEE Photon. Technol. Lett. **20**, 1857-1859 (2008).
36. K. J. Lee, J. Curzan, M. Shokooh-Saremi, and R. Magnusson, “Resonant wide-band polarizer with single silicon layer,” Appl. Phys. Lett. **98**, 211112(2011).
37. R. Magnusson and M. Shokooh-Saremi, “Physical basis for wideband resonant reflector,” Opt. Express. **16**, 3456-3462 (2008).
38. K. J. Lee and R. Magnusson, “Single-layer resonant high reflector in TE polarization: Theory and Experiment,” IEEE Photon. J. **3**, 123-129(2011).
39. R. Magnusson and Y. Ding, “MEMS tunable leaky mode filters,” IEEE Photon. Technol. Lett. **18**, 1479-1481(2006).
40. M. S. Amin, J. W. Yoon and R. Magnusson, “Optical transmission filters with co-existent guided-mode resonance and Rayleigh anomaly,” Appl. Phys. Lett. **103**, 131106(2013).
41. R. Magnusson, “Flat-top resonant reflectors with sharply delimited angular spectra: an application of the Rayleigh anomaly” Opt. Lett. **38**, 989-991(2013).
42. R. Magnusson, Y. Ding, K. J. Lee, D. Shin, P. S. Priambodo, P. P. Young, T. A. Maldonado, “Photonic devices enabled by waveguide-mode resonance effects in periodically modulated films,” Proc. of SPIE **5225**, 20-34(2003).
43. R. Magnusson and M. Shokooh-Saremi, “Widely tunable guided-mode resonance nanoelectromechanical RGB pixels,” Opt. Express. **15**, 10903-10910 (2007).
44. T. Khaleque, M. J. Uddin and R. Magnusson, “Optical filters enabled by the Rayleigh anomaly: Theory and experiment” Proc. of IEEE Photonic Conference, Seattle, USA, TuH3.3, 2013.

45. R. Magnusson, M. Shokooh-Saremi, K. J. Lee, J. Curzan, D. Wawro, S. Zimmerman, W. Wu, J. Yoon, H. G. Svavarsson, S. H. Song, “Leaky-mode resonance photonics: an applications platform,” Proc. SPIE **8102**, 810202-1– 810202-12 (2011).
46. R. Magnusson, “The complete biosensor,” J. Biosensors and Bioelectronics **4**, 1-2(2013).
47. T. Khaleque, H. G. Svavarsson, and R. Magnusson, “Fabrication of resonant pattern using thermal nano-imprint lithography for thin-film photovoltaic applications,” Opt. Express **21**, A631-A641(2013).
48. M. J. Uddin and R. Magnusson, “Efficient guided-mode resonant tunable color filters,” IEEE Photon. Technol. Lett. **24**, 1552-1554(2012).
49. M. J. Uddin and R. Magnusson, “Highly efficient color filter array using resonant Si3N4 gratings,” Opt. Express. **21**, 12495 -12506(2013).
50. M. J. Uddin and R. Magnusson, “Guided-mode resonant thermo-optic tunable filters, IEEE Photon. Technol. Lett. **25**, 1412-1415 (2013).
51. X. Fu, K. Yi, J. Shao, and Z. Fan, “Design of single-material guided-mode resonance filter,” Chinese Opt. Lett. **7**, 9-11(2009).
52. D. Sadot and E. Boimovich “Tunable optical filters for dense WDM networks,” IEEE Commun. Mag. **36**, 50-55(1998).
53. N. Gat, “Imaging spectroscopy using tunable filters: a review,” Proc. Of SPIE **4056**, 50-64(2004).
54. F. Grasdepot, H. Alause, W. Knap, J. P. Malzac, J. Suski, “Domestic gas sensor with micromachined optical tunable filters,” Sens. and Actuators B **36**, 377-380(1996).
55. T. E. Dimmick, G. Kakarantzas, T. A. Birks, A. Diez, and P. St. J. Russell, “Compact all-fiber acoustooptic tunable filters with small bandwidth-length product,” IEEE Photon. Technol. Lett. **12**, 1210-1213(2000).

56. R. Samarth, M. Li, and X. Lu, “An electro-optically tunable optical filter with an ultra-large wavelength tuning range,” Proc. Of SPIE **6368**, 1-7(2006).
57. J. Stone and L. W. Stulz, “Pigtailed high-finesse tunable fiber Fabry-Perot interferometers with large, medium and small free spectral range,” Electron. Lett. **23**, 781-783(1987).
58. A. Iocco, H. G. Limberger, R. P. Salathe, L. A. Everall, K. E. Chisholm, J. A. R. Williams, and I. Bennion, “Bragg grating fast tunable filter for wavelength division multiplexing,” J. Lightwave Technol. **17**,1217-1221(1999).
59. T. Amano, F. Koyama, T. Hino, M. Arai and A. Mastutani, “Design and fabrication of GaAs-GaAlAs micromachined tunable filter with thermal strain control,” J. Lightwave Technol. **21**, 596-601(2003).
60. B. Yu, G. Pickrell, and A. Wang, “Thermally tunable extrinsic Fabry–Perot filter,” IEEE Photon. Technol. Lett. **16**, 2296-2298(2004).
61. E. L. Wooten, R. L. Stone, E. W. Miles and E. M. Bradely, “Rapidly tunable narrowband wavelength filter using LiNbO3 unbalanced Mach-Zehnder interferometers,” J. Lightwave Technol. **14**, 2530-2536(1996).
62. D. Hohlfeld and H. Zappe, “An all-dielectric tunable optical filter based on the thermo-optic effect,” J. Opt. A: Pure Appl. Opt. **6**, 504-511(2004).
63. S. Yun and J. Lee, “A micromachined in-plane tunable optical filter using the thermo-optic effect of crystalline silicon,” J. Micromech. Microeng. **13**, 721-725(2003).
64. L. Domash, M. Wu, N. Nemchuk and E. Ma, “Tunable and switchable multiple-cavity thin film filters,” J. Lightwave Technol. **22**, 126-135 (2004).
65. M. Oh, H. Lee, M. Lee, J. Ahn, S. G. Han and H. Kim, “Tunable wavelength filters with Bragg gratings in polymer waveguides,” Appl. Phys. Lett. **73**, 2543-2545(1998).

66. M. S. Nawrocka, T. Liu, X. Wang and R. R. Panepucci, “Tunable silicon microring resonator with wide free spectral range,” Appl. Phys. Lett. **89**, 1-3(2006).
67. R. W. Sabnis, “Color filter technology for liquid crystal displays,” Displays **20**,119-129(1999).
68. K. Knop, “Diffraction grating for color filtering in the zero diffraction order,” Appl. Opt. **17**, 3598–3603(1978).
69. H. Dammann, “Color Separation gratings,” Appl. Opt. 17, 2273-2279(1978).
70. Y. Yoon, H. Lee, S. Lee, S. Kim, J. Park, and K. Lee, “Color filter incorporating a subwavelength patterned grating in ploy silicon,” Opt. Express **16**, 2374-2380(2008).
71. Y. Kanamori, M. Shimono, and K. Hane, “Fabrication of transmission color filter using subwavelength gratings on quartz substrate,” IEEE Photon. Technol. Lett.**18**, 2126-2128(2006).
72. H. Lee, Y. Yoon, S. Lee, S. Kim, and K. Lee, “Color filter based on a subwavelength patterned metal grating,” Opt. Express **15**,15457-15463(2007).
73. N. Nguyen-Huu, Y. Lo, and Y. Chen, “Color filters featuring high transmission efficiency and broad bandwidth based on resonant waveguide-metallic grating,” Opt. Commun. **284**, 2473-2479(2011).
74. A. F. Kaplan, T. Xu, and L. J. Guo, “High efficiency resonance-based spectrum filters with tunable transmission bandwidth fabricated using nanoimprint lithography,” Appl. Phys. Lett. **99**, 143111-143113(2011).
75. T. Xu, Y. Wu, X. Luo, and L. J. Guo, “Plasmonic nanoresonators for high resolution color filtering and spectral imaging,” Nat. Commun. **1**, ncomms1058(2010).
76. R. Magnusson and M. Shokooh-Saremi, “Widely tunable guided-mode resonance nanoelectromechanical RGB pixels,” Opt. Express **15**, 10903-10910(2007).

77. Q. Wang, D. Zhang, B. Xu, Y. Huang, C. Tao, C. Wang, B. Li, Z. Ni, and S. Zhuang, “Colored image produced with guide-mode resonance filter array,” Opt. Lett. **36**, 4698–4700(2011).

78. Y. Kanamori, H. Katsube, T. Furuta, S. Hasegawa, and K. Hane, “Design and fabrication of structural color filters with polymer-based guided-mode resonant gratings by nanoimprint lithography,” Jpn. J. Appl. Phys. **48**, 06FH04-1–06FH04-4, (2009).

79. D. M. Bloom, “The grating light valve: revolutionizing display technology,” Proc. SPIE, **3013**, 165-171(1997).

80. J. M. Younse, “Projection display systems based on the digital micromirror device (DMD),” Proc. SPIE, **2641**, 64−75 (1995).

81. M. W. Miles, “MEMS based interferometric modulator for display applications,” Proc. SPIE, **3876**, 20−28 (1999).

82. E. Cho, H. Kim, B. Cheong, P. Oleg, W. Xianyua, J. Sohn, D. Ma, H. Choi, N. park, and Y. Park, “Two dimensional photonic crystal color filter development,” Opt. Express **17**, 8621−8629 (2009).

83. T. Ellenbogen, K. Seo, and K. B. Crozier, “Chromatic plasmonic polarizers for active visible color filteging and polarimetry,” Nano Lett., **12,** 1026-1031 (2012).

84. B. Gralak, G. Tayeb and S. Enoch, “Morpho butterflies wings color modeled with lamellar grating theory,” Opt. Express **9**, 567−578 (2001).

85. C. J. Mogab, “The loading effect in plasma etching,” J. Electrochem. Soc., **24**, 1262-1268 (1977).

86. D. Inoue et al., “Polarization independent visible color filters comprising an aluminum film with surface-plasmon enhanced transmission through a subwavelength array of holes, ”, Appl. Phys. Lett. **98**, 093113(2011).

Biographical Information

Mohammad Jalal Uddin completed his B.Sc. and M.Sc. in electrical and electronic engineering from Bangladesh University of Engineering and Technology (BUET), Dhaka, Bangladesh in 2004 and 2008 respectively. After his graduation in 2004 he joined as a lecturer at electrical and electronic engineering department in Ahsanullah University of Science and Technology (AUST). In 2006, he joined as a lecturer in Bangladesh University of Engineering and Technology and in 2008 he was promoted as an assistant professor position. In 2009, he has started his PhD program at the department of electrical engineering in University of Texas at Arlington.

He has done several projects throughout his career. In his undergraduate study he built a personal computer based ECG machine. His M.Sc. research works include analysis of crosstalk in WDM optical fiber communication and dispersion and confinement loss analysis of photonic crystal fibers. In his PhD he has worked with the design and fabrication of guided-mode resonant tunable optical filters for WDM optical communication and display applications. During his internship in Texas Instruments in summer 2013 he worked with the modeling of optical components for silicon photonics applications.

His research interest include guided-mode resonance devices and their applications, silicon photonics, photonic crystals, photonic crystal fiber, photonic crystal laser, opto-electronic devices, nano-photonics, non-linear optics, optical fiber communications; RF and Microwave photonics.

His future plan is to continue doing research based on the background he obtained from UT Arlington through his PhD. His short term goal is to find a research position in a reputed industry or academic institution. His long term goal is to find a tenure-track faculty position in a reputed university in the world.